2017

Theoretical Study of Negative Molecular Ions Relevant to the Interstellar and Laboratory Plasma

Marjan Khamesian
University of Central Florida

THEORETICAL STUDY OF NEGATIVE MOLECULAR IONS RELEVANT TO THE INTERSTELLAR AND LABORATORY PLASMA

by

MARJAN KHAMESIAN
M.S. University of Mazandaran, 2010

A dissertation submitted in partial fulfilment of the requirements
for the degree of Doctor of Philosophy
in the Department of Physics
in the College of Sciences
at the University of Central Florida
Orlando, Florida

Spring Term
2017

Major Professor: Viatcheslav Kokoouline

ABSTRACT

Recently, several negative molecular ions, C_nN^- ($n = 1, 3, 5$) and C_nH^- ($n = 4, 6, 8$), were observed in the interstellar medium (ISM). It was suggested that the anions are formed in the ISM by the process of radiative electron attachment (REA). A simple statistical model was developed in 1980's to estimate rate coefficients of the REA reactions. Some of the rate coefficients obtained in the model are consistent with the observations, the others are not. More importantly, some of the approximations employed in the model are not physically justified.

The aim of this thesis is a development of a quantum-mechanical approach to study the process of radiative electron attachment to linear molecules of astrophysical interest. The approach is based on accurate *ab initio* calculations of electronic bound and continuum states of the negative ion. Cross sections and rate coefficients for formation of the following molecular negative ions by REA were determined: CN^-, C_2H^-, C_3N^-, C_4H^-, C_5N^-, C_6H^-, and C_8H^-. All the calculations presented in the thesis were carried out using the MOLPRO and UK R-matrix (Quantemol) suites of programs. Uncertainty quantification of the results, obtained for each studied system, was performed. The uncertainty of the final cross sections and rate coefficients were obtained by varying parameters of the computational model such as a chosen Gaussian basis set, the size of the R-matrix box, and other parameters of the model.

A second process, closely related to the radiative electron attachment, photodetachment (PD), was also studied in the thesis. Photodetachment cross sections for the C_nN^- ($n = 1, 3, 5$), C_nH^- ($n = 4, 6, 8$) and C_2^- molecules were determined using an approach similar to the one employed for REA from the same transition dipole moment matrix elements. The obtained REA cross sections and rate coefficients were validated by comparing the present theoretical results with the experimental data from recent photodetachment experiments.

Overall, given that the agreement between theoretical and experimental PD cross sections is good, the obtained REA cross sections are also accurate. Therefore, the present results suggest that the observed abundance of these ions in the ISM can hardly be explained by the REA process. In other words, these anions are formed in the interstellar medium by a process different than radiative electron attachment.

Dissociative electron attachment (DEA) is another process of anion formation, which could possibly explain formation of certain molecular anions in the ISM. The ClF attachment was studied using a first principle approach: *ab initio* calculation of the ClF and ClF^- potential energy curves and R-matrix calculations were performed to determine the DEA cross section and rate coefficient. A good agreement with experimental data was demonstrated.

A theoretical approach to evaluate cross sections for rotational excitation of linear neutral molecules by an electron impact was developed and applied to acetylene, HCCH. The differential cross sections for e-HCCH scattering were calculated between energies 0.1 eV and 10 eV. The momentum transfer cross section and eigenphases for e-HCCH scattering were also calculated.

To my parents, with love.

ACKNOWLEDGMENTS

I would like to express the deepest appreciation to my advisor Prof. Viatcheslav Kokoouline, who has the attitude and the substance of a genius. Without his encouragement, advice and persistent helps, this dissertation would not have been possible. I appreciate all his contributions of time, patience and ideas to make my Ph.D. experience productive. I have been amazingly fortunate for having the opportunity to join his group and I deeply appreciate his kindness and belief in me.

For this dissertation, I would like to thank my committee members: Prof. Hari Saha and Prof. Luca Argenti for their time, interest, and helpful comments. I would also like to thank Prof. Patrick Schelling for taking time to discuss my proposal. I gratefully acknowledge the funding sources that made my Ph.D. work possible. This work was supported by the National Science Foundation, Grant No PHY-15-06391.

Special thanks should also be given to my parents for all their endless love, encouragement, and believing in me through all of these years and my life in general. I cannot thank them enough for what they have done for me. I honestly believe that I have the best parents in the world and I will be grateful forever. I am a lucky daughter because you have always been there for me and I am sorry for being miles away from you!

My heartfelt thanks to my sister Maryam, who I have not seen her since I came to US, for being patient with me in my long absence and offering words of encouragements. Maryam, no matter where you are around the world, you are always with me! To my twin sister Mahvand, for her invaluable support and affection. I wish we could have spent our Ph.D. life together like we have been during Bachelor and Master. Do not forget that I could always tell you 'when I was your age' and proceed to tell what I did five minutes ago!

To all my true friends, thank you for your understanding and encouragement in many moments. You are always on my mind. And most of all to my loving, supportive, encouraging, and patient husband Amin whose faithful support during these years of this Ph.D. is so appreciated. Words cannot describe how lucky I am to have him in my life. I love you, and look forward to our lifelong journey!

TABLE OF CONTENTS

LIST OF FIGURES

LIST OF TABLES

CHAPTER 1: INTRODUCTION

Electron-Molecule Collision and its Applications

In recent years, experimental [1, 2, 3, 4] and theoretical research [5, 6] on formation and manipulation with negative molecular ions has attracted considerable attention because of the important role the ions play in many technological applications. In a laboratory environment, different types of molecular anions are often formed by dissociative electron attachment or by charge transfer in a low-energy collision with a highly-excited Rydberg atom, such as Rb or Cs [7].

Collisions of low-energy electrons with molecules are of fundamental interest in the interstellar medium (ISM) [8] in many applications in modern technologies, such as, in lasers and in the ignition of internal combustion engines. They are also considered as the main process in cool plasmas and discharges. They appear in the upper atmosphere of the Earth and other planets, such as auroras [9] and lightning [10]. Determining the energy balance and transport properties of electrons in low-temperature gases and plasmas under a wide variety of conditions is another important role of these collisions processes. Other applications include magnetohydrodynamic power generation [11], electron lasers, such as the CO_2 laser [12], the interstellar medium of outer space [13], and other example of nonequilibrium plasmas [14]. In the case of magnetohydrodynamic power generation, a process similar to the mechanism that occurs in the magnetosphere of earth's atmosphere, in which plasma is the working fluid [15], the electrical conductivity of the coal-fired plasma is restricted by electron-molecule scattering [14]. The CO_2 electron laser includes electron-impact excitation of vibrational and rotational states of the CO_2 molecule. Knowledge of the relevant electron collision cross sections is essential to the computer modeling and optimization of this laser system. Obtaining such data by experiment is extremely difficult, and because of that, theory plays an important role here. In the ISM, rotational excitation of molecules in elec-

tron collisions is considered as an important mechanism for cooling the electrons and establishing rotational temperature of the gas. In addition, in the upper atmospheres of the Earth and other planets, inelastic electron-molecule collision processes cause the decrease of photo-electrons and other electrons produced by cosmic rays and photoionisation of atmospheric components. Vibrational and rotational excitation of molecules are specifically important at electron energies below electronic-excitation thresholds [14].

Another motivation for experimental and theoretical studies of electron-molecule scattering processes comes from modeling of discharge environments, such as planetary atmospheres bombarded by photons and charged particles [16, 17], understanding of atmospheric reentry physics in space programs [18], and modeling of chemical plasmas for surface treatments [19, 20, 21, 22]. In a recent study by L. Sanche [23], the damage to DNA caused by the impact of low energy electrons was discussed. Other applications include anomaterials fabrication using focused electron-beam-induced processing [24, 25] and more recently pretreatment of biomass to obtain biofuels [26, 27, 28].

There were several attempts to utilize negative ion beams for materials science. One of such attemps is negative ion beam technology [29], which is attracting a lot of attention [30]. In fact, for negative ion production, heavy negative ions could be produced in high yields through secondary-ion production method by sputtering [31]. For a development of a negative ion implanter of a high current negative ion source [30], negative ions are believed to be a good solution [30].

The possibility for atomic anions to be formed in the ISM by radiative electron attachment (REA) in electron-atom collisions, namely, the formation of H^-, was first suggested by McDowell [32] in 1961. Later, Dalgarno and McCray [13] discussed the role of negative atomic ions in the formation of neutral molecules in the ISM.

Compared to neutral molecules or positive ions, some key properties of negative ions, such as electron affinities, are very difficult to obtain accurately. The electron affinity is the difference between binding energy in atom and in the corresponding negative ion. In fact, electron correlation influences significantly the properties of a negative ion [33].

The discovery of several molecular anions, C_nN^- ($n = 1, 3, 5$) [34, 35, 36, 37] and C_nH^- ($n = 4, 6, 8$) [38, 39, 36, 40, 41, 37, 42] in the ISM has prompted a discussion about the mechanism of their formation. In fact, before the discovery, the formation of molecular anions in the ISM was theorized by Herbst [43], who suggested that the anions could be formed in the ISM by radiative electronic attachment.

Models show that the negative ions should also be present in the planetary atmospheres and may play a significant role in upper atmospheres of Titan [44, 45, 46, 47] and similar planets (moons) having a high concentration of nitrogen and carbon (see, for instance, Ref. [48]). However, the mechanism of their formation in the ISM has not yet been well established. They are produced under various physical conditions, and several different mechanisms may contribute to their formation. Among several proposals on the formation mechanism of the anions in the ISM, are dissociative or radiative electron attachment. To validate any of the proposed mechanisms of anion formation, one has to know the rate constants (cross sections) for corresponding processes. Following the initial idea of the formation mechanism suggested by Herbst [43, 49, 50], it is now generally accepted by the astronomy community that negative molecular ions are likely formed by the process of radiative attachment of an electron to a neutral molecule.

Measurements of cross sections for electron-molecule collisions are both expensive and difficult to perform. The theoretical calculation of cross sections requires the use of sophisticated procedures based on the application of quantum mechanics. Knowledge of cross sections and branching ratios for such electron-molecule collisional processes involving small polyatomic negative ions is crucial

also in plasma modeling (in laboratory, in the ISM, or in technological applications). In addition, studies of negative ions should be of interest in problems related to the spectra of high temperature plasmas and stellar atmospheres [51]. One of the dominant sources of spectral opacity is the photodetachment of negative ions [52], since the binding energies of the negative ions correspond in general to radiation in the visible and infrared regions.

Theoretical Methods

Some of the needed cross sections (rate coefficients) could be obtained via experiment. However, for many reactions involving formation and reactivity of negative molecular ions, an experimental approach is not possible due to the instability of anions. At present, with the current available *ab initio* quantum-chemistry packages and the abundant computational resources, it appears that theoretical approaches based on first principles only, can be successfully applied to study different mechanisms for the formation of negative molecular ions and their reactivity.

Theoretical description of electron-molecule collisions involving excited or continuum electronic states of anions is difficult. Despite significant progress made in quantum-chemistry first-principle methods, which can describe very accurately the ground electronic state, an accurate description of highly excited bound states remains a difficult problem. In addition, accurate determination of the electron-molecule scattering states at energies between 10 meV and 10 eV is even more complicated.

In order to study REA theoretically, one should be able to obtain electronic wave functions for electron-molecule scattering. Although theoretical treatments of collisions of electrons with diatomic or linear triatomic molecules have reached significant level of sophistication and reliability, theoretical calculations on electronic collisions with nonlinear polyatomic molecules are still at a

relatively primitive stage [53]. The development of efficient theoretical methods for the *ab initio* calculation of low-energy electron-molecule scattering cross sections has confirmed to be difficult. There are three main methods, which are able to provide cross sections for processes involving collision between electrons and simple diatomic molecules with atoms from the first two periods of the periodic table. These methods are the complex Kohn variational method [54], Schwinger variational method [55], and the R-matrix method [56, 54]. In this section, I describe the UK R-matrix method employed in this thesis. The two other *ab initio* variational methods, the complex Kohn and the Schwinger method, are also briefly discussed below.

R-Matrix Approach

Over the past years there was a considerable progress in development more effective techniques for calculating cross sections for electron-atom/molecule collisions. One of them is the R-matrix approach. The R-matrix approach was first introduced by Wigner and Eisenbud [57], and in the early 1970s [58], the R-matrix theory was established as a standard *ab initio* procedure for calculating electron-atom and electron-molecule collision cross sections.

In addition, the approach was applied for scattering of light and heavy particles: nucleons, nuclei, electrons, atoms, and molecules [60]. In recent years, the R-matrix theory was developed to such a level that it can provide a complete theoretical framework for the treatment of different processes involving electron-molecule collisions. At low-energy collisions, when electron-impact ionization is energetically forbidden the following reactions can happen: elastic scattering ($\mathrm{AB} + e^- \rightarrow \mathrm{AB} + e^-$), electronic excitation ($\mathrm{AB} + e^- \rightarrow \mathrm{AB}^* + e^-$), vibrational excitation ($\mathrm{AB}\ (v'' = 0) + e^- \rightarrow \mathrm{AB}\ (v') + e^-$), rotational excitation ($\mathrm{AB}\ (N'') + e^- \rightarrow \mathrm{AB}\ (N') + e^-$), dissociative attachment/recombination ($\mathrm{AB} + e^- \rightarrow \mathrm{A}^- + \mathrm{B}$, $\mathrm{AB}^+ + e^- \rightarrow \mathrm{A} + \mathrm{B}$), impact dissociation ($\mathrm{AB} + e^- \rightarrow \mathrm{A} + \mathrm{B} + e^-$). All of these processes can have AB^- as a common intermediary.

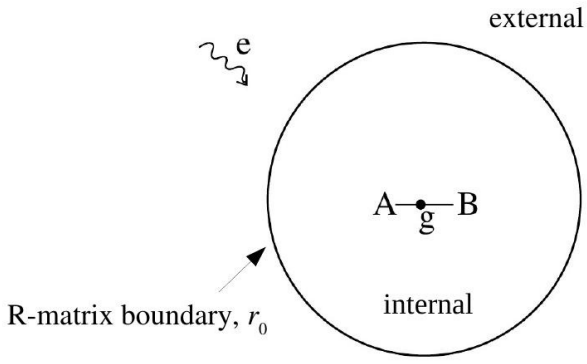

Figure 1.1: Partitioning of configuration space into an internal and an external region by a boundary surface of radius r_0 in the R-matrix theory of electron-molecule collisions [59].

The R-matrix method for treating electron-molecule collisions, used in this thesis, is designed to obtain accurate wave functions for this intermediary and therefore gives an effective theoretical framework of modeling all the processes described above [61].

The R-matrix method is based on a division of the configuration space into two regions (Fig. 1.1): an internal region, which contains the wave function of the target molecule and an external region for which simplified equations can be solved [59]. The two regions are separated by a spherical boundary of radius r_0, known as the channel radius, which is centered on the target center of mass, g in the figure. This radius is chosen large enough so that, in the external region, the different parts of the studied system interact only through long-range forces and antisymmetrization effects can be neglected. Because distances in the internal region are restricted, eigenstates of the system form a discrete basis there. In this region, a scattering wave function can be expanded at an arbitrary energy over these eigenstates. Therefore, the R-matrix can be calculated by inversing the logarithmic derivative of the wave function at the boundary [60].

The R-matrix method has many advantages, such as the inner region problem needs to be solved only once and also the energy dependence is obtained completely from the solution in the outer region, which is a much simpler problem. Another important advantage of the R-matrix method, is the ability to produce solutions at a large number of energies at little extra computational cost [59].

Before discussing the results obtained by this method, the basic principles of R-matrix are briefly discussed below. A radial scattering wave function for channel i, at R-matrix boundary, $r = a$, can be written as [59]

$$F_i(a) = \sum_j R_{ij}(a, E) a \frac{dF_j}{dr}|_{r=a} \,, \tag{1.1}$$

where a is the radius of the R-matrix sphere. $F_i(r)$ represents the outer region radial wave function for channel i, describing the motion of the scattered electron and $R_{ij}(r, E)$ is the R-matrix linking channels i and j with scattering energy E and radius for R-matrix propagation, r. The subscript i numerates the channel or the different asymptotic quantum states of the colliding particles before and/or after the collision. The R-matrix, $R_{ij}(a, E)$, connects the radial wave function to its derivative. It can be seen from the formula that the R-matrix depends on distance and energy. In matrix notation Eq. (1.1) is written as

$$\mathbf{F}(a) = \mathbf{R}(a, E) a \frac{d\mathbf{F}}{dr}|_{r=a} \,. \tag{1.2}$$

In the other words, for any radial distance, the R-matrix is defined by

$$\mathbf{R}(r, E) = \frac{\mathbf{F}(r)}{r\mathbf{F}'(r)} \,, \tag{1.3}$$

where a prime is used to denote the derivative.

To derive an expression for the R-matrix, connecting solutions of the Schrödinger equation in the inner region and the outer region, first consider the general Schrödinger equation given by an $N+1$ electron Hamiltonian, $\mathcal{H}$, and its wave function $\mathbf{w}$, within the frozen nuclei approximation:

$$(\mathcal{H} - \mathbf{E})\mathbf{w}(E) = 0\,, \tag{1.4}$$

By considering this equation over a finite spherical volume, which has a surface at $r = a$, an extra term needs to be added, which is derived by Bloch [62], such that the operator remains Hermitian. The Bloch term (Eq. (5) at Ref. [59]) in the Schrödinger Eq. (1.4) gives

$$(\mathcal{H} + \mathbf{L} - \mathbf{E})\mathbf{w} = \mathbf{L}\mathbf{w}\,, \tag{1.5}$$

which is the Schrödinger equation for the space surrounded by the sphere given by $r \leq a$. The operator $\mathcal{H} + \mathbf{L}$ is considered as the inner region Hamiltonian. The Eq. (1.5) has the following solution

$$\mathbf{w} = (\mathcal{H} + \mathbf{L} - \mathbf{E})^{-1}\mathbf{L}\mathbf{w}\,. \tag{1.6}$$

The above equation is derived for the region of $r \leq a$, which results in discrete values of the energy, E_k and solutions $\mathbf{w_k}$. The corresponding wave functions satisfies the following equation

$$\langle \mathbf{w_k} | \mathcal{H} + \mathbf{L} | \mathbf{w_k}' \rangle = \delta_{kk'} E_k\,, \tag{1.7}$$

where the Dirac brackets mean an integration over the finite volume defined by $r \leq a$. $\mathbf{w_k}$ are the eigenfunctions of the inner region Hamiltonian and represent a complete basis set inside the

R-matrix sphere. The solution of Eq. (1.4) expanded in this basis set is given by

$$\mathbf{w}(E) = \sum_k A_k(E)\mathbf{w_k}\,. \tag{1.8}$$

Inserting Eq. (1.6) into Eq. (1.7) gives

$$\mathbf{w}(E) = \sum_k \frac{|\mathbf{w_k}\rangle\langle\mathbf{w_k}|\mathbf{L}|\mathbf{w}\rangle}{(E_k - E)}\,, \tag{1.9}$$

which can be rewritten as

$$F_i(a) = \frac{1}{2}\sum_k \frac{w_{ik}(a)}{E_k - E}\sum_j w_{jk}(a)[r\frac{dF_j}{dr} - bF_j]|_{r=a}\,, \tag{1.10}$$

where $w_{ik}(a)$ are the amplitudes of the inner region functions at $r = a$. Thus, Eq. (1.10) can be rewritten as

$$F_i(a) = \sum_j R_{ij}(a,E)[r\frac{dF_j}{dr} - bF_j]|_{r=a}\,, \tag{1.11}$$

where $R_{ij}(a,E)$ is the standard form of the R-matrix on the boundary [59], which is given by

$$R_{ij}(a,E) = \frac{1}{2}\sum_k \frac{w_{ik}(a)w_{jk}(a)}{E_k - E}\,. \tag{1.12}$$

The main goal of the inner calculation is to provide the necessary numerical values to construct the R-matrix of Eq. (1.12) on the boundary.

The Inner Region

The inner region wave function is obtained using the close-coupling approach [63], which is widely used in other *ab initio*, low-energy electron-molecule collisions methods [64]. Thus the inner region wave function is written as [59]

$$\Psi_k{}^{N+1} = A \sum_{ij} a_{ijk} \Phi_i^N(\mathbf{x}_1 ... \mathbf{x}_N) u_{ij}(\mathbf{x}_{N+1}) + \sum_i b_{ik} \chi_i^{N+1}(\mathbf{x}_1 ... \mathbf{x}_{N+1}) \,, \tag{1.13}$$

where the target includes N electrons and functions which labeled as N or $N+1$ referred to the target or the compound scattering system respectively. Φ_i^N is the wave function of i^{th} target state and u_{ij} denotes the extra orbitals, which represents the scattering electron. It should also be noted that, the electrons with represented space-spin coordinates, $\mathbf{x}_i$, must obey the Pauli principle and are therefore anti-symmetrized by operator A. The second summation in Eq. (1.13) includes configurations with no amplitude on the R-matrix boundary, where all electrons are placed in orbitals associated with the target.

The continuum basis functions as a partial wave expansion using polar coordinates (r, θ, ϕ) is given by

$$v_{ij}(r, \theta, \phi) = f_{ij}(r) Y_{l_i, m_i}(\theta, \phi) E_{\frac{1}{2}} \,, \tag{1.14}$$

where Y_{l_i, m_i} is the normalized spherical harmonic and the (l_i, m_i) are related to the asymptotic channel associated with the i^{th} target state and these angular momentum quantum numbers. $f_{ij}(r)$ is the radial part of continuum basis function, v_{ij} . The function $E_{\frac{1}{2}}$ is a one half electron spin function [59].

The Outer Region

In the outer region the wave function is given by [59]:

$$\Psi^{N+1}(E) = \sum_{i=1}^{n} \Phi_i^N(\mathbf{x}_1 ... \mathbf{x}_N) F_i(r_{N+1}) Y_{l_i,m_i}(\theta,\phi) E_{\frac{1}{2}} \,, \tag{1.15}$$

where the sum runs over the n channels of the problem. For molecular problems, there are several channels related to each target state, therefore for solving a one-state problem a multichannel outer region problem needs to be solved.

For solving the outer region problem, information about asymptotic channels of the problem and outer region potentials is needed. Asymptotic channel i describes a state of the target molecule and a partial wave of the scattering electron, (l_i, m_i). If the target state related to channel i has energy E_i^N, the related wavenumber of the scattering electron is given by

$$k_i^2 = \frac{2m_e(E - E_i^N)}{\hbar^2} \,, \tag{1.16}$$

where m_e is the electronic mass, and E is the energy of the scattered electron. An open channel is defined when $k_i^2 \geq 0$ and closed when $k_i^2 \leq 0$. For a general scattering problem the outer region solutions asymptotically, at large r for open channel can be written as

$$F_{ij} \sim \frac{1}{\sqrt{k_i}} (\sin\theta_i \delta_{ij} + \cos\theta_i K_{ij}) \,. \tag{1.17}$$

For neutral targets the channel phase θ_i is

$$\theta_i = k_i r - \frac{1}{2} l_i \pi \,. \tag{1.18}$$

The $\mathbf{K}$-matrix in Eq. (1.17) is a symmetric matrix with the dimension equal to the number of

open channels. Many scattering observables can be obtained from the $\mathbf{K}$-matrix. For example, the scattering matrix $\mathbf{S}$ is expressed as [59]

$$\mathbf{S} = \frac{(\mathbf{1} + i\mathbf{K})}{(\mathbf{1} - i\mathbf{K})} \,. \tag{1.19}$$

$\mathbf{T}$-matrix can also be directly derived from $\mathbf{S}$-matrix from the equation $\mathbf{T} = \mathbf{S} - \mathbf{1}$.

In calculations presented in the thesis, the R-matrix approach is employed to model collisions of electrons with the molecules of astrophysical interest mentioned above. Besides the R-matrix method, there are two other *ab initio* variational methods for electron-molecule scattering used in the community: the complex Kohn variational and Schwinger variational methods.

Complex Kohn Method

The complex Kohn method is an algebraic variational method for studying collisions of electrons with polyatomic molecules [65]. In the complex Kohn method, to describe the scattering of an electron incident in a channel Γ of the target molecule, the first step is to choose the trial scattering wave function, which is to be used in the variational principle [53]. The trial wave function is defined by [54]

$$\Psi_{\Gamma'}(r_1, ..., r_{N+1}) = \sum_{\Gamma} A(\chi_{\Gamma}(r_1, ..., r_N) F_{\Gamma\Gamma'}(r_{N+1})) + \sum_{\mu} d_{\mu}^{\Gamma'} \Theta_{\mu}(r_1, ..., r_{N+1}) \,, \tag{1.20}$$

where the first summation runs over open channels, denoted by χ_{Γ}, which are the target functions. The functions Θ_{μ} are an orthonormal set of antisymmetric, square-integrable $(N + 1)$ electron functions used to represent polarization and correlation effects, which are not included in the first summation [54]. The target functions χ_{Γ} is single or multiconfiguration descriptions of the bound

states of the target molecule and the second summation includes closed channel functions, which also contain $(N+1)$ electron configurations [53]. The symbol Γ refers to all the quantum numbers needed to represent a physical state of the system, i.e., the internal state of the target molecule, as well as the energy and orbital angular momentum of the scattered electron [54].

The channel continuum functions $F_{\Gamma\Gamma'}$ can be expanded as [54]

$$rF_{\Gamma\Gamma'}(r) = \sum_{l,m}[f_l^{\Gamma}(r)\delta_{ll'}\delta_{mm'}\delta_{\Gamma\Gamma'} + T^{\Gamma\Gamma'}_{lml'm'}g_l^{\Gamma}(r)]Y_{lm}(\hat{r}) + \sum_k c_k^{\Gamma\Gamma'}\phi_k^{\Gamma}(r)\,, \tag{1.21}$$

where Y_{lm} is a normalized spherical harmonic, the ϕ_k^{Γ} are a set of square-integrable functions, and the functions, f_l^{Γ} and g_l^{Γ}, are linearly independent continuum orbitals. The coefficients $T^{\Gamma\Gamma'}_{lml'm'}$, $c_k^{\Gamma\Gamma'}$, and $d_{\mu}^{\Gamma}{}'$ are to be determined from a stationary principle [54].

This method was successfully applied to calculate the radiative electron attachment (REA) and photodetachment (PD) cross sections of some of the anions listed above in the previous works [5, 66]. In the next chapter, I will compare our results with those obtained applying this method.

Schwinger Method

The Schwinger variational (SV) method was introduced by Schwinger [67] in 1947. The method uses the Lippmann-Schwinger integral equation [68], equivalent to the Schrödinger equation, to compute scattering amplitude and scattering matrices.

The first application of the SV method was published by Blatt et al. [69] in 1949 in a study of neutron-proton scattering below 10 MeV. They applied the SV principle to obtain an estimate for the bound state energy of the deuteron. Later, Kato demonstrated that the SV method gives an upper/lower bound for the phase shift when the potential is purely positive/negative. He also

established the upper and lower bounds for elastic electron-hydrogen scattering [70].

In the SV method, a Green's function is introduced for the asymptotic electron continuum part of the total wave function [71]. In Ref. [72], electron-molecule collisions were studied using Schwinger variational principle with plane waves as a trial basis set. According to the study, for electron-molecule elastic scattering, the bilinear variational construction of the scattering is

$$f(\vec{k_f},\vec{k_i}) = -\frac{1}{2\pi}\{\langle S_{\vec{k}_f}|V|\Psi^{(+)}_{\vec{k}_i}\rangle + \langle\Psi^{(-)}_{\vec{k}_f}|V|S_{\vec{k}_i}\rangle - \langle\Psi^{(-)}_{\vec{k}_f}|V - VG_0^{(+)}V|\Psi^{(+)}_{\vec{k}_i}\rangle\}\,, \tag{1.22}$$

where $|S_{\vec{k}_i}\rangle$ is the input channel state, which is represented by the product of a plane wave $\vec{k}_i$ times $|\Phi_0\rangle$, the initial (ground) target state. $|S_{\vec{k}_f}\rangle$ is a plane wave with wave vector $\vec{k}_f$. V is the interaction between the incident electron and the target, and $G_0^{(+)}$ is the projected Green's function [73, 74]:

$$G_0^{(+)} = \int d^3k \frac{|\Phi_0\vec{k}\rangle\langle\Phi_0\vec{k}|}{(E - \mathcal{H}_0 + i\epsilon)}\,, \tag{1.23}$$

where $\mathcal{H}_0$ is the Hamiltonian for the N electrons of the target, plus the kinetic energy of the incident electron, and E is total energy of the system (target + electron). The scattering states, $\Psi^{(+)}_{\vec{k}_i}$ and $\Psi^{(-)}_{\vec{k}_f}$, are products of the target wave function $|\Phi_0>$ and one-particle scattering wave function. More details of this method and its applications can be found in the literature, for example in Refs. [75] and [76].

Thesis Layout

The rest of the thesis is organized in the following way, chapter 2 discusses different mechanisms for the formation of the anions discovered in the ISM. Cross sections and rate coefficients for formation of the negative ions CN^-, C_2H^-, C_3N^-, C_4H^-, C_5N^-, C_6H^-, C_8H^-, and C_2^- by REA are determined. The obtained results are compared with available experimental data of absolute photodetachment cross sections and previous theoretical calculations performed using the complex Kohn method. The rate coefficients are also computed for these molecules. Chapter 3 presents a theoretical study of dissociative electron attachment cross sections and rate coefficients for molecules ClF/ClF^-. The theoretical results are compared with recent experimental data. In Chapter 4, a theoretical approach to evaluate cross sections for rotational excitation of linear neutral molecules by an electron impact is developed and applied to acetylene, HCCH. The differential cross section, momentum transfer cross section, and eigenphases for e-HCCH scattering are calculated. Finally, in conclusion chapter 5 discusses the results obtained in the thesis.

CHAPTER 2: FORMATION OF ANIONS BY RADIATIVE ELECTRON ATTACHMENT

Molecular Anions: Formation and Destruction

Following the discovery of several molecular anions, C_nN^- ($n = 1, 3, 5$) [34, 35, 36, 37] and C_nH^- ($n = 4, 6, 8$) [38, 39, 36, 40, 41, 37, 42] from several sources in the interstellar medium (ISM), not only mechanism of their formation in the ISM, but also a better understanding of their chemistry received considerable attention. Before the discovery, it was suggested by Herbst that negative molecular ions coud be formed in the ISM by radiative electronic attachment (REA) [43] as the following reaction:

$$e^- + \mathrm{A} \rightarrow \mathrm{A}^- + \mathrm{h}\nu\,, \tag{2.1}$$

where an electron attaches to a neutral species, A, by capture and emits excess energy as radiation [40]. This process can be separated into the following reactions:

$$e^- + \mathrm{A} \rightleftharpoons \mathrm{A}^{-*}\,, \tag{2.2}$$

$$\mathrm{A}^{-*} \rightarrow \mathrm{A}^- + \mathrm{h}\nu\,, \tag{2.3}$$

where A^{-*}, the intermediate anionic complex, either experiences detachment back or stabilizes by photon emission [77].

Generally, the REA process is too slow to produce a substantial number of electronically bound anions M^- in electron-M collisions at thermal energies in the ISM. It is because the Einstein coefficient between the initial continuum state of $e^- + M$ and a bound anion state for spontaneous

emission is very small, resulting in a REA cross section of the order of $(137^3 E_{el})^{-1}$ in atomic units, where E_{el} is the energy of the incident electron in units of hartree. However, Herbst argued that the Einstein coefficient for large molecules could be enhanced significantly if the incident electron is captured by the target neutral molecule M forming a long-lived resonance $(M^-)^*$, such that the molecule becomes vibrationally excited. In order for this to happen at low collision energies, the electronic state of the captured electron should be weakly bound. If the lifetime of $(M^-)^*$ with respect to electron detachment is long enough and comparable to the radiative lifetime for transition to the formed resonance, the $(M^-)^*$ resonance can emit a photon becoming a stable anion M^-. The long autodetachment lifetime of $(M^-)^*$ comparable to the radiative lifetime is one of the two main approximations of this approach, called the phase-space approach (PST). The second important approximation is the unitary probability of forming the resonance $(M^-)^*$ in a single $e^- + M$ collision. There is also a requirement that the energy of the incident electron should match the energy of the $(M^-)^*$ resonance (vibrational Feshbach resonance). It was argued that if the molecule has many vibrational degrees of freedom, such vibrational Feshbach resonances should be present virtually at any collision energy within the relevant characteristic energy interval, which corresponds to $k_B T$, where T is the temperature of the gas. However, the resonance width of $(M^-)^*$ should also be non-negligible for an effective electron capture.

The PST approach, was used in a number of studies [40, 43, 50, 78, 79, 41, 80] to calculate the radiative electron attachment rate coefficients and model formation of the observed anions in the ISM [43, 40, 80, 78, 79, 81]. This approach, which is widely accepted by the astrophysical community was successful explaining the observed column density of C_8H^-, C_6H^-, C_5N^- and C_3N^- ions, while the agreement with observations is not as good for the C_4H^- and CN^- ions [80].

In Herbst notation, the REA process in PST is modeled as follows: First, the electron attaches to the molecule

$$\mathrm{A}(j) + e^- \rightarrow (\mathrm{A}^-\dagger)(j)\,, \tag{2.4}$$

Then, the electron can detach

$$(\mathrm{A}^-\dagger)(j) \rightarrow \mathrm{A}(j) + e^-\,, \tag{2.5}$$

or radiate a photon, bringing the M^- system to a state stable with respect to autodetachment,

$$(\mathrm{A}^-\dagger)(j) \rightarrow \mathrm{A}^-(j') + h\nu\,, \tag{2.6}$$

where the symbol $\dagger$ denotes a complex system, j and j' represent states of rotational angular momentum.

The cross section for the first step, Eq. (2.4), in any state j with momentum $\vec{p} = \hbar\vec{k}$ of the incident electron, is given in PST by

$$\sigma = \frac{\pi\hbar^2}{2m_e E}\,, \tag{2.7}$$

where m_e is the electronic mass, and E is the energy of the collision [40].

The PST assumes that an incoming electron attaches to the molecule with the unitary probability for s-wave scattering but the formed M^- complex is unstable. Once the electron is attached to the radical, the extra energy of the compound can be released via two different competing processes. The first outcome is the autodetachment of the electron from the radical. In PST, the statistical rate coefficient for autodetachment is inversely proportional to the density of states at the total energy of the molecular ion, such that autodetachment should decrease significantly for ions with many degrees of freedom. The second process for energy release, which leads to negative ion stabilization, is radiative relaxation. The ratio between the rate of radiative relaxation and autodetachment represents the key parameter in the PST to determine the total rate of the REA reaction. Therefore,

the PST has a great advantage of providing rates for formation of large negative ions by REA, with only few parameters needed. On the other hand, PST employs some approximations that must be critically revised. Certainly the strongest approximation used in PST is the assumption of 100% efficiency in electronic capture, which could lead to a significantly overestimated REA cross section. Without performing detailed quantum scattering calculations, the relevance of such an approximation is relatively hard to quantify [5].

Using the PST approach, the REA rate coefficients were determined and used to model abundance of observed anions and their neutral counterparts [40]. The obtained abundances agree within a factor 2-4 for large anions, but disagree significantly by factor of 100 or more, for the CN^- and C_4H^- anions [80, 40]. Therefore, the problem of anion formation in the ISM seems to be unresolved given the significant disagreement between PST results and observations and, more importantly, the very crude approximations employed in the PST approach.

Figure. 2.1 schematically shows two possible mechanisms for REA on the example of the CN/CN^- [66]: Direct REA, in which an electron incidents on CN ground vibronic state spontaneously emits a photon of energy $\hbar\omega$ (green arrow) and directly decays to the CN^- ground state. The energy of the photon equals to the difference between the initial total energy of the system E_{tot} (horizontal dashed line) and the energy of CN^- ground state. There is another mechanism for REA, in this thesis it is called indirect REA to distinguish it from the one discussed above. In the indirect DEA, at the first step of the process, the incident electron is captured by non-Born-Oppenheimer coupling into the ground electronic state of CN^- without a photon emission. Because of the conservation in total energy E_{tot}, the vibrational level v^- of CN^- in the first step of the process is highly excited: For low incident energies of the electron, it corresponds to $v^- = 18$ or 19. Next, the electron in an excited vibrational level can either autodetach or stabilize by emitting a photon. The photon changes the rotational and vibrational states of the CN^- molecule. In the second step, the largest probability corresponds to a change of v^- by one quantum, $\Delta v^- = 1$. The dashed red

line presents the derivative of the vibrational ground state wave function of CN, which is involved in the expression for the non-Born-Oppenheimer coupling. Below we discuss only the direct REA, referring it simply as REA.

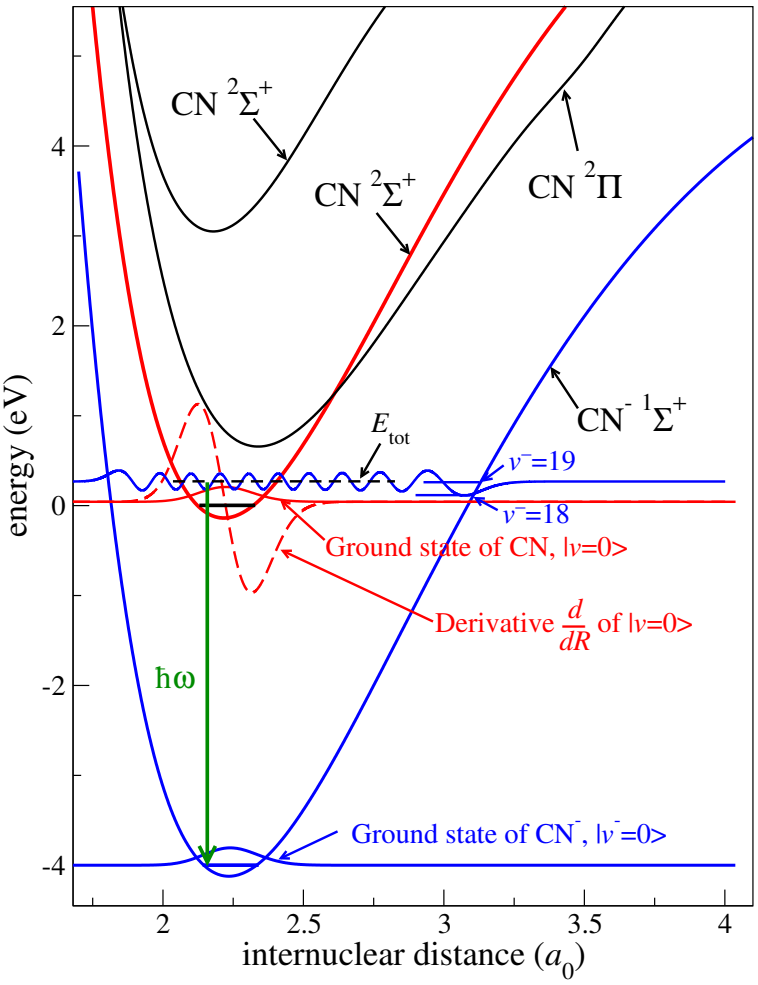

Figure 2.1: Schematic representation of REA on the example of CN/CN$^-$ [66].

Direct Mechanism of Radiative Electron Attachment

In the direct mechanism, the electron during a collision with the molecule emits a photon and forms a negative ion in one of the lowest vibrational levels. The cross section for the radiative electron attachment of the electron to the neutral linear molecule M, such as C_nH ($n = 2, 4, 6, 8$) or C_mN ($m = 1, 3, 5$), which is initially in the $X^1\sum^+$ electronic state with the vibrational level v and energy E_i , is given by [5]

$$\sigma_i \approx \frac{4}{3}\frac{\pi\omega^3 m_e}{k^2\hbar^2c^3}\sum_{l\pi}|d^{(v\to v_f)}_{\pi,\Gamma l-\pi}|^2\,. \tag{2.8}$$

Here, v_f is the vibrational state of the ion M^- with total energy E_f formed after REA and ω is the frequency of the emitted photon, $\hbar\omega = E_i + E_{el} - E_f$; l and λ are the electronic partial wave angular momentum and its projection in the molecular frame respectively; $d^{v\to v_f}_{\pi,\Gamma l\lambda}$ are the components of the transition dipole moment operator with $\pi = -1, 0, +1$ between the initial $\Psi_{\Gamma l\lambda}$ ($M[X^1\sigma^+]$+incident electron) and the final Ψ_f electronic states integrated over the vibrational wave functions of the initial $\chi_v(q)$ and final levels $\chi_{vf}(q)$ of M and M^-, which is given by [5]

$$d^{(v\to v_f)}_{\pi,\Gamma l\lambda} = \int \chi_{v_f}(q)\langle\Psi_f|d_\pi|\Psi_{\Gamma l\lambda}\rangle\chi_v(q)dq\,, \tag{2.9}$$

where q represents all vibrational degrees of freedom.

The matrix elements $\langle\Psi_f|d_\pi|\Psi_{\Gamma l\lambda}\rangle$ of the dipole moment operator are calculated from the electronic wave functions and can be expressed as

$$\langle\Psi_f|d_\pi|\Psi_{\Gamma l\lambda}\rangle = -\sum_{k=1}^{N}\int \Psi^*_f(r_1,\cdots r_N)er_{k\pi}\Psi_{\Gamma l\lambda}(r_1,\cdots r_N)d^3r_1,\cdots d^3r_N\,, \tag{2.10}$$

where $|\Gamma\rangle$ is the initial state of the neutral target and $r_{k\pi}$ is one of the three cyclic components ($\pi = 0,\pm 1$) of the coordinate of the $k^{\rm th}$ electron, which is given by

$$r_{k\pi} = \begin{cases} z_k, & \pi = 0 \\ \mp(x_k \pm i y_k)/\sqrt{2}, & \pi = \pm 1\,. \end{cases} \tag{2.11}$$

The electronic wave functions and transition dipole moments ($\rm TDMs$) of Eq. (2.10), are calculated using R-matrix approach. The matrix elements of the d_x and d_z components of the transition dipole moments between the final state of the CN^- ion and the initial state of the $e^- + \rm CN$ system are shown in the Fig. 2.2 below [5], for several partial waves of the initial wave function as a function of the internuclear distance, and for the energy $\epsilon = 0.25$ eV of the incident electron. The figure shows the weak dependence of the transition-dipole moments with respect to variation of the internuclear distance for the CN/CN^- [5]. In other words, the transition dipole moments depend very weakly on the geometry of the molecule near the equilibrium position.

It is therefore reasonable to simplify the calculation of the vibrational integral of Eq. (2.9), approximating it by a value of $\langle \Psi_f | d_\pi | \Psi_{\Gamma l\lambda} \rangle$ evaluated at the equilibrium of the target molecule,

$$d^{(v\to v_f)}_{\pi,\Gamma l\lambda} \approx \langle \Psi_f | d_\pi | \Psi_{\Gamma l\lambda} \rangle_{\mathcal{Q}_0} \int \chi_{v_f}(q)\chi_v(q) dq\,, \tag{2.12}$$

where the subscript $\mathcal{Q}_0$ refers to the geometry of equilibrium of the target molecule.

For molecules such as $\rm C_nH$ and $\rm C_mN$, for which the potential energy surfaces of the initial electronic state of the target and the final state of the negative ion are similar in shape, the Franck-Condon integral in Eq. (2.12) is the largest for transitions with $v_f = v$, for which the Franck-Condon factor is approximately equal to the unity.

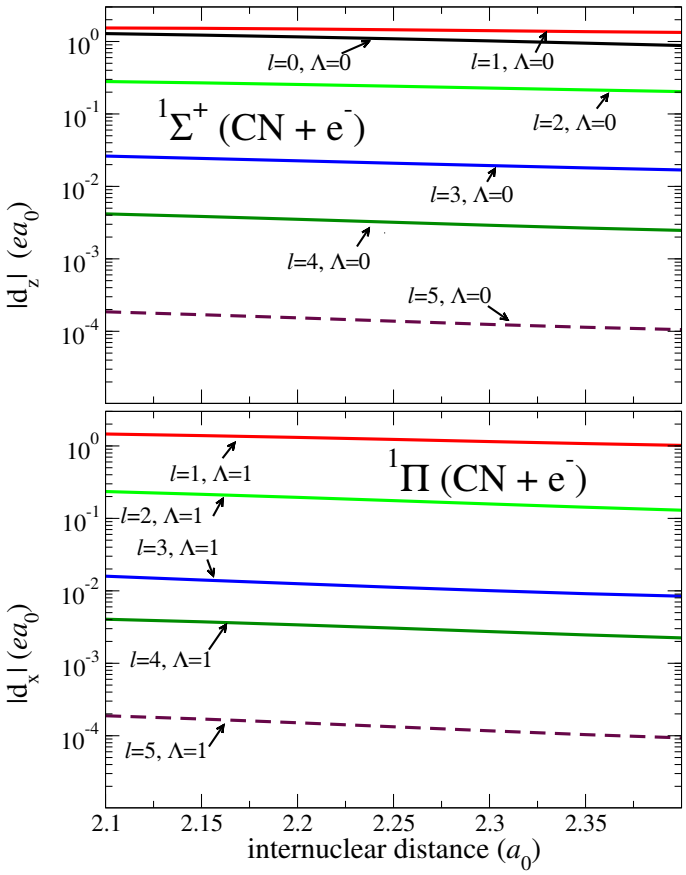

Figure 2.2: The d_x and d_z components of the TDMs as a function of the internuclear distance for R = 0.25 eV [5].

For transitions to other vibrational levels, the integral is significantly smaller. Therefore, the total REA cross section is well approximated by [5]

$$\sigma_i \approx \frac{4}{3}\frac{\pi\omega^3 m_e}{k^2\hbar^2c^3}\sum_{l\pi}\left|\langle\Psi_f|d_\pi|\Psi_{\Gamma l\lambda}\rangle_{\mathcal{Q}_0}\right|^2 , \tag{2.13}$$

This is the formula that will be used to study of REA in my thesis.

There are no experimental measurements of REA cross sections or rate coefficients for the anions observed in the ISM. However, cross sections of the process inverse to REA, photodetachment

(PD), were measured for a number of anions. Theoretically, in the fully-quantum approach cross sections for REA and PD are obtained from the same transition dipole moment (TDM) matrix elements between continuum states of the $M+e^-$ system and bound electronic states of the molecular anion. In a fully-quantum approach, vibrational Feshbach resonances $(M^-)^*$, if vibrational motion is included, are treated in the same way as continuum states of the $M + e^-$ system, i.e. by using TDM elements. The comparison of the PD cross sections obtained theoretically with experimental data allows one to access the accuracy of the calculated TDM elements and, therefore, the validity of the obtained REA cross sections. Theoretically, the PD cross section is obtained using the Eq. (10) of Ref. [66]

$$\sigma_{PD} = \frac{4m_e\pi^2\omega}{3\hbar^2 c}\sum_{l\pi}\left|d^{(v_i\to v_n)}_{\pi,\Gamma l-\pi}\right|^2 , \tag{2.14}$$

where v_i is the vibrational state of the ion M^- with initial energy E_i, v_n is the vibrational state of the final neutral molecule with energy energy E_n; ω is the frequency of the absorbed photon, $\hbar\omega = E_n + E_{el} - E_i$, and E_{el} is the energy of detached photoelectron; The above cross section takes into account averaging over initial rotational states of the negative ion and summation over final possible rotational states of the final neutral molecule. In this case, the TDMs is given by

$$d^{(v_i\to v_n)}_{\pi,\Gamma l\lambda} = \int \chi^*_{v_n}(\vec{q})\langle\Psi_i|d_\pi|\Psi_{\Gamma l\lambda}\rangle\chi_{v_i}(\vec{q})d\vec{q}\,, \tag{2.15}$$

The electronic continuum functions $\Psi_{\Gamma l\lambda}$ in the R-matrix calculations are normalized such that at large distances, the incoming part of the total electronic wave functions behaves as

$$r\Psi_{\Gamma l\lambda} \sim \frac{i}{\sqrt{2\pi k}}e^{-i(kr-\frac{l\pi}{2})}\,. \tag{2.16}$$

Therefore, there is a factor of $\sqrt{\pi/2}$ between the continuum functions used in this study and the

ones used in Refs. [5, 66], where the complex Kohn method and the MESA suite of codes were employed. As a result, Eq. (2.14) above differs from Eq. (10) of Ref. [66] by a factor of $\pi/2$. With respect to the energy-normalized continuum function $\phi_E(r)$, also often used in calculations, $\Psi_{\Gamma l\lambda}$ can be written as

$$\phi_E(r) = \frac{\sqrt{m_e}}{\hbar}\Psi_{\Gamma l\lambda}\,. \tag{2.17}$$

The TDMs then take the simple form

$$d_{\pi,\Gamma l\lambda}^{(v_i\to v_n)} \approx \langle\Psi_i|d_\pi|\Psi_{\Gamma l\lambda}\rangle_{\mathcal{Q}_0}\int \chi_{v_n}^*(\vec{q})\chi_{v_i}(\vec{q})d\vec{q}, \tag{2.18}$$

and the cross section is

$$\sigma_i = \frac{4m_e\pi^2\omega}{3\hbar^2 c}\left|\langle v_n|v_i\rangle\right|^2 \sum_{l\pi}\left|\langle\Psi_i|d_\pi|\Psi_{\Gamma l\lambda}\rangle_{\mathcal{Q}_0}\right|^2\,. \tag{2.19}$$

Similarly to the PD cross section, if the geometry-dependence of transition dipole moments is weak in the Franck-Condon region, the REA cross section can be approximated by

$$\sigma_i \approx \frac{2}{3}\frac{\pi^2\omega^3 m_e}{k^2\hbar^2 c^3}\left|\langle v_n|v_i\rangle\right|^2 \sum_{l\pi}\left|\langle\Psi_i|d_\pi|\Psi_{\Gamma l\lambda}\rangle_{\mathcal{Q}_0}\right|^2\,. \tag{2.20}$$

In this thesis, several processes involving electron-molecule collisions, namely the following reactions, were studied:

$$e^- + \mathrm{C}_n\mathrm{N} \rightarrow \mathrm{C}_n\mathrm{N}^- + \hbar\omega \quad \text{with } n = 1, 3, 5 \quad (\mathrm{REA}); \tag{2.21}$$

$$e^- + \mathrm{C}_n\mathrm{H} \rightarrow \mathrm{C}_n\mathrm{H}^- + \hbar\omega \quad \text{with } n = 2, 4, 6, 8 \quad (\mathrm{REA}); \tag{2.22}$$

$$e^- + \mathrm{ClF} \rightarrow \mathrm{Cl}^- + \mathrm{F} \quad (\mathrm{DEA}); \tag{2.23}$$

$$\rightarrow \mathrm{Cl} + \mathrm{F}^- \quad (\mathrm{DEA})\,. \tag{2.24}$$

For theoretical evaluation of PD and REA cross sections, the continuum electronic functions of the $e^- + M$ system should be calculated. In the previous study [5, 82, 66], the complex Kohn variational method [53, 83, 84, 85] was used. The UK R-matrix approach [59, 86, 87] with Quantemol interface [88] is used in the present thesis. Recently, the possibility of calculation of transition dipole moments was added to the code [87]. The use of the R-matrix approach for these molecules allows us to compare results of two methods and, therefore, validate the photoionization/photodetachment module added recently to the UK R-matrix code. This aspect of the present study appears to us to be also important because the UK R-matrix code is available to the community and can be used by virtually any prepared researcher. Calculating the PD and REA cross sections, it was assumed that the molecules before and after the process are in the ground vibrational levels, $v_n = v_i = 0$.

In the R-matrix calculations the target molecule was represented using the complete active space configuration interaction (CASCI) method build on Hartree-Fock (HF) orbitals. Calculations with different sets of parameters were performed in order to evaluate the uncertainty of the obtained photodetachment results. The following parameters were independently varied for each molecule: (1) the Gaussian basis set, namely, the `DZP` and `cc-PVxZ` bases with x `=D,T,Q`; (2) the number of target states employed in close coupling expansion was varied from 7 to 66; (3) the number of active and (4) virtual states has also been varied; (5) the R-matrix sphere radius was varied in the

interval of 10-15 bohrs. The polarizability and dipole moment of the C_nN ($n = 1, 3, 5$) and C_nH ($n = 2, 4, 6, 8$) molecules were calculated using the `cc-PVQZ` basis with *spdf*-functions and the multi-reference configuration interaction (MRCI). The obtained results for equilibrium geometries, electronic affinity, and the polarizability agree well with available data.

The rest of the chapter discusses applications of the above theoretical approach for determination of cross sections and rate coefficients for formation of C_nN^- ($n = 1, 3, 5$), C_nH^- ($n = 2, 4, 6, 8$), and C_2^- by REA using the treatment presented above. The vibrational resonances are not included into the treatment. However, we would like to mention only that since the electronic state of the formed resonance $(M^-)^*$ is weakly-bound, vibrational modes of the target M and resonance $(M^-)^*$ molecules should be almost identical, which means that the excitation of vibrational modes and formation of vibrational Feshbach resonance should be very ineffective due to a small Franck-Condon overlap between the initial vibrational state of M and the vibrational state of $(M^-)^*$.

CN and CN^-

The CN radical is found in many environments, such as, Sun's atmosphere, terrestrial plasmas, and flames [89]. It is also well-known in study of the cosmic microwave background [90]. It is often used in laboratory experiments, such as photoelectron spectroscopy [91]. The anionic form, CN^-, was the smallest and the first molecular anions to be observed in the interstellar medium [92].

Structure of the CN and CN^- molecules have previously been determined in a number of theoretical and experimental studies. The ground electronic state of CN is $X^2\Sigma^+$ and the only stable electronic state of CN^- is $X^1\Sigma^+$ see the Fig. 2.1. Table 2.1 gives internuclear distances at equilibrium of CN and CN^-, the CN electron affinity (EA), dipole moment, d, and its spherically-averaged polarizability, α, obtained in the present thesis and compared with published data.

Table 2.1: Comparison of electron affinities - EA, dipole moments - d, polarizabilities α, and internuclear distances (in Å) of the CN and CN^- molecules at equilibrium obtained in this thesis and available in the literature.

CN/CN^-	r_{CN} (Å)	EA(eV)	d(D)	α(Å^3)
CN^{-a}	1.182			
prev. calc.	1.177[93]			
CN[a]	1.173	3.8	1.48	2.7
exp.	1.172[94]	3.862±0.004[93]	1.45[95]	
prev. calc.	1.174[96]		1.390[97]	2.884[97]

[a]Calculated in this thesis

In the present thesis, the structure calculations were performed using MOLPRO [98] as discussed in Ref. [5]. For theoretical evaluation of PD and REA cross sections, the continuum electronic functions of the $e^- + M$ system should be calculated. In the previous study [5, 82, 66], the complex Kohn variational method [53, 83, 84, 85] was used. The UK R-matrix approach [59, 86, 87] with Quantemol interface [88] is used in the present thesis. Recently, the possibility of calculation of transition dipole moments was added to the code [87]. The use of the R-matrix approach for the CN and CN^- molecules allows us to compare results of two methods and, therefore, validate the photoionization/photodetachment module added recently to the UK R-matrix code. This aspect of the present study appears to us to be also important because the UK R-matrix code is available to the community and can be used by virtually any prepared researcher.

In the R-matrix calculations the CN target was represented using the complete active space configuration interaction (CASCI) method build on Hartree-Fock (HF) orbitals. Calculations with different sets of parameters were performed in order to evaluate the uncertainty of the obtained results. The final calculation was made with the following parameters: We used the same atomic orbital basis set `cc-PVQZ` as for the polarizability and dipole moment calculations mentioned above. Partial waves with $l = 0 - 4$ (up to the g-wave) functions were included. Four lowest

Hartree-Fock orbitals of the target CN molecule were frozen in the CASCI calculations. The remaining five (out of 13) electrons were distributed over the active space that included seven orbitals and ten virtual orbitals. The virtual orbitals were included in the calculations to improve the electronic continuum states near the target nuclei. The R-matrix sphere radius of 13 bohrs was used.

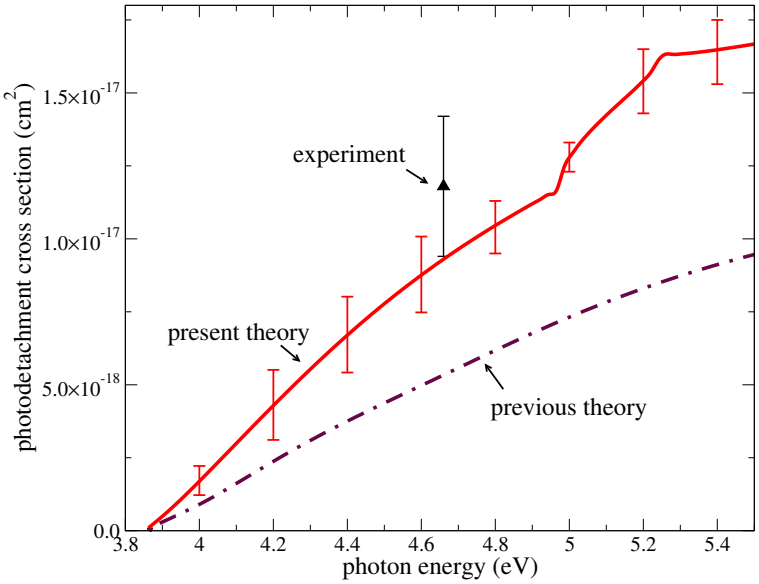

Figure 2.3: Theoretical and experimental photodetachment cross sections for CN^-. The cross section obtained in this thesis (solid red curve) is compared with available experimental data (black triangle) [2] and with the previous theoretical calculation (dot-dashed line) [5] performed using the complex Kohn method. The uncertainty bar of the theoretical cross section is obtained performing calculations for different sets of parameters in the computational model.

In the REA calculations, the initial electronic state is the ground state $X^2\Sigma^+$ of the neutral molecule, the final state of the anion is $X^1\Sigma^+$. In the PD calculations the initial electronic state of CN^- is $X^1\Sigma^+$. For photoelectron energies below 1 eV above the CN+e^- detachment limit, there is only one electronic state open for photodetachment. Therefore, for higher photoelectron energies, where there are more than one electronic channel open for detachment, a sum over all possible electronic final states in the PD cross section calculations is evaluated.

The obtained PD cross section is shown in Fig. 2.3. As mentioned above, calculations with different parameters of the computational model were performed to evaluate uncertainty of obtained theoretical results. The theoretical uncertainty is shown by error bars in the figure. Figure 2.4 shows some of the PD cross sections obtained with different sets of parameters. The uncertainty bars shown in the figure are obtained inspecting the distribution of the cross section values for a given energy value. We stress here that the obtained uncertainty does not account for other sources of uncertainties, for example, associated with neglected rotational structure of initial and final state of the system.

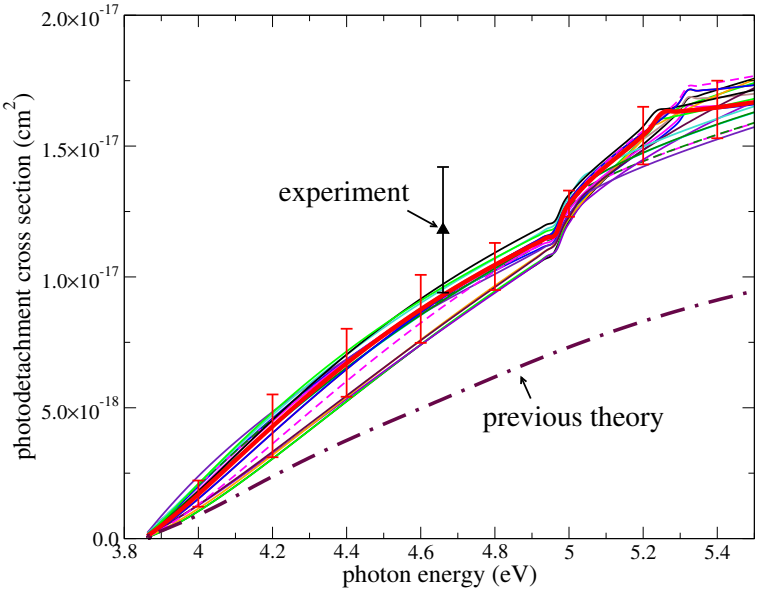

Figure 2.4: The figure shows the same data as in Fig. 2.3 and, in addition, cross sections obtained with different sets of parameters of the computational model.

For CN/CN$^-$, cross sections for the PD or REA processes with a final vibrational level different than the initial vibrational level $v_n \neq v_i$ is much smaller than for the process with $v_n = v_i$.

It is because the electronic potential curves of the ground electronic states of CN and CN^- are almost parallel to each others. The Franck-Condon factor $|\langle v_n|v_i\rangle|^2$ in Eqs. (2.19) and (2.20) with $v_n = v_i = 0$ is equal to 95%. Therefore, neglecting transitions $v_n \leftrightarrow v_i \neq v_n$ in calculations of total PD and REA cross sections (including all possible final vibrational levels) is justified. For the $v_n = v_i$ processes, the vibrational integral in the cross section formulas was performed in two different ways: (a) The integral of Eq. (2.15) was computed explicitly from the geometry-dependent matrix as discussed in Refs. [5, 66] and (b) an approximate formula of Eq. (2.18) was used. Due to a weak dependence of transition dipole moments on molecular geometry near the CN and CN^- equilibrium positions, the difference between the results of the two ways is negligible. It is much smaller than the uncertainty of the cross sections with respect to parameters of the quantum chemistry model discussed above.

The obtained PD cross section agrees with the only experimental data point [2] within experimental and theoretical uncertainties. However, there is an appreciable disagreement, about a factor of 1.7, between the present result and the previous calculations [5, 66], where the complex Kohn variational method was used. Although the source of disagreement is not clear, it is partially explained by combined uncertainties of the present and previous calculations [5], which is about 40%.

The same transition dipole moments between bound and continuum electronic wave functions are used for calculations of the PD and REA cross sections. The REA cross section for formation of CN^- obtained using Eq. (2.20) is shown in Fig. 2.5. The indicated uncertainty bars are obtained using the same procedure as in the PD calculation. Notice that at small electron energies the uncertainty is larger compared to higher collision energies. It is because the larger uncertainty of transition dipole moments is larger for small electron energies. The figure also shows the previous complex Kohn calculations [5]. The agreement between the two results is not perfect but reasonable given the combined uncertainties of the two calculations.

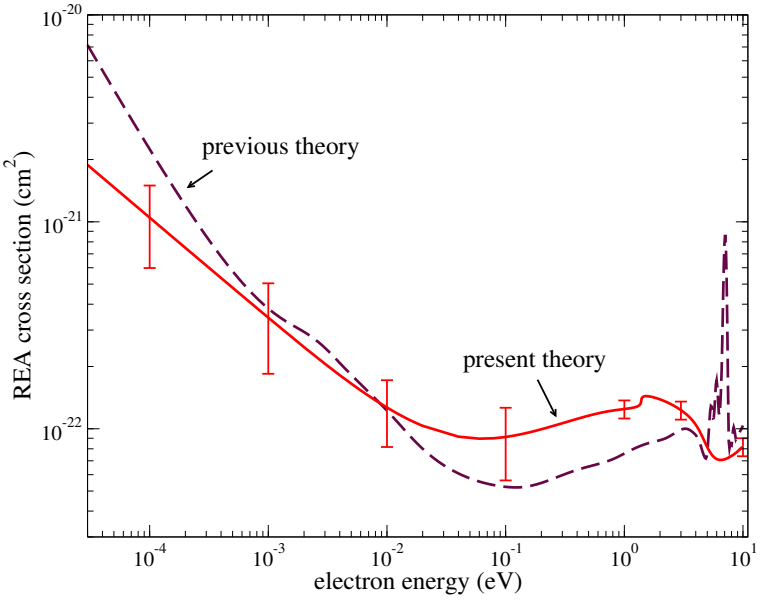

Figure 2.5: Theoretical cross section of of CN^- formation by radiative electron attachment to CN. The figure shows the result of the present calculations and compares it with the previous theory [5].

Figure 2.6 shows rate coefficients for REA to the CN molecule. The coefficient is obtained from cross sections evaluated for a fixed geometry, i.e. such rate coefficients represent the direct REA process in which the final state could be any vibrational level of the formed anion. For the purpose of modeling chemical evolution of interstellar medium, rate coefficients summed over final vibrational states are usually employed. For comparison, the CN coefficient obtained in the previous theoretical study [5] is also shown in the figure. The agreement between the two theoretical results is good.

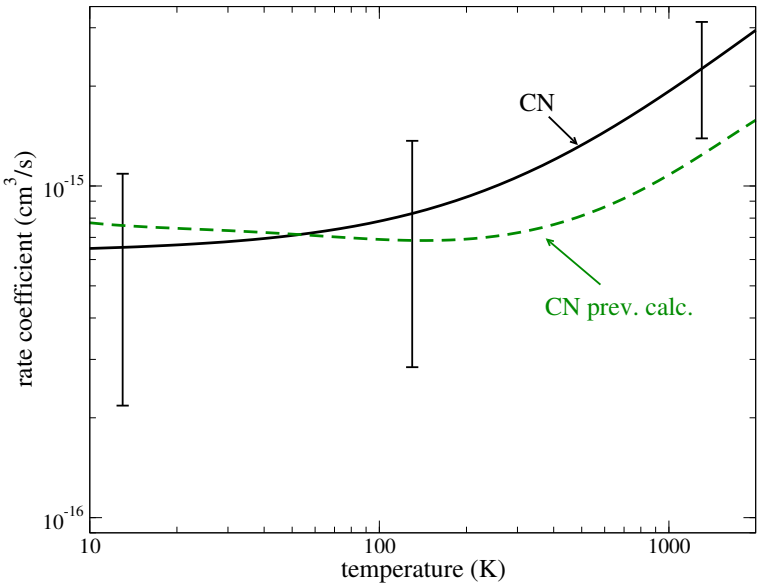

Figure 2.6: Thermally-averaged rate coefficient for radiative electron attachment to CN obtained from cross sections calculated for geometry of equilibrium of CN [94]. The figure also shows the rate coefficient obtained for CN in the previous study [5].

C_2H and C_2H^-

The ethynyl radical, C_2H, is the most studied among the C_nH species and also is one of the most abundant interstellar polyatomic molecules known in the interstellar medium, playing an important role in the formation and destruction of polyynes $H(CC)_n$ in comets and in the interstellar media. It is also important in the laboratory as an intermediate in hydrocarbon reaction systems of chemical processes, including combustion, discharges, and photolysis. In the laboratory, C_2H was first observed in 1963 by Cochran and co-workers [99] by electron spin resonance, and later in 1973 in the gas phase [100]. Subsequently, experimental techniques applied to C_2H (see, for example, Ref. [101] and references therein) and was studied extensively with various experimental and spectroscopic methods [102]. Ethynyl became of interest spectroscopically because of having strong vibronic coupling between the C_2H ground electronic state and the low-lying C_2H excited

state [103].

Table 2.2: Comparison of electron affinities - EA, dipole moments - d, polarizabilities α, and internuclear distances (in Å) of the C_2H and C_2H^- molecules at equilibrium obtained in this thesis and available in the literature.

C_2H/C_2H^-	r_{CC}	r_{CH}	EA(eV)	d(D)	$\alpha(Å^3)$
$C_2H^-(^1\Sigma^+)^a$	1.219	1.057			
prev. calc.	1.22[104]	1.06[104]			
$C_2H(\tilde{X}^2\Sigma^+)^a$	1.177	1.054	2.96	0.87	3.7
exp.			2.96[105]		
prev. calc.	1.207[106]	1.069[106]	2.96±0.04[107]	0.80[97]	4.41[97]

[a] Calculated in this thesis

The structure of the C_2H and C_2H^- molecules were previously determined in a number of theoretical and experimental studies (see [106, 108] and references therein). The ground electronic state of C_2H is $\tilde{X}^2\Sigma^+$ and the ground state of C_2H^- is $\tilde{X}^1\Sigma^+$. Table 2.2 gives internuclear distances at equilibrium of C_2H and C_2H^-, the C_2H electron affinity (EA), dipole moment d, and its spherically-averaged polarizability α, obtained in the present thesis and compared with published data.

The R-matrix calculations performed for the C_2H+e^- collisions are similar to the CN/CN^- calculations. We employed the same atomic orbital basis set `cc-pVQZ` as used to determine the polarizability and the dipole moment presented above. However, partial waves with $l = 0 - 4$ (up to g-wave) functions were included. Four lowest Hartree-Fock orbitals of the target C_2H molecule were frozen in the CASCI calculations.

The remaining five (out of 13) electrons were distributed over the active space that included ten orbitals. Six virtual orbitals were included in the calculations to improve the electronic continuum states near the target nuclei. The radius of the R-matrix sphere was 12 bohrs.

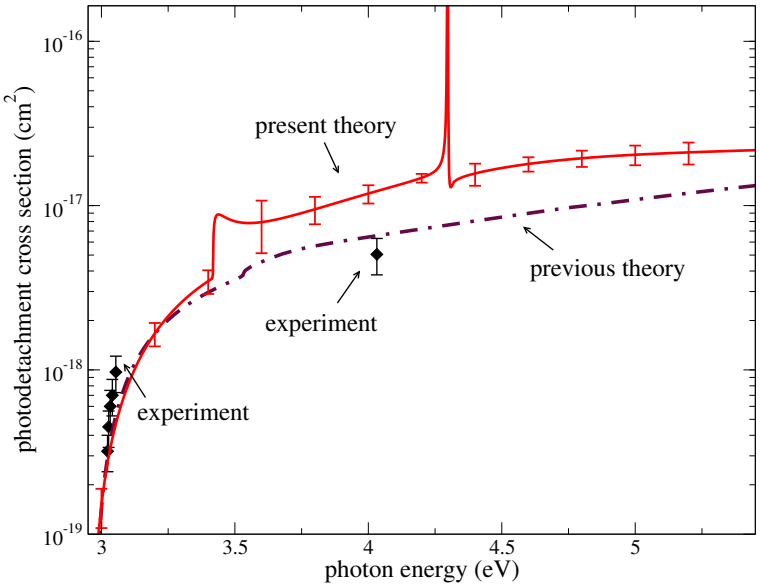

Figure 2.7: Theoretical and experimental photodetachment cross sections for C_2H^-. The cross section obtained in this thesis (solid red curve) is compared with available experimental data (black diamonds) [1] and with the previous theoretical calculation (dot-dashed line) [66] performed using the complex Kohn method. The uncertainty bar of the theoretical cross section is obtained performing calculations for different sets of parameters in the computational model.

In the REA calculations, the initial electronic state is the ground state $\tilde{X}^2\Sigma^+$ of the neutral molecule, the final state of the anion is $\tilde{X}^1\Sigma^+$. In the PD calculations the initial electronic state of C_2H^- is $\tilde{X}^1\Sigma^+$. For photoelectron energies smaller than 0.5 eV above the C_2H+e^- detachment limit, only the electronic ground state $\tilde{X}^1\Sigma^+$ is open for photodetachment, whereas at higher energies, the first excited $\tilde{A}^2\Pi$ electronic state of C_2H becomes opens for detachment. Consequently, for the corresponding energies, a sum over the two possible final electronic states of C_2H in the PD cross section calculations was evaluated.

The obtained PD cross section is depicted in Fig. 2.7. The theoretical uncertainty is shown by error bars in the figure. Figure 2.8 shows some of the PD cross sections obtained with different sets of parameters. The calculated PD cross section agrees well with the experimental data points [1] and previous theoretical result [82] for low photoelectron energies.

For energies above the $\tilde{A}^2\Pi$ detachment threshold, the present cross section is significantly larger than the experimental and complex Kohn results. It suggests that in the present R-matrix calculations, the transition dipole moments into the $\tilde{A}^2\Pi$ state of C_2H are overestimated.

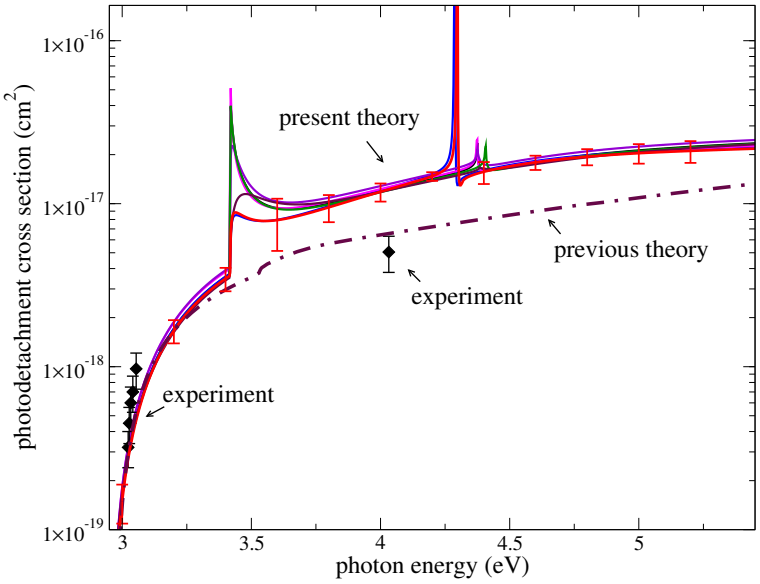

Figure 2.8: Theoretical and experimental photodetachment cross sections for C_2H^-. The figure shows the same data as in Fig. 2.7 and, in addition, cross sections obtained with different sets of parameters of the computational model.

The Franck-Condon factor $|\langle v_n|v_i\rangle|^2$ in Eqs. (2.19) and (2.20) with $v_n = v_i = 0$ is equal to 0.83 for PD to the $\tilde{X}^2\Sigma^+$ state and 0.73 to the $\tilde{A}^2\Pi$ state [82]. The same transition dipole moments between bound and continuum electronic wave functions are used for calculations of the PD and REA cross sections.

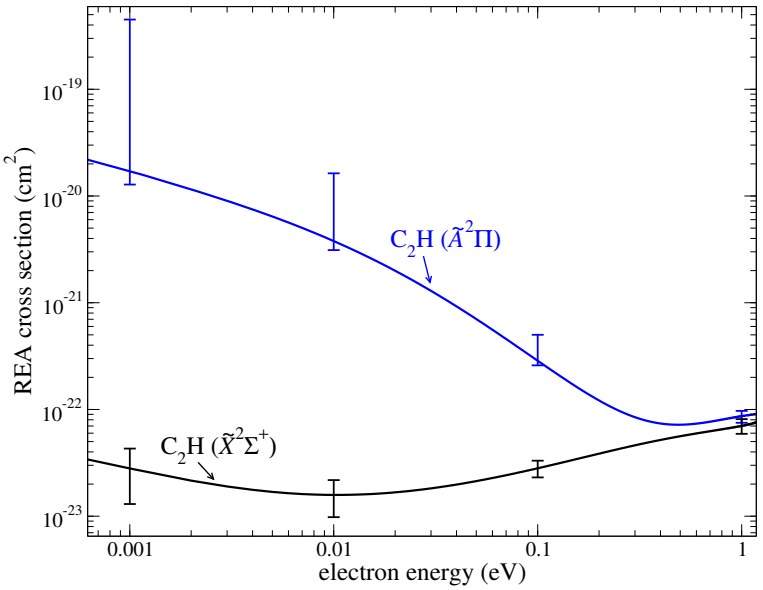

Figure 2.9: Theoretical cross sections of REA to the C_2H molecule. Two different cross sections were calculated: the first one assuming that the target molecule is in the ground electronic state $\tilde{X}^2\Sigma^+$ and the second one assuming the target molecule is in the $\tilde{A}^2\Pi$ state.

The REA cross section for formation of C_2H^- obtained using Eq. (2.20) is shown in Fig. 2.9. The two C_2H^- curves shown in the figure correspond to two different initial electronic states of C_2H. The indicated uncertainty bars are obtained using the same procedure as in the PD calculation. Notice that at small electron energies the relative uncertainty is significantly larger compared to higher collision energies due to the fact that at low electron energies the uncertainty in evaluation of TDMs is large.

Figure 2.10 shows rate coefficient for REA to the C_2H molecule, obtained from cross section evaluated for a fixed geometry. Such rate coefficient represent the REA process in which the final state could be any vibrational level of the formed anion. For the purpose of modeling chemical evolution of interstellar medium, rate coefficient summed over final vibrational states is usually employed.

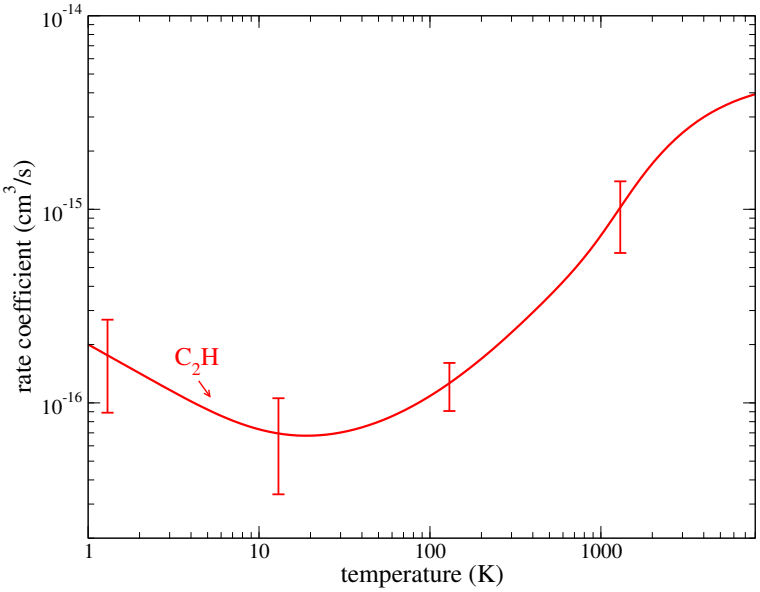

Figure 2.10: Thermally-averaged rate coefficient for radiative electron attachment to C_2H obtained from cross section calculated geometry of equilibrium of C_2H [106].

C_3N and C_3N^-

The cyanoethynyl radical, C_3N, was identified 30 years ago prior to laboratory detection [109]. The negative molecular ion, C_3N^-, was detected in many environments, such as laboratory discharge, the molecular envelope of IRC+10216 [35], and in the dark cloud TMC1 [110]. The C_3N and C_3N^- both have an important role in the interstellar chemistry and also potentially significant constituents of Titan's ionosphere [45]. The interstellar detection of C_3N was confirmed by the observation of the radical in the low-pressure laboratory gas discharge of cyanoacetylene in nitrogen [111]. The electronic structure of C_3N and C_3N^- was determined in a number of theoretical studies (see, for example, Ref. [112] and references therein). Similarly to C_2H and C_2H^-, the ground electronic state of C_3N is $\tilde{X}^2\Sigma^+$ and the ground state of C_3N^- is $\tilde{X}^1\Sigma^+$.

Table 2.3 gives the internuclear distances at equilibrium of C_3N and C_3N^-, the C_3N electron affinity, the dipole moment, and its spherically-averaged polarizability, obtained in the present thesis and previously published. The present PD and REA calculations discussed below were performed for the geometry of C_3N^- equilibrium, obtained in Ref. [113], which is also given in the table 2.3.

Table 2.3: Comparison of electron affinities - EA, dipole moments - d, polarizabilities α, and internuclear distances (in Å) of the C_3N and C_3N^- molecules at equilibrium obtained in this thesis and available in the literature.

C_3N/C_3N^-	$r_{C_1C_2}$	$r_{C_2C_3}$	r_{C_3N}	EA(eV)	d(D)	$\alpha(\text{Å}^3)$
C_3N^- [a]	1.222	1.372	1.173			
exp.	1.252[112]	1.366[112]	1.171[112]			
prev. calc.	1.252[114]	1.366[114]	1.171[114]			
C_3N [a]				4.6	2.66	5.3
exp.	1.217[112]	1.388[112]	1.160[112]	4.305±0.001[112]		
prev. calc.	1.214[113]	1.385[113]	1.162[113]	4.34[114]	2.86[97]	5.6[97]

[a] Calculated in this thesis

Similarly to the previously discussed molecules, the R-matrix calculations were performed for several sets of parameters, and the final calculations were made with the `cc-PVTZ` Gaussian basis set. Ten lowest HF orbitals of the target molecule were frozen. The remaining five (out of 25) electrons were distributed over the active space that included nine orbitals and six virtual orbitals. The R-matrix sphere radius of 13 bohrs was used. As in the case of C_2H/C_2H^-, in the REA calculations, the initial electronic state is the ground state $\tilde{X}^2\Sigma^+$ of the neutral molecule, the final state of the anion is $\tilde{X}^1\Sigma^+$. In the PD calculations the initial electronic state of C_3N^- is $\tilde{X}^1\Sigma^+$. For photoelectron energies above 1 eV, where there are more than one electronic channel open for detachment, a sum over all possible electronic final states in the PD cross section calculations is evaluated.

The Franck-Condon factor between two ground-level vibrational wave functions of C_3N and C_3N^- can be calculated using the expression in Ref. [82]

$$|\langle v_n = 0 | v_i = 0 \rangle|^2 = e^{-\frac{\Delta^2}{2}}, \tag{2.25}$$

where $\Delta^2 = \Delta_1^2 + \Delta_2^2 + ... + \Delta_N^2$ is the distance squared between the minima of the C_3N and C_3N^- potentials in the space of dimensionless normal coordinates. The quantity Δ_i is the distances between the two minima along the normal coordinate i. Therefore, the normal mode coordinates as well as minima of the C_3N and C_3N^- potentials should be calculated, which was made using the MOLPRO code. Deriving the above equation, it was assumed that normal coordinates of the two potentials are the same but equilibrium positions are not. We have verified the accuracy of this assumption performing calculation of the Franck-Condon factor using the C_3N and C_3N^- normal coordinates (which are slightly different). The difference in the result was insignificant compared to the uncertainty of the electron-scattering calculations. For C_3N/C_3N^-, the Franck-Condon factor calculated using Eq. (2.25) is 0.89.

Figure 2.11 shows the C_3N^- photodetachment cross sections and the corresponding uncertainties obtained using the procedure described above. The red (upper) curve represents the result obtained without taking into account the vibrational Franck-Condon overlap. In other words, the curve was calculated assuming that the Franck-Condon factor in Eq. (2.19) is unity. The blue (lower) curve takes into account the Franck-Condon factor of 0.89. This result corresponds to the cross section for photodetachment without change in the vibrational level $v_i = v_n = 0$. In order to obtain the PD cross section with any possible final level v_n, a sum over v_n should be taken in Eq. (2.19). Evaluating the sum, the dependence of ω on v_n should, in principle, be accounted for.

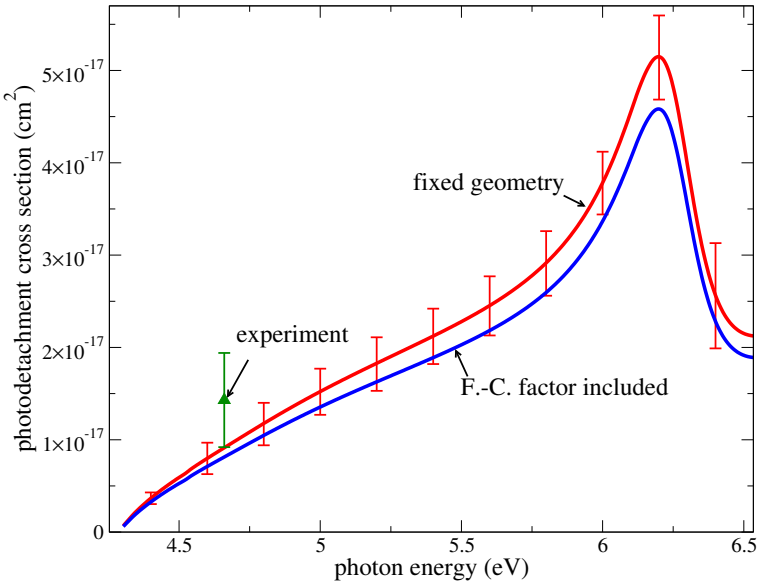

Figure 2.11: C_3N^- photodetachment cross section obtained for a fixed geometry (the red curve) and for the process where the final vibrational level of C_3N is the same as the initial one, $v_i = v_n = 0$ (the blue curve). Available experimental data [2], also shown in the figure, should be compared with the cross section obtained for a fixed geometry (red curve).

However, given the large value of affinity compared to the vibrational splitting between different levels v_n, the dependence is weak and can be neglected when the sum over all v_n is evaluated. TDMs in Eq. (2.19) also change not much over the energy interval of a few vibrational quanta v_n. If the ω and TDM dependences in Eq. (2.19) are neglected, the sum over all v_n of the vibrational overlap gives unity. It brings the PD cross section summed over all possible final vibrational levels v_n to the values calculated as a fixed geometry, i.e. to the values given by the red curve in Fig. 2.11. The figure also shows the available experimental data [2]. In the experiment, the vibrational structure of final states of C_3N was not resolved and, therefore, the experimental data should be compared with the theoretical result represented by the red curve. As one can see, the agreement between theory and experiment is good. It is within theoretical and experimental uncertainty intervals.

The resonance in the PD spectrum around 6.2 eV (Fig. 2.11) is of the $^1\Pi$ overall symmetry of the C_3N+e^- system with three electronic partial waves, $p\pi$, $d\pi$, and $f\pi$ contributing almost equally, respectively, 20%, 20%, and 30% of the total cross section.

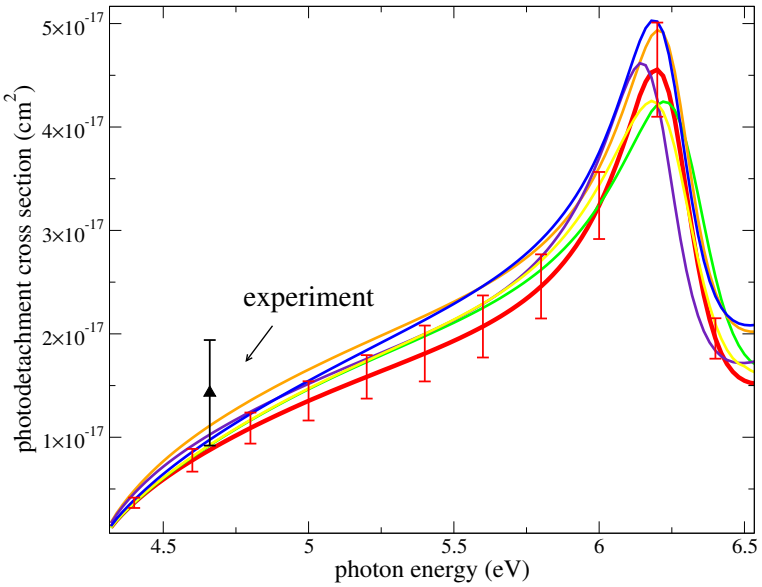

Figure 2.12: The figure shows the same data as in Fig. 2.11 for a fixed geometry and, in addition, cross sections obtained with different sets of parameters of the computational model.

Figure 2.12 shows the same data as in Fig. 2.11 and some of the PD cross sections obtained with different sets of parameters. The theoretical uncertainty is shown by error bars in the figure.

The REA cross section for formation of C_3N^- obtained using Eq. (2.20) is shown in Fig. 2.13. The indicated uncertainty bars are obtained using the same procedure as in the PD calculation.

Figure 2.14 shows rate coefficients for REA to the C_3N molecule. The coefficient is obtained from cross sections evaluated for a fixed geometry. The REA coefficients for the $v_n = 0 \rightarrow v_i = 0$ process can be obtained by multiplying the C_3N values shown in Fig. 2.14 by the factor of 0.89.

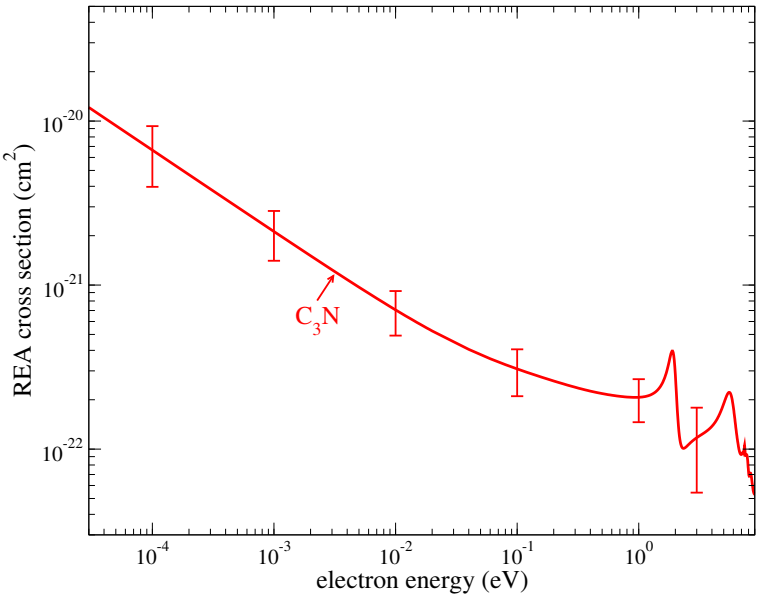

Figure 2.13: Theoretical cross section of of C_3N^- formation by radiative electron attachment to C_3N.

C_4H and C_4H^-

In the ISM, the C_4H radical was among the first molecules to be identified in IRC+10216 [115] even before its laboratory characterization. The anionic form, C_4H^-, was detected in a gas discharge in laboratory [35]. Several laboratory microwave spectroscopy studies were performed on these molecules (see, for example, Ref. [101] and references therein). The electronic structure of C_4H and C_4H^- was determined in previous studies (see, for example, Refs. [116, 117]). Similarly to C_2H/C_2H^-, the ground electronic state of C_4H is $\tilde{X}^2\Sigma^+$ and the ground state of C_4H^- is $\tilde{X}^1\Sigma^+$. The first excited electronic state $\tilde{A}^2\Pi$ of C_4H lies only 0.026 eV above the $\tilde{X}^2\Sigma^+$ state. Table 2.4 gives the internuclear distances at equilibrium of C_4H and C_4H^-, the C_4H electron affinity, the dipole moment, and its spherically-averaged polarizability, obtained in the present thesis or previously published data. The present PD and REA calculations discussed below were performed for the geometry of C_4H^- equilibrium, obtained in Ref. [118], given in the table.

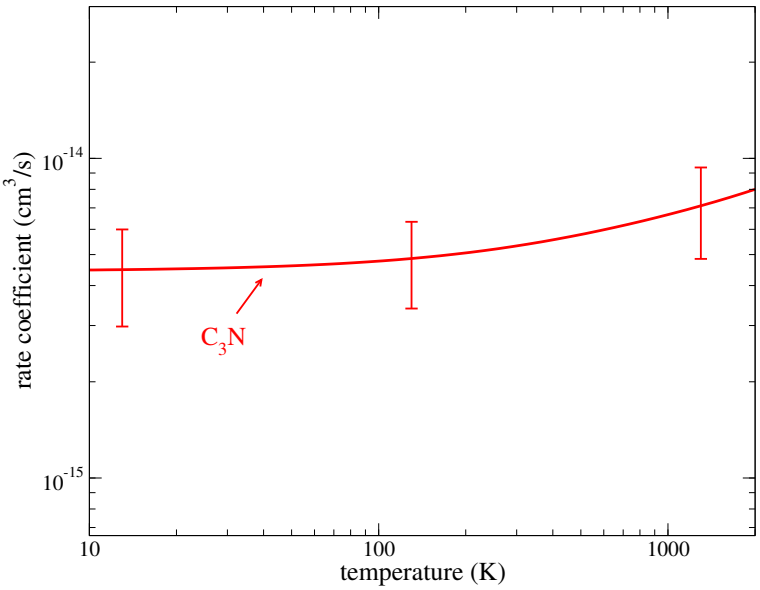

Figure 2.14: Thermally-averaged rate coefficient for radiative electron attachment to C_3N obtained from cross sections calculated for geometry of equilibrium of $C3N^-$ [112].

Table 2.4: Comparison of electron affinities - EA, dipole moments - d, polarizabilities α, and internuclear distances (in Å) of the C_4H and C_4H^- molecules at equilibrium obtained in this thesis and available in the literature.

C_4H/C_4H^-	$r_{C_1C_2}$	$r_{C_2C_3}$	$r_{C_3C_4}$	r_{C_4H}	EA(eV)	d(D)	α(Å^3)
C_4H^{-a}	1.247	1.382	1.193	1.051			
prev. calc.	1.257[117]	1.372[117]	1.226[117]	1.061[117]			
$C_4H(\tilde{X}^2\Sigma^+)^a$	1.207	1.387	1.180	1.053	3.84	0.8	6.5
exp.	1.227[118]	1.359[118]	1.211[118]	1.055[118]	3.55± 0.01[101]		
prev. calc.	1.209[119]	1.385[119]	1.182[119]	1.054[119]	3.46±0.07[107]	0.8[120]	7.1[97]

[a] Calculated in this thesis

The electron scattering calculations were performed in the same way as for the C_2H/C_2H^- pair with the following differences. The final calculation was made with the `cc-PVTZ` Gaussian basis set. Ten lowest HF orbitals of the target molecule were frozen. The remaining five (out of 25) electrons were distributed over the active space that included sixteen orbitals (with ten virtual orbitals). The radius of the R-matrix sphere was 12 bohrs. For C_4H/C_4H^-, the Franck-Condon factor $|\langle v_n|v_i\rangle|^2$

in Eqs. (2.19) and (2.20) is equal to 0.75 for PD to the $\tilde{X}^2\Sigma^+$ state and 0.88 to the $\tilde{A}^2\Pi$ state [82].

Figure 2.15 shows the C_4H^- photodetachment cross sections and the corresponding uncertainties obtained using the procedure described above. The results were obtained without taking into account the vibrational Franck-Condon overlap. In other words, the curve was calculated assuming that the Franck-Condon factor in Eq. (2.19) is unity. The figure also shows the available experimental data [2]. As one can see, the agreement between theory and experiment is reasonable but not perfect. In addition, the results of the complex Kohn method and the R-matrix can differ by a factor larger than five in some energy region.

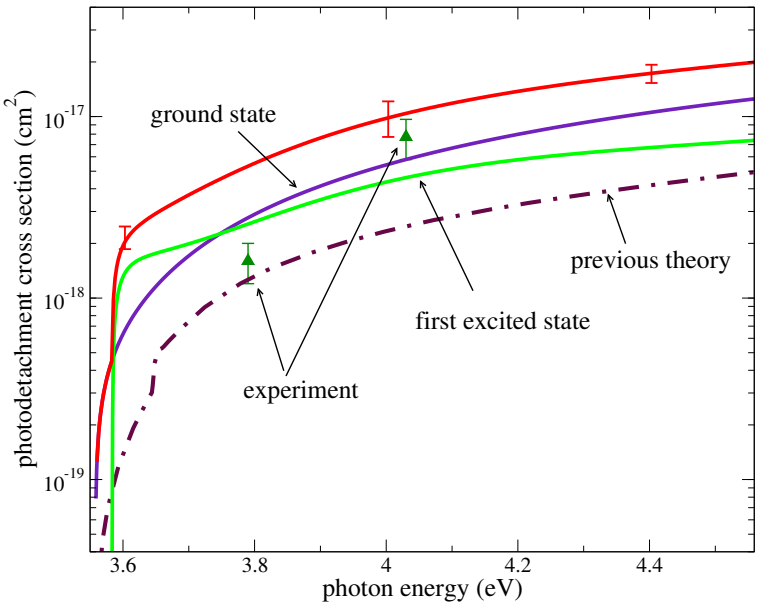

Figure 2.15: C_4H^- photodetachment cross section obtained at a fixed geometry. Available experimental data (green triangle) [1] and results of the previous calculation (dot-dashed line) [82] are also shown.

Figure 2.16 shows the same data as in Fig. 2.15 and some of the PD cross sections obtained with different sets of parameters. The theoretical uncertainty is shown by error bars in the figure.

The REA cross section for formation of C_4H^- obtained using Eq. (2.20) is shown in Fig. 2.17. The

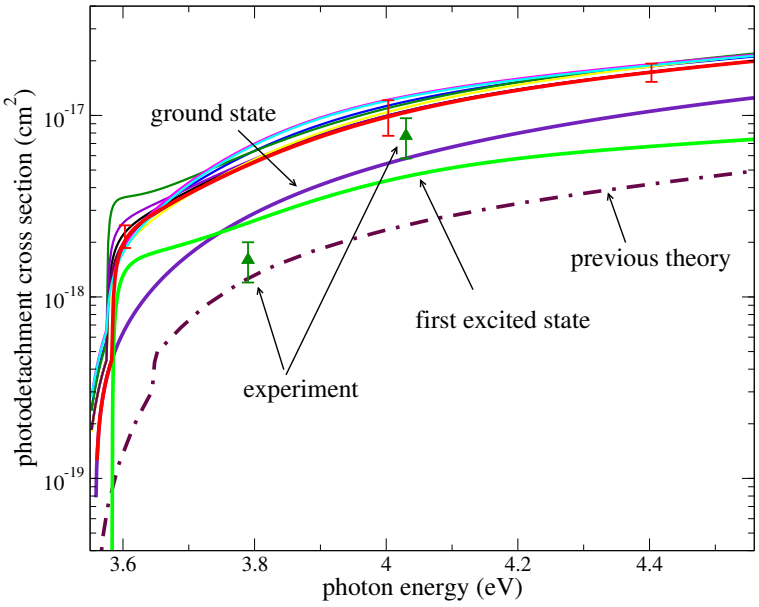

Figure 2.16: The figure shows the same data as in Fig. 2.15 and, in addition, cross sections obtained with different sets of parameters of the computational model.

two C_4H^- curves shown in the figure correspond to two different initial electronic states of C_4H. The indicated uncertainty bars are obtained using the same procedure as in the PD calculation. Notice that at small electron energies the relative uncertainty is significantly larger compared to higher collision energies due to the fact that at low electron energies the uncertainty in evaluation of TDMs is large.

The obtained REA cross sections were used to determine REA thermally-averaged rate coefficients. For C_4H, the excited electronic $\tilde{A}^2\Pi$ state is only 0.026 eV above the ground state. Therefore, at low temperatures it can be populated and should be accounted in rate coefficient calculations.

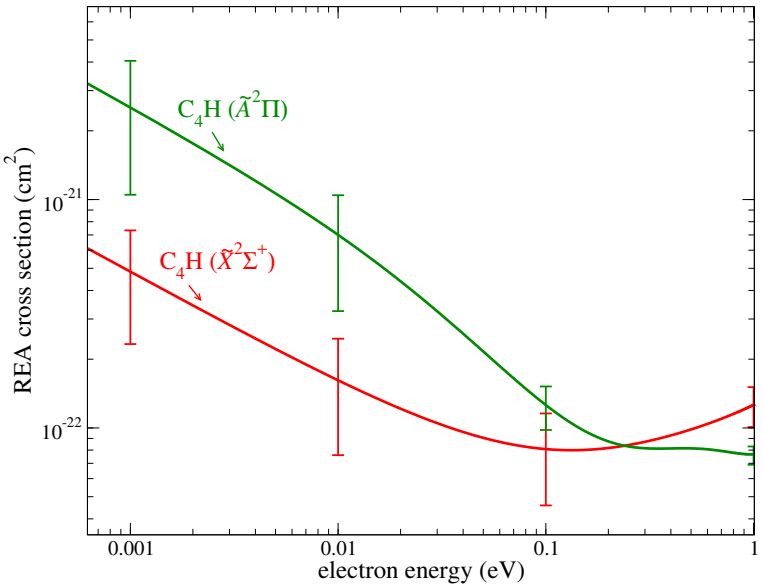

Figure 2.17: Theoretical cross sections of REA to the C_4H molecule. Two different cross sections were calculated: the first one assuming that the target molecule is in the ground electronic state $\tilde{X}^2\Sigma^+$ and the second one assuming the target molecule is in the $\tilde{A}^2\Pi$ state.

The rate coefficient for this situation is calculated using the following integral [121] (in atomic units)

$$\alpha(T) = \frac{1}{N}\int_0^\infty \sum_{s=\tilde{X},\tilde{A}} \sigma_s(E_{el})\omega(s,T)E_{el}dE_{el}, \tag{2.26}$$

where the normalization constant N and the statistical factors $\omega(s,T)$ are

$$N = \int_0^\infty \sum_{rv} \omega(s,T)\sqrt{\frac{E_e l}{2}}dE_{el}, \tag{2.27}$$

$$\omega(\tilde{X},T) = \exp(-\frac{E_{el}}{kT}), \tag{2.28}$$

$$\omega(\tilde{A},T) = 2\exp(-\frac{\Delta_E}{kT})\exp(-\frac{E_{el}}{kT}), \tag{2.29}$$

and Δ_E is the difference between energies of the $\tilde{A}^2\Pi$ and $\tilde{X}^2\sum^+$ states. Using the above equations, the rate coefficients were calculated from the cross sections at fixed geometry.

Such rate coefficients represent the REA process in which the final state could be any vibrational level of the formed anion. For the purpose of modeling chemical evolution of interstellar medium, rate coefficients summed over final vibrational states are usually employed. Figs. 2.10 and 2.18 show the obtained rate coefficients for C_2H and C_4H.

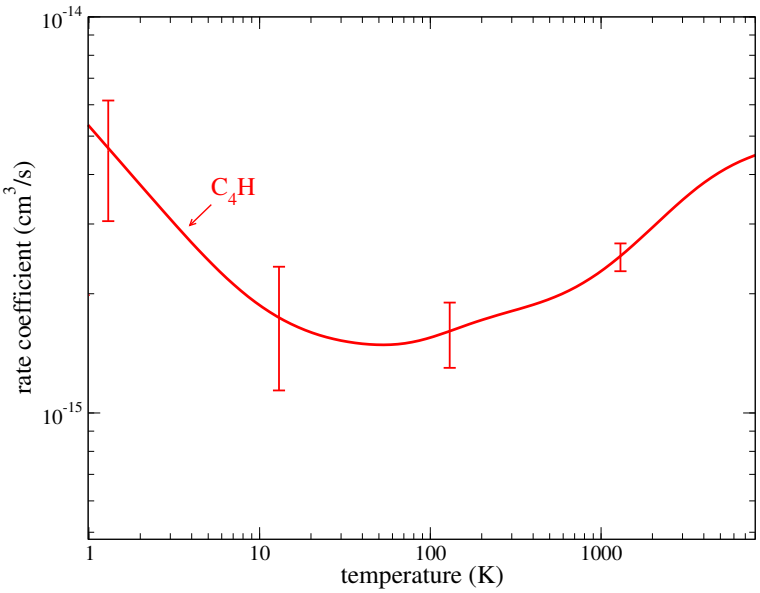

Figure 2.18: Thermally-averaged rate coefficient for radiative electron attachment to C_4H obtained from cross section calculated for geometry of equilibrium of C_4H [118].

Figure 2.18 shows rate coefficient for REA to the C_4H molecule, obtained from cross section evaluated for a fixed geometry.

C_5N and C_5N^-

Carbon chain radical, C_5N, was detected in the dark cloud TMC1 and also in the circumstellar envelope IRC+10216 [122]. It was detected for the first time by using a pulsed-discharge nozzle Fourier transform microwave spectrometer [123]. Electronic structure calculations were also performed for C_5N and C_5N^- [124]. For about two decades, the electronic structure of C_5N and C_5N^- has been a matter of some disagreement (see the discussion in Ref. [112]). Only quite recently, it has finally been established that, similarly to C_3N and C_3N^-, the ground electronic states of C_5N and C_5N^- are $\tilde{X}^2\Sigma^+$ and $\tilde{X}^1\Sigma^+$ respectively. Table 2.5 gives properties of C_5N and C_5N^-, obtained in this thesis or previously published. In the same manner as in the case of C_3N/C_3N^-, the present PD and REA calculations were performed for the geometry of C_5N^- equilibrium [124] given in the table. Also, the target was represented using CASCI with HF orbitals. Assessment of uncertainty was performed in the same way as for the other molecules. The final calculation was made with the following parameters: The `cc-PVTZ` basis with partial waves up to the g-wave was used. Sixteen lowest Hartree-Fock orbitals of the target molecule were frozen. The remaining five (out of 37) electrons were distributed over the active space that included nine orbitals and five virtual orbitals. The radius of the R-matrix sphere was 15 bohrs. Similarly to CN/CN^-, in the REA calculations, the initial electronic state is the ground state $\tilde{X}^2\Sigma^+$ of the neutral molecule, the final state of the anion is $\tilde{X}^1\Sigma^+$. In the PD calculations the initial electronic state of C_3N^- is $\tilde{X}^1\Sigma^+$. In the case of C_5N, the first excited electronic state at the geometry of equilibrium is relatively high, around 2.5 eV above the detachment threshold. Our calculations have not been performed at such energies. Correspondingly, there is only one possible final state in the PD calculations for C_5N^-.

Similarly to C_3N^-, we have evaluated the Franck-Condon vibrational factor calculating the C_5N^- PD cross section for the $v_i = 0 \rightarrow v_n = 0$ process. The obtained value of the factor is 0.78. Figure 2.19 shows the C_5N^- photodetachment cross sections and the corresponding uncertainties.

Table 2.5: Comparison of electron affinities - EA, dipole moments - d, polarizabilities α, and internuclear distances (in Å) of the C_5N and C_5N^- molecules at equilibrium obtained in this thesis and available in the literature.

C_5N/C_5N^-	$r_{C_1C_2}$	$r_{C_2C_3}$	$r_{C_3C_4}$	$r_{C_4C_5}$	r_{C_5N}	EA(eV)	d(D)	α(Å^3)
C_5N^- [a]	1.227	1.357	1.198	1.384	1.137			
exp.	1.258[112]	1.345[112]	1.231[112]	1.357[112]	1.170[112]			
prev. calc.	1.258[124]	1.345[124]	1.231[124]	1.357[124]	1.170[124]			
C_5N [a]						4.48	3.5	9.2
exp.	1.247[112]	1.299[112]	1.230[112]	1.308[112]	1.148[112]	4.45±0.03[112]		
prev. calc.	1.214[125]	1.366[125]	1.212[125]	1.371[125]	1.161[125]	4.45[112]	3.3[97]	9.4[97]

[a] Calculated in this thesis

The notations are the same as in Fig. 2.11. To our knowledge, there is no experimental PD cross section for the C_5N^- anion. The resonance in the C_5N^- PD spectrum around 5.1 eV is of the $^1\Pi$ overall symmetry with the major contribution from the $p\pi$ and $d\pi$ partial waves.

Figure 2.20 shows the same data as in Fig. 2.19 and some of the PD cross sections obtained with different sets of parameters. The theoretical uncertainty is shown by error bars in the figure.

The REA cross section for formation of C_5N^- obtained using Eq. (2.20) is shown in Fig. 2.21. The indicated uncertainty bars are obtained using the same procedure as in the PD calculation.

Figure 2.22 shows rate coefficients for REA to the C_5N molecule. The coefficient is obtained from cross sections evaluated for a fixed geometry. The REA coefficients for the $v_n = 0 \rightarrow v_i = 0$ process can be obtained by multiplying the C_5N values shown in Fig. 2.22 by the factor of 0.78.

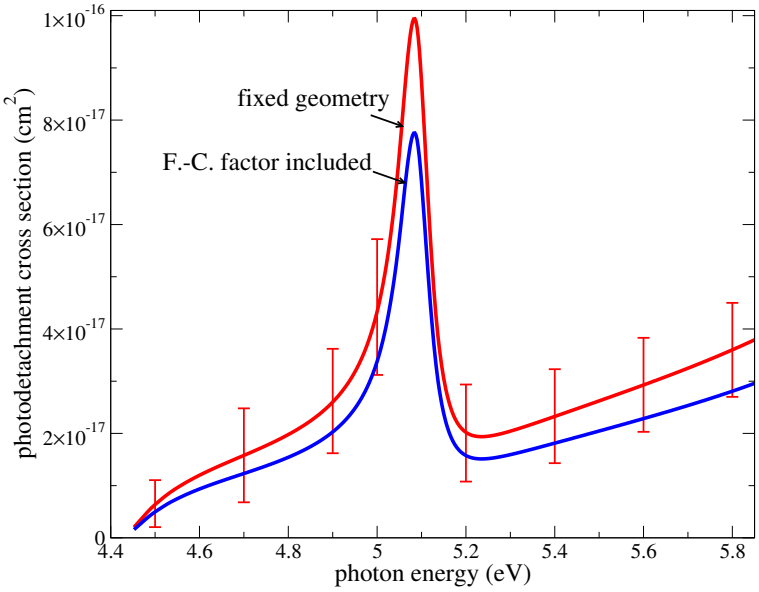

Figure 2.19: C_5N^- photodetachment cross section obtained for a fixed geometry (the red curve) and for the process where the final vibrational level of C_5N is the same as the initial one, $v_i = v_n = 0$ (the blue curve).

C_6H and C_6H^-

The C_6H^- was the first anion detected in space by McCarthy [126], in the radio band in the laboratory and in the molecular envelope of IRC+10216. It was also identified in the dense molecular cloud TMC-1 [126]. The ground electronic state of C_6H is $^2\Pi$. Table 2.6 gives properties of C_6H and C_6H^-, obtained in this thesis. In the same manner as in the case of C_4H/C_4H^-, the present PD and REA calculations were performed for the geometry of C_6H^- equilibrium [118] given in the table. Also, the target was represented using CASCI with HF orbitals. Assessment of uncertainty was performed in the same way as for the other molecules. The final calculation was made with the following parameters: The `cc-PVDZ` basis with partial waves up to the g-wave was used. Sixteen lowest Hartree-Fock orbitals of the target molecule were frozen. The remaining five (out of 37) electrons were distributed over the active space that included ten orbitals and five virtual orbitals.

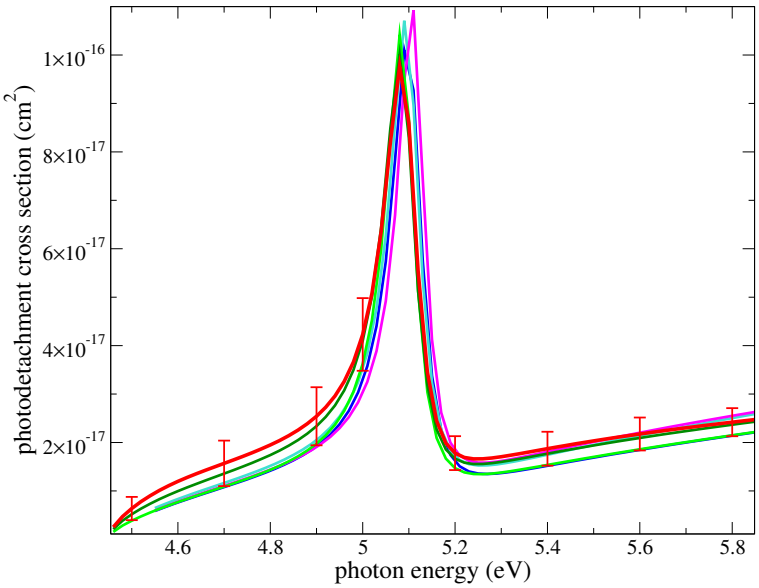

Figure 2.20: The figure shows the same data as in Fig. 2.19 and, in addition, cross sections obtained with different sets of parameters of the computational model.

The radius of the R-matrix sphere was 15 bohrs. The geometry of equilibrium of C_6H [118] was used. Similarly to C_4H/C_4H^-, in the REA calculations, the initial electronic state is the ground state $\tilde{X}^2\Sigma^+$ of the neutral molecule, the final state of the anion is $\tilde{X}^1\Sigma^+$.

Table 2.6: Comparison of electron affinities - EA, dipole moments - d, polarizabilities α, and internuclear distances (in Å) of the C_6H and C_6H^- molecules at equilibrium obtained in this thesis and available in the literature.

C_6H/C_6H^-	$r_{C_1C_2}$	$r_{C_2C_3}$	$r_{C_3C_4}$	$r_{C_4C_5}$	$r_{C_5C_6}$	r_{C_6H}	EA(eV)	d(D)	α(Å^3)
C_6H^- [a]	1.226	1.363	1.199	1.373	1.189	1.067			
prev. calc.									
C_6H [a]	1.180	1.381	1.183	1.380	1.185	1.053		2.1	12.8
exp.	1.257[118]	1.332[118]	1.237[118]	1.341[118]	1.216[118]	1.056[118]	3.8±0.01[101]	4.7[127]	13.6[97]
prev. calc.	1.299[128]	1.327[128]	1.242[128]	1.354[128]	1.221[128]	1.065[128]			

[a] Calculated in this thesis

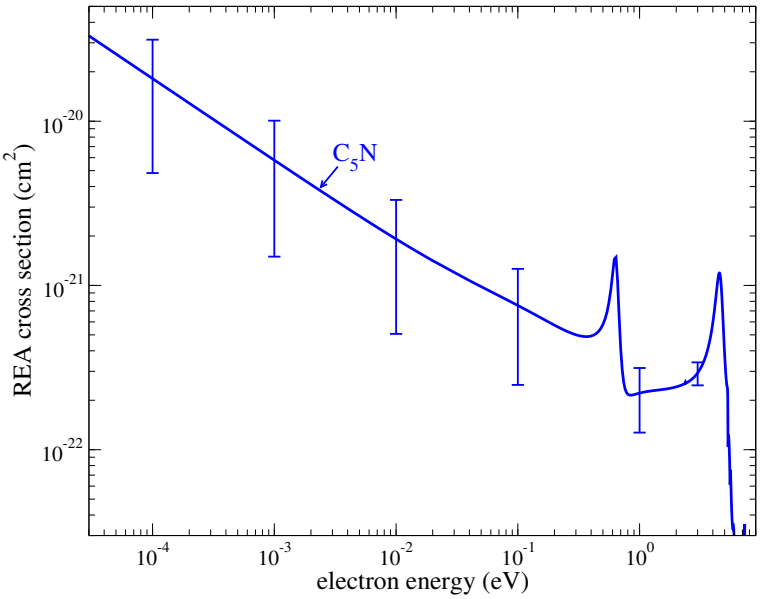

Figure 2.21: Theoretical cross section of of C_5N^- formation by radiative electron attachment to C_5N.

Similarly to C_4H^-, the Franck-Condon vibrational factor was evaluated calculating the C_6H^- PD cross section for the $v_i = 0 \rightarrow v_n = 0$ process. The obtained value of the factor is 0.78 for the ground state [82], but the Franck-Condon for the excited state was not calculated. Figure 2.23 shows the C_6H^- photodetachment cross sections at a fixed geometry and the corresponding uncertainties.

Figure 2.24 shows the same data as in Fig. 2.23 and some of the PD cross sections obtained with different sets of parameters. The theoretical uncertainty is shown by error bars in the figure. For C_6H^- more calculations are needed because results are not converged.

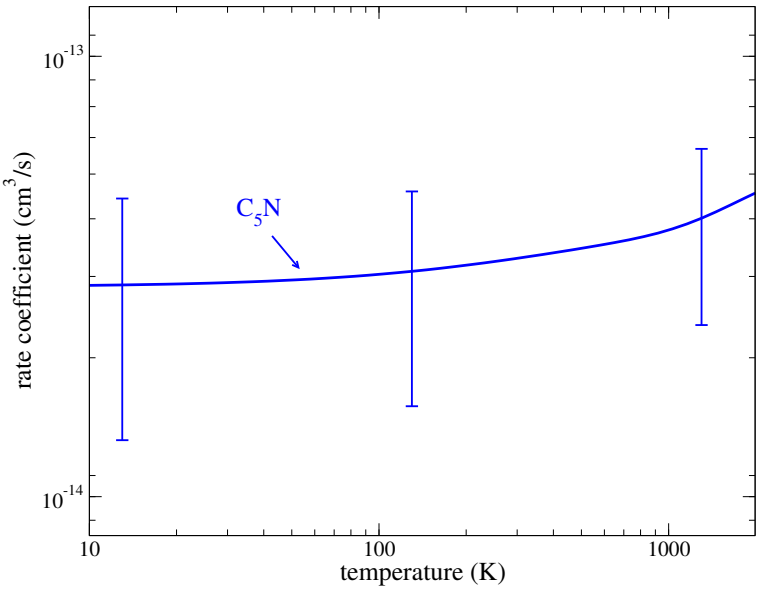

Figure 2.22: Thermally-averaged rate coefficient for radiative electron attachment to C_5N obtained from cross sections calculated geometry of equilibrium of C_5N^- [112].

C_8H and C_8H^-

The octatetranyl anion, C_8H^-, was observed in the Galactic molecular source TMC-1 [129]. Having large dipole moment and also high binding energy makes C_8H^- a good candidate for astronomical detection [38]. Some experimental measurements were performed for C_8H^-, such as anion photoelectron spectra [101]. The electronic spectra of the C_8H^- also was observed in the gas phase using photodetachment spectroscopy [127]. The electronic structure of C_8H and C_8H^- was determined in a number of theoretical studies (see, for example, Ref. [127] and references therein). The ground electronic state of C_8H is $^2\Pi$. Table 2.7 gives the internuclear distances at equilibrium of C_8H and C_8H^-, the C_8H electron affinity, the dipole moment, and its spherically-averaged polarizability, obtained in the present thesis. The present PD and REA calculations discussed below were performed for the geometry of C_8H equilibrium in Ref. [97].

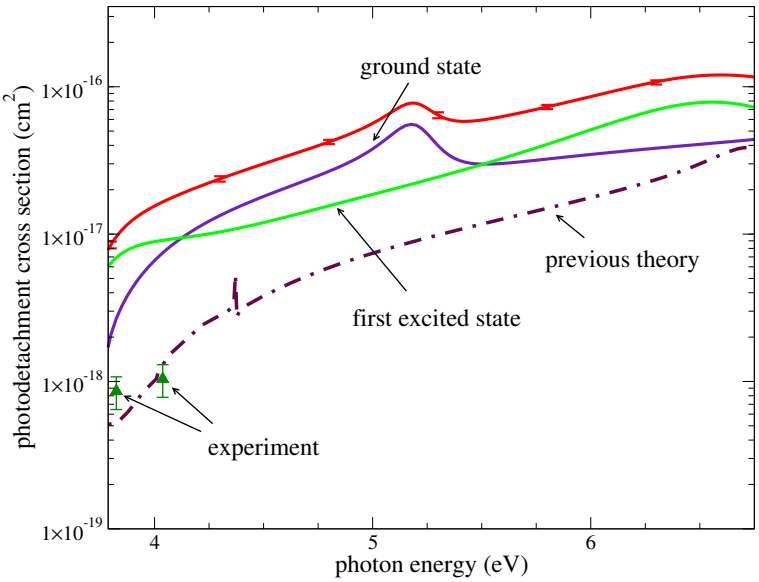

Figure 2.23: C_6H^- photodetachment cross section obtained at a fixed geometry. Available experimental data (green triangle) [1] and results of the previous calculation (dot-dashed line) [82] are also shown.

The same as the other molecules, calculations with different sets of parameters were performed in order to evaluate the uncertainty of the obtained results. The final calculation was made with the following parameters: We used the same atomic orbital basis set `cc-PVTZ` as for the polarizability and dipole moment calculations mentioned above. Partial waves with $l = 0 - 4$ functions were included. Twenty two lowest Hartree-Fock orbitals of the target C_8H molecule were frozen in the CASCI calculations. The remaining five (out of 49) electrons were distributed over the active space that included ten orbitals and five virtual orbitals. The virtual orbitals were included in the calculations to improve the electronic continuum states near the target nuclei. The R-matrix sphere radius of 15 bohrs was used.

Figure 2.25 shows the C_8H^- photodetachment cross sections at a fixed geometry and the corresponding uncertainties obtained using the UK R-matrix code. To our knowledge, there is no experimental PD cross section for the C_8H^- anion.

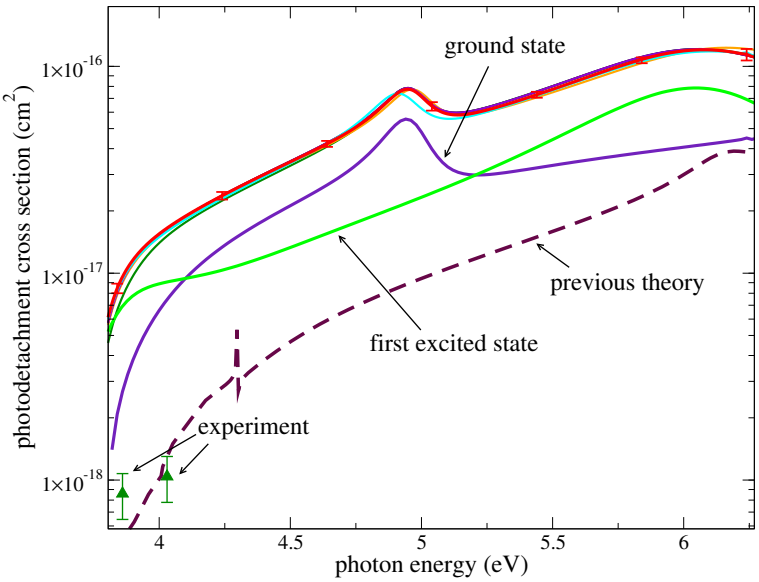

Figure 2.24: The figure shows the same data as in Fig. 2.23 and, in addition, cross sections obtained with different sets of parameters of the computational model.

Table 2.7: Comparison of electron affinities - EA, dipole moments - d, polarizabilities α, and internuclear distances (in Å) of the C_8H and C_8H^- molecules at equilibrium obtained in this thesis and available in the literature.

C_8H/C_8H^-	$r_{C_1C_2}$	$r_{C_2C_3}$	$r_{C_3C_4}$	$r_{C_4C_5}$	$r_{C_5C_6}$	$r_{C_6C_7}$	$r_{C_7C_8}$	r_{C_8H}	EA(eV)	d(D)	α(Å^3)
C_8H^- [a]	1.22	1.35	1.20	1.36	1.19	1.37	1.18	1.05			
prev. calc.	1.25[130]	1.36[130]	1.23[130]	1.36[130]	1.22[130]	1.37[130]	1.21[130]	1.06[130]			
C_8H [a]	1.18	1.38	1.18	1.37	1.18	1.37	1.18	1.05		2.9	18.3
exp.									3.9±0.01[101]	5.26[127]	21.82[97]
prev. calc.	1.31[97]	1.34[97]	1.26[97]	1.35[97]	1.24[97]	1.37[97]	1.23[97]	1.08[97]			

[a] Calculated in this thesis

Figure 2.26 shows the same data as in Fig. 2.25 and some of the PD cross sections obtained with different sets of parameters. The theoretical uncertainty is shown by error bars in the figure.

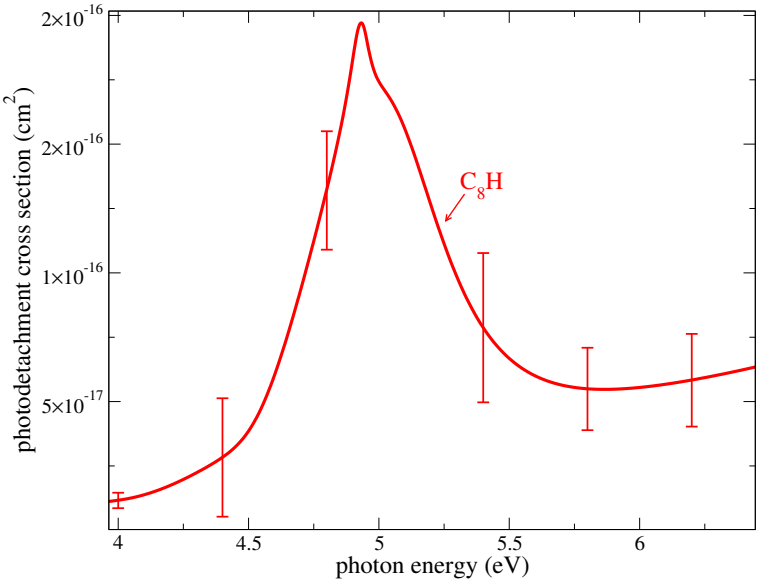

Figure 2.25: C_8H^- photodetachment cross section at a fixed geometry using the UK R-matrix code and the corresponding uncertainties.

C_2 and C_2^-

Collisions of electrons with small molecules containing carbon atoms play an important role in a number of physical and chemical processes such as lasers, gas discharges, and combustion chemistry [131, 132, 133, 134]. In particular, C_2, the smallest carbon chain found in space, is one of such molecules. Its spectrum is recognized in cometary tails, in the atmospheres of cool carbon stars, and also in flames [135]. Employment of the carbon-based materials including graphite in fusion experiments [136], such as graphite walls in fusion devices [136] is one of the applications of C_2, which has recently became of particular interest. The advantage of carbon-based materials used as wall materials in fusion devices is the high thermal conductivity, such as the capability to endure high heat loads appearing in the divertor region [136].

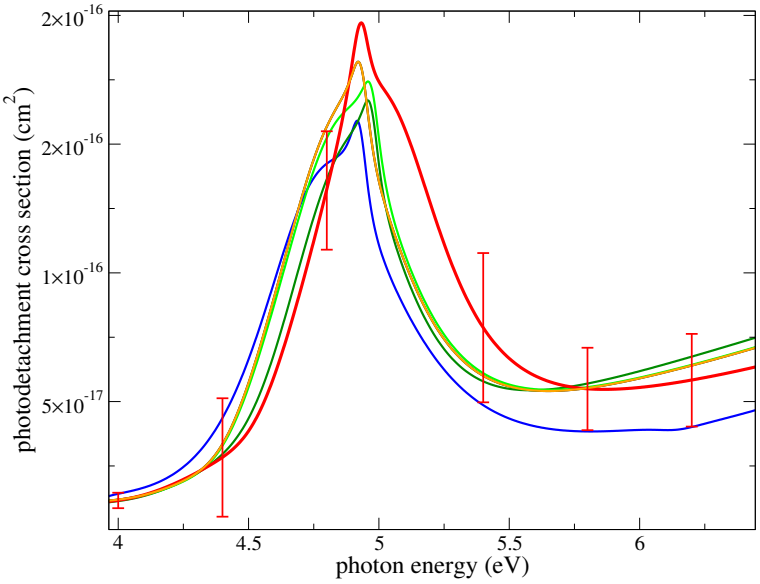

Figure 2.26: The figure shows the same data as in Fig. 2.25 and, in addition, cross sections obtained with different sets of parameters of the computational model.

Knowledge of cross sections for such electron collisional process is required for this and other applications. Studying electron collisions with C_2 is challenging experimentally also difficult to represent using standard *ab initio* methods, because of the large number of low-lying electronic states of the system [135].

The ground state of C_2 molecule is $X^1\sum_g^+$. The electron affinity of dicarbon was measured to be $3.269 \pm 0.006\,\mathrm{eV}$ [103]. Our result, $3.2393\,\mathrm{eV}$, obtained using the MOLPRO code, is in agreement with the experiment. We made e - C_2 scattering calculations in order to determine PD cross sections for C_2^- molecule. Figure 2.27 shows the PD cross sections calculated for C_2^- for different parameters. The internuclear distances at equilibrium of equilibrium of C_2^- was used [137]. The red curve represents the results with the following parameters: We used the `cc-PVQZ` atomic orbital basis set. Partial waves with $l = 0 - 4$ functions were included. Three lowest HF orbitals of the C_2 molecule were frozen in the CASCI calculations. The remaining six (out

of 12) electrons were distributed over the active space that included eleven orbitals. Ten virtual HF orbitals were included in calculations to improve the electronic continuum states in the inner region. The R-matrix sphere radius of 12 bohrs was used.

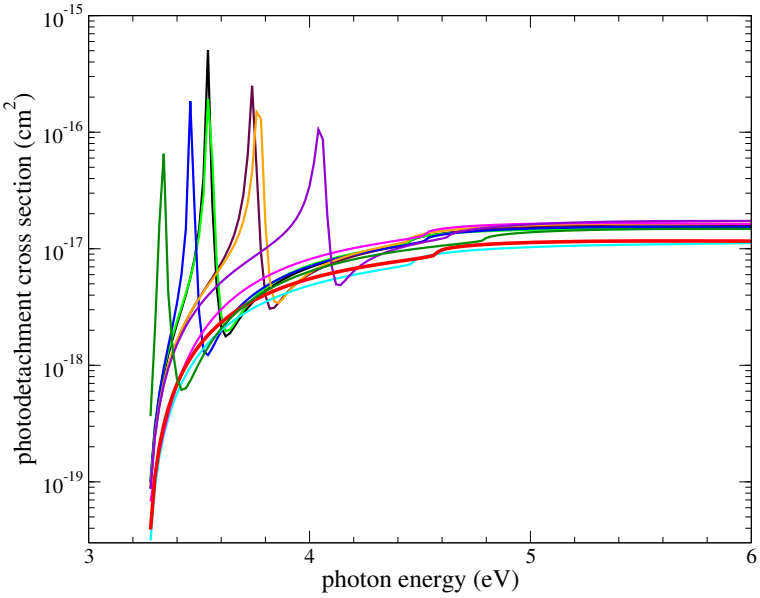

Figure 2.27: Theoretical photodetachment cross section for C_2^-. The cross sections obtained with different sets of parameters of the computational model.

These cross sections demonstrate that the position of the resonance depends on internuclear distance and for a larger orbital space the resonance goes into the discrete spectrum, i.e it becomes a bound state. When the molecule vibrates, the photodetachment cross section will be a sort of an average over the interval of geometries where the resonance is present and the region where it is absent.

Figure 2.28 shows the electronic potential energy curves of C_2 and C_2^- molecules, which was calculated using the `d-aug-pVQZ` atomic orbital basis set with spd-functions using the multi-reference configuration interaction (MRCI) method.

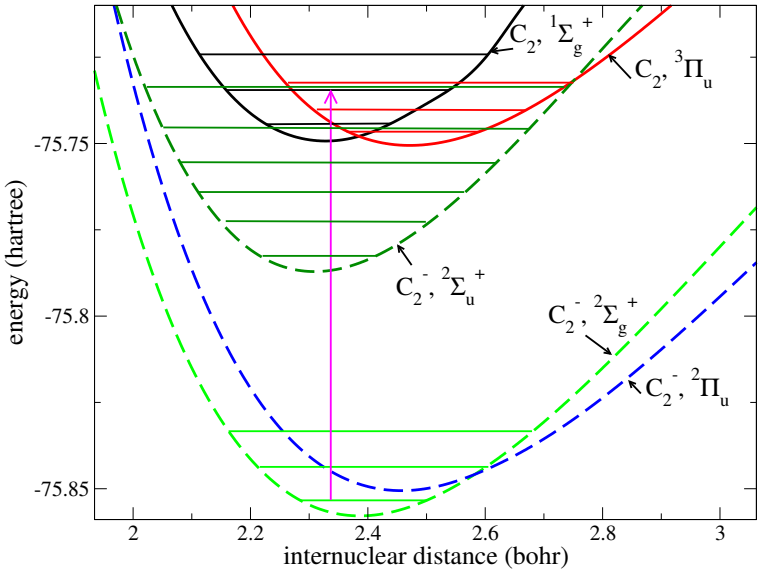

Figure 2.28: Potential energy curves of C_2 and C_2^- molecules was calculated using the `d-aug-pVQZ` atomic orbital basis set with *spd*-functions using the MRCI method.

In Ref. [138] by P.l. Jones et al. a very large PD cross section was observed if the laser is tuned to the $v' = 6$ vibrational level of the final electronic state of C_2^- (green curve in Fig. 2.28). This vibrational state $v' = 6$ is in resonance with $v'' = 1$ of the ground state of C_2 (black curve in Fig. 2.28). This is the reason why the PD cross section is enhanced. In fact, the electronic resonance in Fig. 2.27 corresponds to the excited state of C_2^- (green curve in Fig. 2.28). The C_2^- results are not complete and deserve a separate study.

CHAPTER 3: FORMATION OF ANIONS BY DISSOCIATIVE ELECTRON ATTACHMENT

The process, which could possibly explain formation of some molecular anions in the ISM, is dissociative electron attachment (DEA) [40]. DEA cross sections are needed to model plasma in many environments, including such technology applications as etching in semiconductor industry or chemical and gas lasers [139]. It is difficult to study the process both theoretically and in the experiment [140, 141].

In the DEA process, an incoming, low-energy electron attaches to a molecule which dissociates after [140]

$$e^- + \mathrm{AB} \rightarrow \mathrm{A}^- + \mathrm{B} \quad \text{or} \quad \mathrm{A} + \mathrm{B}^- \,. \tag{3.1}$$

In this process, an electron becomes temporarily trapped in a resonant state of the molecule. This resonance can autodetach again. Otherwise, it can dissociate, which happens only if the energetics allow it and the resonance has a lifetime long enough for dissociation to happen [140].

The literature on low-energy electron attachment to homonuclear diatomic halogens is extensive, if at times conflicted [142, 143, 144, 145, 146, 147, 148, 149]. These are the simplest systems that can undergo dissociative electron attachment at thermal energies, making them attractive targets for theoretical methods aimed at handling the complexities of electron-molecule interactions. They are also obvious subjects for experiment, and measurements of the attachment kinetics to homonuclear diatomic halogens extend back to the 1920s, the earliest days of any quantitative data on electron attachment rates [150, 151].

After theoretical and experimental studies of the DEA process [152, 153] performed for Cl_2 and F_2, interhalogens received little attention. In this chapter, results of theory-experiment collabora-

tion on DEA in ClF are presented. The experiment was performed by the group of Viggiano, who meassured rate coefficients for the DEA process in ClF [154]. The experiment was performed at temperatures from 300 - 900 K and at pressures of 1 - 2 Torr using a flowing afterglow - Langmuir probe apparatus. In this experiment, ClF attaches an electron inefficiently (k = 7.5 $\times$ 10^{-9} cm^3s^{-1}) at 300 K, with the rate coefficient rising to 1.5×10^{-8} cm^3s^{-1} at 700 K. At higher temperatures the apparent rate coefficient falls steeply.

In DEA theory, accurate determination of crossing point(s) between potential curves of the neutral molecule and the anion is crucial. For *ab initio* calculations it means that relative energy of the neutral and anion curves should be determined as accurately as possible. With this goal, the following procedure was tested and chosen in the present *ab initio* calculations. We use relatively large standard atomic basis sets augmented with diffuse functions with s, p, d, and f orbitals, `d-aug-cc-pVQZ` for fluorine and `aug-cc-pVQZ` for chlorine. Diffuse functions are necessary to accurately describe anion electronic states. With this basis, Hartree-Fock orbitals were determined for the neutral molecule. The same Hartree-Fock orbitals were used in the second step of the calculations for the neutral and anion molecule. In that second step, natural orbitals were determined for both molecules. To ensure accurate relative energy of the ClF and ClF^- curves, not only the same Hartree-Fock orbitals, but also the same orbital space was used in both the ClF and ClF^- calculations. In practice, a much larger compared to a standard single-molecule calculation was needed to obtain converged results for ClF^-. In a typical calculation, out of twenty two occupied orbitals in all symmetries, the eight lowest orbitals were kept frozen. For the neutral molecule, only the lowest $^1\Sigma^+$ electronic state was determined. For the anion, the $^2\Sigma^+$ and the $^2\Pi$ states were calculated. Using the natural orbitals, configuration interaction calculations were performed as the third step for the ground $^1\Sigma^+$ electronic state of ClF and for the two lowest states for each of the $^2\Sigma^+$ and $^2\Pi$ symmetries of ClF^-. Again, the same orbital space for ClF and ClF^- was used.

Potential energy curves of ClF and ClF^- molecules are shown in Fig. 3.1. On the right side of the

graph, labels "Cl+F", "Cl+F$^-$", and "Cl$^-$ +F" with short horizontal lines refer to the Cl+F, Cl+F$^-$, and Cl$^-$+F dissociation limits obtained in this thesis. The energies marked with the horizontal lines are those obtained at R = 7 bohrs, the largest distance where the convergence is still reasonable with the employed orbital space. The energy differences [Cl+F]-[Cl+F$^-$] and [Cl+F]-[F+Cl$^-$] correspond to electron affinities of Cl and F. In the present calculations [Cl+F]-[Cl+F$^-$] = 3.0 eV and [Cl+F]-[F+Cl$^-$] = 3.4 eV, whereas accurate affinities of F and Cl are 3.399 and 3.617 eV, respectively. Although the difference is significant, it does not affect the DEA calculations in the crossing region where accurate curves are necessary.

Each of the lowest curves of the $^2\Sigma^+$ and $^2\Pi$ states dissociates only towards the F + Cl$^-$ limit. Out of all the ClF$^-$ curves, only the lowest $^2\Sigma^+$ state crosses the neutral state near the minimum of the ClF potential. In addition, the ground state does not approach any other curve to the right of the crossing. This suggests that if the ClF molecule is initially in one of the lowest vibrational levels, the DEA products could only be F + Cl$^-$, which is consistent with the experimental results presented below. Figure 3.1 also shows the probability density $|\chi_v(R)|^2$ of the ground vibrational level in the ClF potential, representing the Franck-Condon factor for this state. Electron beam experiments are expected to show peaks corresponding to the higher-energy ClF$^-$ states shown in Fig. 3.1, but these are not relevant to the present thesis and would have to be calculated more accurately.

Table 3.1 below compares equilibrium positions R_e for ClF and ClF$^-$ obtained in the present work with several previous calculations [155, 156, 157, 158, 159] and an experimental work [160]. The values of R_e obtained in the thesis agree well with the most accurate previous theoretical work by Li et al. [158] and with the RKR data available from the experiment [160]. The electron scattering calculations were performed using the UK R-matrix code. In the calculation, the `cc-pVTZ` atomic basis with $l = 0 - 4$ orbitals were employed for the two atoms.

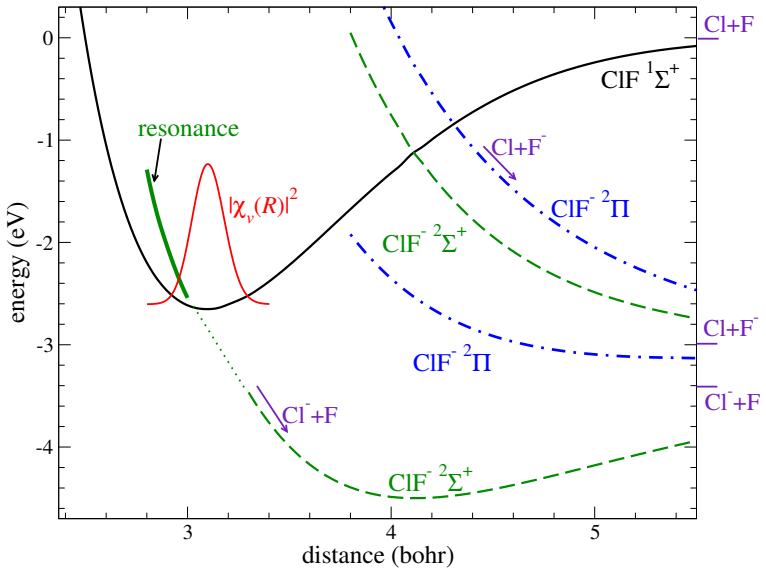

Figure 3.1: Potential energy curves of ClF and ClF^- molecules. The solid curve is the ground electronic state of the ClF molecule. The dashed green and dot-dashed blue curves correspond to the two lowest electronic states of the $^2\Sigma^+$ and $^2\Pi$ symmetries of ClF^-, respectively. The curve labeled $|\chi_v(R)|^2$ shows the probability density of the ground vibrational level of the ClF molecule. The thick line labeled resonance represents the energy of the lowest resonant state of ClF^-. The labels Cl+F, Cl+F^-, and Cl^-+F with short horizontal lines refer to corresponding dissociation limits as calculated in the thesis.

The target ClF molecule of the $^1\Sigma^+$ symmetry was represented using a complete-active-space configuration interaction (CASCI) method built on Hartree-Fock orbitals. Eight lowest Hartree-Fock orbitals of the target ClF were frozen in the CASCI calculations. The remaining ten (out of 26) electrons were distributed over the active space that included nine orbitals and six virtual orbitals. The virtual orbitals were included in the calculations to improve the electronic continuum states near the target nuclei. ClF is a small molecule and a small R-matrix sphere radius of 10 bohrs was used.

Table 3.1: Equilibrium distances R_e (in Å) of the ground electronic states of ClF and ClF^- obtained in the present thesis and previous study. The most accurate theoretical calculations are from Refs. ([157, 158])

	R_e(ClF)	R_e(ClF^-)
Present calculations	1.638	2.181
Calc., Ref. ([155])	1.614-1.668	2.049-3.036
Calc., Ref. ([156])	1.643-1.659	2.078-2.298
Calc., Ref. ([157])	1.641	
Calc., Ref. ([158])	1.6294	2.148-2.156
Calc., Ref. ([159])	1.63-1.69	2.25-2.40
Exp., Ref. ([160])	1.628	

The K-matrix $K(R)$ obtained in the scattering calculations was used to determine energies and widths of the $^2\Sigma^+$ resonance for distances R <3.05 bohrs, where the curve is resonant. The energies and widths were obtained from eigenphase sums generated by $K(R)$. The eigenphase sums for six values of R are shown in Fig. 3.2. As evident from Fig. 3.1, the $^2\Sigma^+$ curve of ClF^- crosses the ClF $^1\Sigma^+$ potential near R_c = 3.02 bohrs. The inset in Fig. 3.2 shows the resonance energy E and width Γ as a function of R. The full resonance width is obtained from fitting the eigenphase sums to the Breit-Wigner formula [161].

The resonance energy is also shown with the thick green line, but now the energy of the ClF $^1\Sigma^+$ potential is added to the scattering energy E. Represented in this way the resonant curve (thick green line in Fig. 3.1) should join smoothly the lowest $^2\Sigma^+$ curve of ClF^- obtained in bound-state calculations. However, our basis in the bound-state calculations was not optimized for weakly-bound states of $^2\Sigma^+$ curve of ClF^-. Therefore, a part of the $^2\Sigma^+$ curve below the crossing point is not converged and missing in Fig. 3.1. This part of the $^2\Sigma^+$ curve is replaced by a straight dotted line to guide the eye.

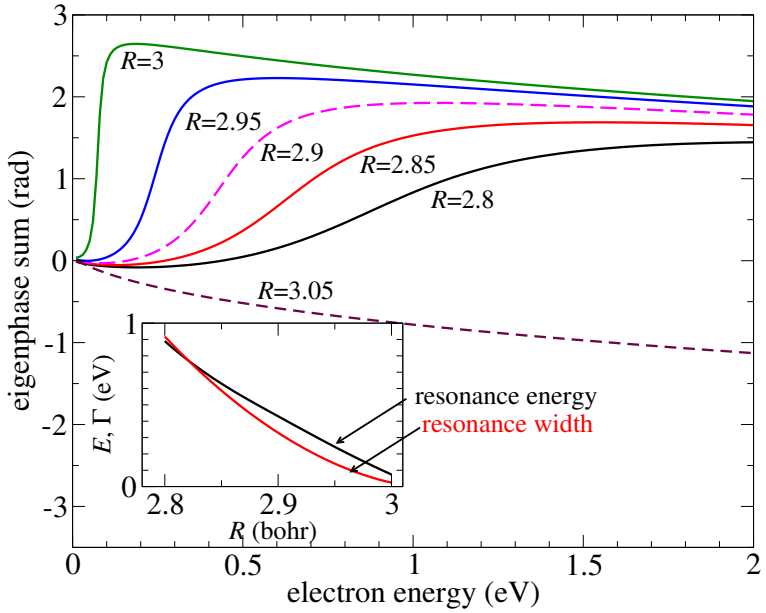

Figure 3.2: The eigenphase sums for e^-+ ClF scattering in the $^2\Sigma^+$ symmetry for six different values of the internuclear distance R near the crossing point of the ClF and ClF^- potential curves. For all shown values of R, the ClF^- state is resonant, except for R = 3.05 bohrs, for which the ClF^- electronic state is bound. The inset shows energies and widths of the resonant state. Energy E is the electron scattering energy.

Bound-state and scattering calculations show that the anion curve is crossing the neutral close to the equilibrium internuclear separation in ClF. The inversion symmetry is broken, and the s-wave component in the electron wave function contributes to the resonance composition. Our calculated scattering matrices indicate a substantial intermixture of the s, p and d waves.

As an example, for internuclear distance R = 3 bohrs and near-resonant energy of 0.07 eV (see Fig. 3.2), the probability of a partial-wave change after one collision from the $s\sigma$ partial wave to $p\sigma$ is 0.49. The probabilities of the $s\sigma \rightarrow d\sigma$ and $p\sigma \rightarrow d\sigma$ transitions at the same energy and internuclear distance are significantly smaller, 0.003 and 0.01 correspondingly.

Ab initio calculation of partial attachment amplitudes presents a big challenge for the nonlocal complex potential theory [162] where the amplitudes should be calculated as functions of electron

energies. But even in the local theory calculation of partial resonance widths is a nontrivial task, and, to the best of our knowledge, has been accomplished only in calculations of DEA to water [163] whose purpose was to extract information on the angular distribution of the DEA products.

In this part, I am presenting the cross section calculation process, which was done in collaboration with I. Fabrikant. An angular-independent attachment amplitude $V(R)$ can be calculated as

$$V(R) = (\Gamma(R)/2\pi)^{1/2}\,. \tag{3.2}$$

This is a common approach used in many local DEA calculations which we also use in the present thesis.

After $\Gamma(R)$ and the attachment amplitude $V(R)$ are obtained, we solve the inhomogeneous equation of the local complex potential model [164] (also called the boomerang model [165]) for the wave function $\Psi(R)$ describing the nuclear motion in the anion state

$$(T + U(R) - i\Gamma(R)/2 - E)\Psi(R) = -V(R)\chi_\nu(R)\,, \tag{3.3}$$

where T is the kinetic energy operator, $U(R)$ is the anion potential energy, E is the electron energy and $\chi_\nu(R)$ is the vibrational function of the molecule in the initial state.

The major deficiency of the local approximation appears in producing the DEA cross sections with incorrect threshold behavior. This is, for example, a serious issue in attachment to F_2 and Cl_2 molecules [166, 167]. Due to the Σ_u symmetry of the low-energy resonance in this case, the Wigner threshold law predicts $E^{1/2}$ energy dependence [143, 168] whereas in local calculations the cross section diverges towards $E = 0$ as E^{-1}. Bardsley [169] suggested a correction for the

attachment amplitude in the form of the factor

$$(E/E_r(R))^{a/2}\,, \tag{3.4}$$

where $E_r(R)$ is the resonance energy, that is $U(R) - U_0(R)$, where $U_0(R)$ is the potential energy of the neutral molecule, and a is the threshold exponent. For nonpolar molecules, according to the Wigner law, $a = l + 1/2$ where l is the lowest angular momentum allowed by symmetry. For polar molecules, depending on the dipole moment, a varies between 0 and $1/2$ [170]. In particular for the ClF molecule whose dipole moment is 0.346 a.u.(0.8881 D) [171], $a = 0.4152$. The cross section for an exothermic reaction behaves as E^{a-1} that in the case of ClF leads to $E^{-0.5848}$ behavior at low energies, in contrast to the $1/E$ behavior in the original version of the nonlocal theory. This difference is important for thermal energies.

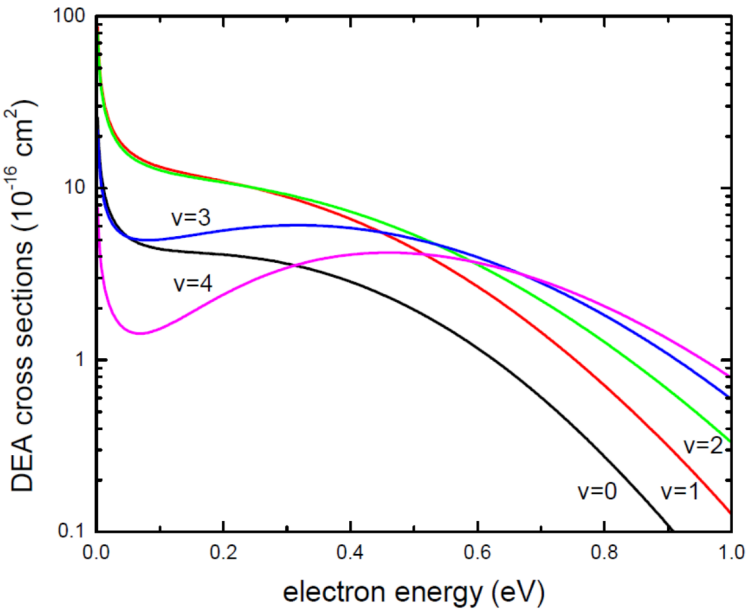

Figure 3.3: Dissociative electron attachment cross sections as a function of electron energy, calculated with Bardsley's correction, from the first five vibrational states of the ClF.

Figure 3.3 presents the attachment cross sections for different initial vibrational states. At low electron energies the attachment cross section is largest for $v = 1$ and 2; about 3-4 times those for $v = 0$ and 3 at low-energy. The vibrational quantum for ClF is 97.1 meV. Therefore, accounting for the Boltzmann factor, the $v = 3$ contribution is insignificant at $T = 700$ K. This dependence of the DEA cross section on v is relatively weak; that is typical for the situation when the neutral and anion curves cross close to the equilibrium internuclear separation. This results in a weak dependence of the cross section on the vibrational temperature, as demonstrated in Fig. 3.4.

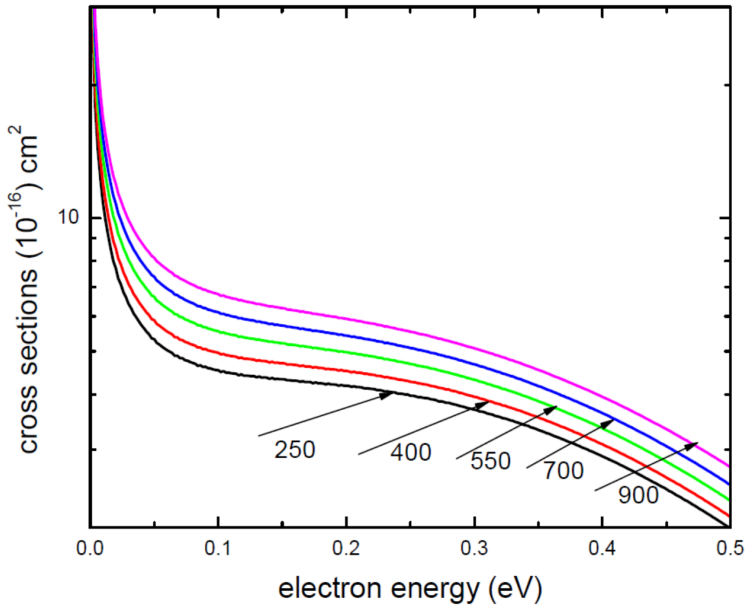

Figure 3.4: DEA cross sections for ClF averaged over the vibrational state distribution. Numbers associated with each curve indicate the vibrational temperature in K.

Comparison with Experiment

The theoretical calculations described above confirm the exclusive production of Cl^- from ClF. The theoretical rate coefficients were obtained by averaging the cross sections from Fig. 3.4 over the

electron energy distribution. The results do not show a significant temperature dependence because the low-energy behavior of the cross section is close to $E^{1/2}$ meaning that the rate coefficient weakly depends on E. The growth of the ClF rate coefficient with temperature is slow and does not indicate any activation energy typical for Arrhenius-type behavior [172]. In Fig. 3.5 we show good agreement of experimental data with the second calculation at T = 300 K. However, the rate coefficients calculated with Bardsley's correction [169] grow slower than the experimental values. It is not unusual for Bardsley's correction to underestimate the DEA cross section, therefore it is not surprising that at T = 700 K the experimental result lies closer to the first calculation. Overall, considering all approximations involved in the theory, the agreement is satisfactory.

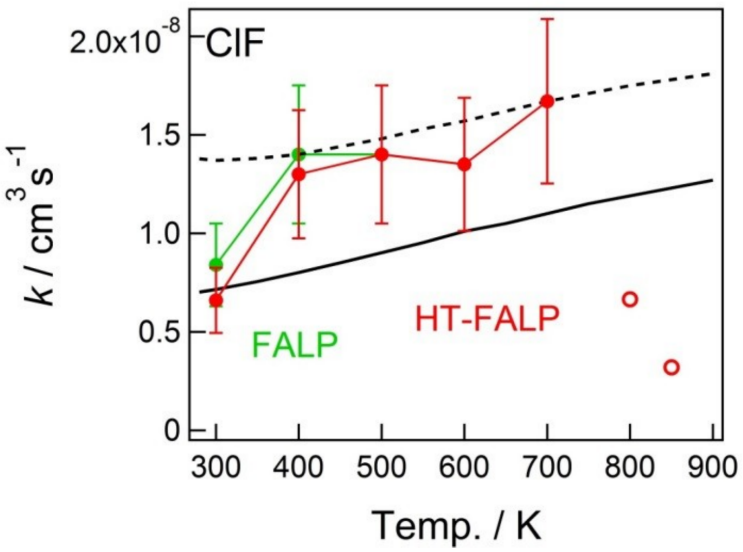

Figure 3.5: Experimental DEA rate coefficients k_a (in units of $\mathrm{cm^3 s^{-1}}$) for ClF from 300 to 850 K. Points connected by line segments are from the FALP apparatus (green line) and from the HT-FALP apparatus (red line). Two open symbols represent the apparent rate coefficient which may be low due to decomposition or other losses in the flow tube. The rate coefficient from electron scattering calculations is shown with (black solid line) and without (black dashed line) Bardsley's correction, as described in the text.

The electron attachment results for ClF is presented in Table 3.2 and Fig. 3.5. The apparent rate coefficient for attachment to ClF falls off steeply above 700 K. Such a steep drop cannot be

physical, and is typical of high temperature decomposition of the reactant on walls of the quartz inlet line which is overheated by 10 - 20 % in the upstream region.

Table 3.2: Attachment rate coefficients k_a (in units of cm^3s^{-1}) for ClF from 300 to 700 K. FALP and HT-FALP values were averaged for data taken at the same temperatures on both instruments. Error bars for the measurements are approximately ± 25 %.

Temperature	300	400	500	600	700
Attachment rate coefficients	7.5×10^{-9}	1.4×10^{-8}	1.4×10^{-8}	1.4×10^{-8}	1.7×10^{-8}

ClF dissociatively attaches exclusively forming Cl^-, forming little or no F^-, throughout the entire temperature range. The Cl^- channel is more exothermic than forming F^- from ClF by only 0.21 eV. The theoretical calculations described above imply exclusive production of Cl^- from ClF.

In this chapter, electron attachment to the interhalogen diatomic ClF was studied over the temperature range 300 - 900 K using two flowing afterglow-Langmuir probe apparatuses. ClF exhibits modestly increasing rate coefficient with increasing temperature, predominantly forming Cl^-. The ClF trend may be slightly steeper than that predicted from theoretical calculations, but the calculated rate coefficients are nevertheless in agreement with experiment. No activation barrier to attachment is indicated by the modest trends with temperature. Dissociative electron attachment to ClF occurs near the equilibrium Cl-F atomic separation. The lack of inversion symmetry in ClF allows a substantial contribution of the s-wave component of the electron wave function to the scattering cross section. Theory shows that the v = 1 and 2 vibrational levels of ClF dominate the attachment resonance with little contribution from higher modes or v = 0.

CHAPTER 4: RO-VIBRATIONAL EXCITATION OF MOLECULE

Rotational Excitation of Acetylene in Collision with Electrons

Acetylene, HCCH, is one of the most studied polyatomic molecules [173]. It was detected in many environments, such as, the interstellar medium [174] and the planetary atmospheres, including Jupiter [175], Saturn [176], Neptune [177], and Uranus [178]. Electron collisions play an important role in the chemistry of acetylene plasmas [179]. In the ground electronic state, HCCH is linear with $D_{\infty h}$ symmetry [180]. Cross sections for various processes involving e - HCCH collisions are important for understanding different phenomena, such as thermal diffusion in polyatomic gases [181], resonance fluorescence [182], relaxation of nuclear spin-lattice [183], and ultrasonic dispersion [184]. Others include cooling in both interstellar space [185] and in nozzle flow [186].

In this chapter, a theoretical approach to evaluate cross sections for rotational excitation of linear neutral molecules by an electron impact is developed and applied to acetylene. The calculations were made using the MOLPRO [98] and UK R-matrix (Quantemol) [59, 86, 87] suites of programs.

Theory

Derivation of the Formula for Rotational Excitation Cross Section

The cross section for the transition in which the rotational quantum number changes from j to $j^{'}$ was derived in the present thesis as follow. To derive the cross section formula for rotational excitation, first, we write the spherical harmonic describing the incident electron in a e - HCCH

collision as below

$$Y_{lm_l}(\tilde{\theta},\tilde{\phi}) = \sum_{\lambda=-l}^{l} [D^{l}_{m_l\lambda}(\Omega)]^{*} Y_{l\lambda}(\theta,\phi)\,, \tag{4.1}$$

where λ is the projection of the electron angular momentum on the molecular axis, $(\tilde{\theta},\tilde{\phi})$ and (θ,ϕ) are spherical angles of the incident electron defined with respect to a fixed laboratory axis and the molecular axis, respectively. In the laboratory frame (LF), we have

$$|j\ m_j\ \mu > Y_{lm_l}(\tilde{\theta},\tilde{\phi}) \equiv |a>\,, \tag{4.2}$$

where $|a>$ is a channel function describing the incident electron in LF and the state of the target HCCH with the quantum numbers $|j\ m_j\ \mu\ l\ m_l>$, and $|j\ m_j\ \mu>$ can be written in terms of the Wigner function as follow

$$|j\ m_j\ \mu >= \sqrt{\frac{2j+1}{8\pi^2}} [D^{j}_{m_j\mu}(\Omega)]^{*}\,, \tag{4.3}$$

where j , m_j , and μ are the angular momentum of HCCH and its projections in the laboratory frame and the molecular frame correspondingly, and $D^{j}_{m_j\mu}$ is the Wigner function depending on three Euler angles Ω. Using equations above we have

$$|a >= \sqrt{\frac{2j+1}{8\pi^2}} \sum_{\lambda} [D^{l}_{m_l\lambda}(\Omega)]^{*} [D^{j}_{m_j\mu}(\Omega)]^{*} Y_{l\lambda}(\theta,\phi)\,. \tag{4.4}$$

By using Eq. (A8) from Ref. [5]:

$$D^{j}_{m_j\mu}(\Omega) D^{l}_{m_l\lambda}(\Omega) = \sum_{J',M,\Lambda}^{j+l} D^{J'}_{M\Lambda}(\Omega) C^{J'M}_{jm_jlm_l} C^{J\Lambda}_{j\mu l\lambda}\,, \tag{4.5}$$

where $C^{J\Lambda}_{j\mu l\lambda}$ are Clebsch-Gordan coefficients, we can rewrite the formula (4.4), at fixed J and M, as the following term, where $\Lambda = \mu + \lambda$, with total angular momentum $J = l + j$ and projection

$M = m_l + m_j$ in the LF

$$|a >= \sqrt{\frac{2j+1}{8\pi^2}} \sum_{\lambda} \sum_{JM\Lambda} [D^J_{M\Lambda}(\Omega)]^* C^{JM}_{jm_j lm_l} C^{J\Lambda}_{j\mu l\lambda} Y_{l\lambda}(\theta, \phi)\,. \tag{4.6}$$

$|b >$ is a channel function describing the final state defined by the quantum numbers $|J\ M\ \Lambda;\ l\ \lambda\ j >$

$$|b >= \sqrt{\frac{2J+1}{8\pi^2}} [D^J_{M\Lambda}(\Omega)]^* Y_{l\lambda}(\theta, \phi)\,, \tag{4.7}$$

where $|a >$ can be written in terms of $|b >$

$$|a >= \sum_{\lambda JM\Lambda} \sqrt{\frac{2j+1}{2J+1}} C^{JM}_{jm_j lm_l} C^{J\Lambda}_{j\mu l\lambda} |b >\ . \tag{4.8}$$

Then we have

$$< b|a >= \sqrt{\frac{2j+1}{2J+1}} C^{JM}_{jm_j lm_l} C^{J\Lambda}_{j\mu l\lambda}\,, \tag{4.9}$$

$$< a|\bar{b} >= \sqrt{\frac{2j+1}{2J+1}} C^{J\bar{M}}_{jm_j lm_l} C^{J\bar{\Lambda}}_{j\mu l\bar{\lambda}}\,, \tag{4.10}$$

$$< \bar{b'}|a' >= \sqrt{\frac{2j'+1}{2J'+1}} C^{J'\bar{M}'}_{j'm'_j l'm'_l} C^{J'\bar{\Lambda}'}_{j'\mu' l'\bar{\lambda}'}\,, \tag{4.11}$$

$$< a'|b' >= \sqrt{\frac{2j'+1}{2J'+1}} C^{J'M'}_{j'm'_j l'm'_l} C^{J'\Lambda'}_{j'\mu' l'\bar{\lambda}'}\,. \tag{4.12}$$

In order to calculate rotational excitation cross section from initial j to final j' we have

$$\sigma_{j'\leftarrow j} = \frac{\pi}{k_j^2} \frac{1}{2j+1} \sum_{m_j m'_j} \sum_{ll'm'_l} (2l+1) |T_{l'm'_l j'm'_j \leftarrow l0jm_j}|^2\,, \tag{4.13}$$

where k_j are the incoming wave vectors and $T_{l'm'_l j'm'_j \leftarrow l0jm_j}$ are T-matrix elements.

We define $T_{a'a}$ and $T^*_{aa'}$ as follow

$$|T_{a'a}|^2 = T^*_{aa'} T_{a'a}\,, \tag{4.14}$$

$$T_{a'a} = \sum_{bb'} < a'|b' >< b'|T|b >< b|a >\,, \tag{4.15}$$

$$T^*_{aa'} = \sum_{\bar{b}\bar{b}'} < a|\bar{b} >< \bar{b}|T^*|\bar{b}' >< \bar{b}'|a' >\,, \tag{4.16}$$

where the elements of T-matrix are given by

$$\begin{aligned} < b'|T|b >= \sqrt{\frac{2J'+1}{8\pi^2}}\sqrt{\frac{2J+1}{8\pi^2}} \int \sin\beta d\alpha d\beta d\gamma D^{J'}_{M'\Lambda'}(\Omega)[D^J_{M\Lambda}(\Omega)]^* < l'\lambda'|T|l\lambda > \\ = \delta_{JJ'}\delta_{MM'}\delta_{\Lambda\Lambda'} T_{l'\lambda';l\lambda}\,, \end{aligned} \tag{4.17}$$

$$< \bar{b}|T^*|\bar{b}' >= \delta_{JJ'}\delta_{\bar{M}\bar{M}'}\delta_{\bar{\Lambda}\bar{\Lambda}'} T^*_{l'\bar{\lambda};l\bar{\lambda}'}\,. \tag{4.18}$$

Using equations (4.14), (4.15), and (4.16) we have

$$\begin{aligned} |T_{a'a}|^2 &= \sum_{bb'}\sum_{\bar{b}\bar{b}'} < a|\bar{b} >< \bar{b}|T^*|\bar{b}' >< \bar{b}'|a' >< a'|b' >< b'|T|b >< b|a > \\ &= \sum_{JJ';JJ'} \sum_{MM'\Lambda\Lambda'\bar{\Lambda}\bar{\Lambda}'} \sum_{ll'm'_l} \sum_{\lambda\lambda';\bar{\lambda}\bar{\lambda}'} \frac{(2j+1)(2j'+1)}{[(2J+1)(2J'+1)(2J+1)(2J'+1)]^{\frac{1}{2}}} \\ &\quad \times C^{J\bar{M}}_{jm_j lm_l} C^{J\bar{\Lambda}}_{j\mu l\bar{\lambda}} C^{J'\bar{M}'}_{j'm'_j l'm'_l} C^{J'\bar{\Lambda}'}_{j'\mu' l'\bar{\lambda}'} C^{J'M'}_{j'm'_j l'm'_l} C^{J'\Lambda'}_{j'\mu' l'\lambda'} C^{JM}_{jm_j lm_l} C^{J\Lambda}_{j\mu l\lambda} \\ &\quad \times \delta_{JJ'}\delta_{MM'}\delta_{\Lambda\Lambda'}\delta_{JJ'}\delta_{\bar{M}\bar{M}'}\delta_{\bar{\Lambda}\bar{\Lambda}'} T_{l'\lambda';l\lambda} T^*_{l'\bar{\lambda};l\bar{\lambda}'}\,. \end{aligned} \tag{4.19}$$

Then Eq. (4.13) can be written as

$$\sigma_{j'\leftarrow j} = \sum_{JJM}\sum_{\Lambda\bar{\Lambda}}\sum_{ll'}\sum_{\lambda\lambda';\bar{\lambda}\bar{\lambda}'}\sum_{m_j m'_j m'_l}\frac{\pi}{k_j^2}\frac{(2j'+1)(2l+1)}{(2J+1)^2}$$
$$\times C^{J\bar{M}}_{jm_j lm_l}C^{J\bar{\Lambda}}_{j\mu l\bar{\lambda}}C^{J\bar{M}}_{j'm'_j l'm'_l}C^{J\bar{\Lambda}}_{j'\mu' l'\bar{\lambda}'}C^{JM}_{j'm'_j l'm'_l}C^{J\Lambda}_{j'\mu' l'\lambda'}C^{JM}_{jm_j lm_l}C^{J\Lambda}_{j\mu l\lambda}T_{l'\lambda';l\lambda}T^*_{l'\bar{\lambda};l\bar{\lambda}'}\,. \tag{4.20}$$

From the orthonormality of Clebsch-Gordan coefficients we have

$$\sum_{m_j m_l} C^{J\prime M\prime}_{jm_j lm_l}C^{JM}_{jm_j lm_l} = \delta_{J'J}\delta_{M'M}\,, \tag{4.21}$$

$$\sum_{m'_j m'_l} C^{J\bar{M}}_{j'm'_j l'm'_l}C^{J\Lambda}_{j'm'_j l'm'_l} = \delta_{JJ}\delta_{\bar{M}M}\,. \tag{4.22}$$

Then Eq. (4.20) simply becomes

$$\sigma_{j'\leftarrow j} = \sum_{JM}\sum_{\Lambda\bar{\Lambda}}\sum_{ll'}\sum_{\lambda\lambda';\bar{\lambda}\bar{\lambda}'}\sum_{m_j}\frac{\pi}{k_j^2}\frac{(2j'+1)(2l+1)}{(2J+1)^2}$$
$$\times C^{JM}_{jm_j lm_l}C^{J\bar{\Lambda}}_{j\mu l\bar{\lambda}}C^{J\bar{\Lambda}}_{j'\mu' l'\bar{\lambda}'}C^{J\Lambda}_{j'\mu' l'\lambda'}C^{JM}_{jm_j lm_l}C^{J\Lambda}_{j\mu l\lambda}T_{l'\lambda';l\lambda}T^*_{l'\bar{\lambda};l\bar{\lambda}'}\,. \tag{4.23}$$

Using Eq. (5) of Sec. 8.7.2 from Ref. [187]

$$\sum_{\alpha\gamma} C^{c\gamma}_{a\alpha b\beta}C^{c\gamma}_{a\alpha b'\beta'} = \frac{\Pi_c^2}{\Pi_b^2}\delta_{bb'}\delta_{\beta\beta'}\,, \tag{4.24}$$

where $\Pi_{ab\ldots c} = \sqrt{(2a+1)(2b+1)\ldots(2c+1)}$. Therefore we have

$$\sum_{m_j M} C^{JM}_{jm_j lm_l}C^{JM}_{jm_j lm_l} = \frac{2J+1}{2l+1}\,. \tag{4.25}$$

Therefore, the cross section for the rotational excitation is

$$\sigma_{j'\leftarrow j} = \frac{\pi(2j'+1)}{k_j^2} \sum_{J\Lambda\bar{\Lambda};ll'\lambda\lambda'} \frac{1}{(2J+1)} C^{J\bar{\Lambda}}_{j\mu l\bar{\lambda}} C^{J\bar{\Lambda}}_{j'\mu' l'\bar{\lambda}'} C^{J\Lambda}_{j'\mu' l'\lambda'} C^{J\Lambda}_{j\mu l\lambda} T_{l'\lambda';l\lambda} T^{*}_{l'\bar{\lambda};l\bar{\lambda}'} \,. \tag{4.26}$$

where $\mu = \mu' = 0$ for HCCH in the ground electronic state.

Eigenphases

Eigenphases of various doublet scattering states for $e-$HCCH scattering were calculated using the UK R-matrix code. Figure 4.1 shows the eigenphases of $e-$HCCH scattering as a function of energy. The calculations were made up to 9 eV obtained for various doublet scattering states, such as ^{2}Ag , ^{2}Au, $^2B_{1g}$, $^2B_{1u}$, $^2B_{2g}$, $^2B_{2u}$, $^2B_{3g}$, and $^2B_{3u}$, which are denoted by electron terms $^2\sum^+_g$, $^2\sum^-_u$, $^2\sum^-_g$, $^2\sum^+_u$, $^2\Pi_g$, $^2\Pi_u$, $^2\Pi_g$, and $^2\Pi_u$, respectively. Because $^2B_{2u}$ and $^2B_{3u}$ and also $^2B_{2g}$ and $^2B_{3g}$ are degenerate states, therefore one curve is shown, $^2\Pi_u$ and $^2\Pi_g$, respectively.

Calculations with different sets of parameters were performed in order to evaluate the uncertainty of the obtained results. The following parameters were independently varied: (1) the Gaussian basis set, namely, the `DZP` and `cc-PV`x`Z` bases with x =`D,T,Q`; (2) the number of target states employed in close coupling expansion was varied from 7 to 66; (3) the number of active and (4) virtual states has also been varied; (5) the R-matrix sphere radius was varied in the interval of 10-15 bohrs.

The final calculation was made with the following parameters: We used the atomic orbital basis set `cc-PVQZ`. Three lowest Hartree-Fock orbitals of the target HCCH molecule were frozen in the CASCI calculations. The remaining eight (out of 14) electrons were distributed over the active space that included nine orbitals and six virtual orbitals. The virtual orbitals were included in the calculations to improve the electronic continuum states near the target nuclei. The R-matrix sphere

radius of 12 bohr and the geometry of equilibrium of HCCH [188] were used.

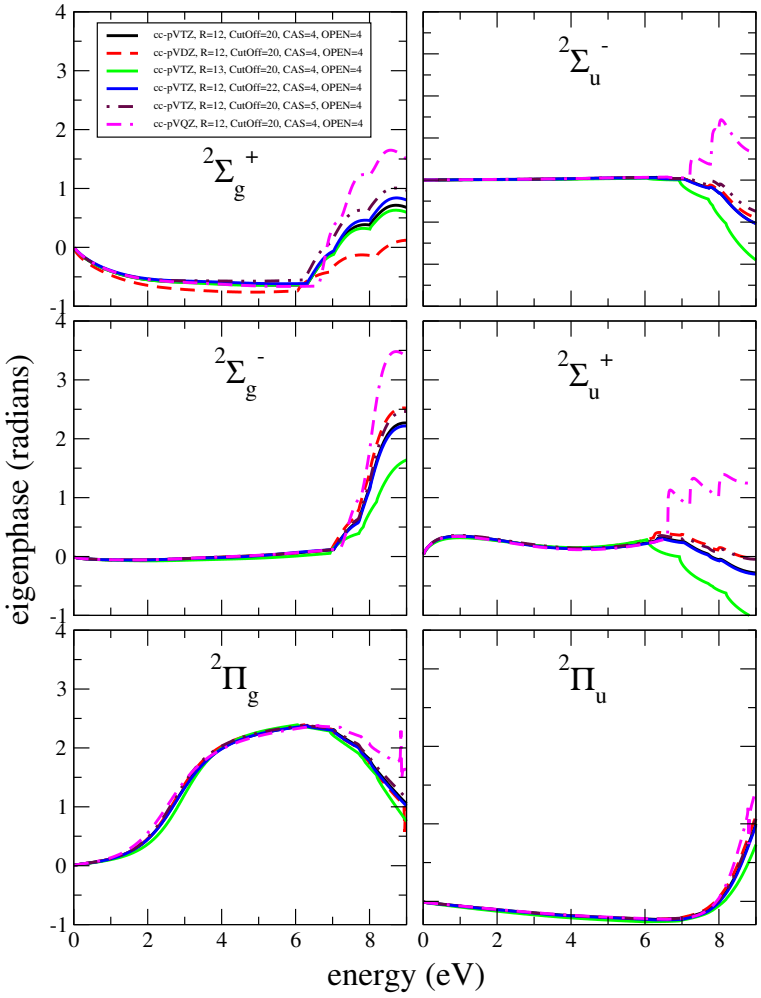

Figure 4.1: Eigenphases for $e-$HCCH scattering with different sets of parameters for various doublet scattering states.

Differential Cross Section

In this section, the differential cross sections (DCS) calculated for $e-$HCCH scattering using the UK R-matrix code were discussed. Figure 4.2 shows differential cross section for $e-$HCCH scattering over a range of incident energy from 0.1 eV to 10.0 eV for different transitions $j = 0 \rightarrow 0$,

2, 4 with the solid, dashed, dashed-dotted lines, respectively.

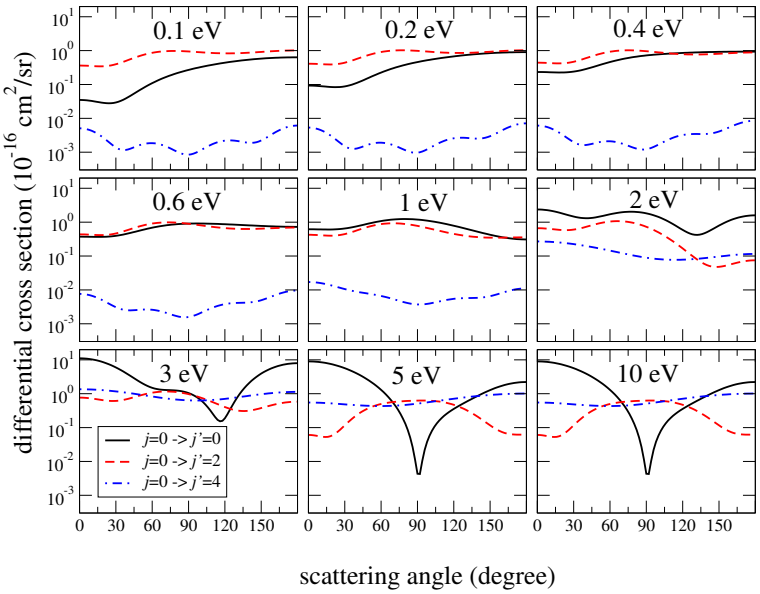

Figure 4.2: Differential cross sections for $e-$HCCH scattering is calculated for energies between 0.1 eV and 10.0 eV. The differential cross sections shown with the solid, dashed, and dashed-dotted lines present for transitions $j = 0 \rightarrow 0$, 2, 4, respectively.

The comparison of the differential cross sections obtained theoretically with previous calculation allows us to validite the obtained results. Figure 4.3 compares the differential cross sections for $e-$HCCH scattering with the previous work [189] at energy 10 eV for different transitions $j = 0 \rightarrow 0$, 2, 4. The solid and dashed lines show the present and previous results, respectively.

Momentum Transfer Cross Section

In this section, I am presenting the obtained momentum transfer cross section (MTCS) for $e-$HCCH scattering using the UK R-matrix code. Figure 4.4, the panel below, shows the obtained momentum transfer cross section for $e-$HCCH scattering for different basis sets. The solid, dashed, dashed-dotted lines show MTCS at bases `cc-pVTZ`, `cc-pVDZ` and `cc-pVQZ`, respectively. In the same

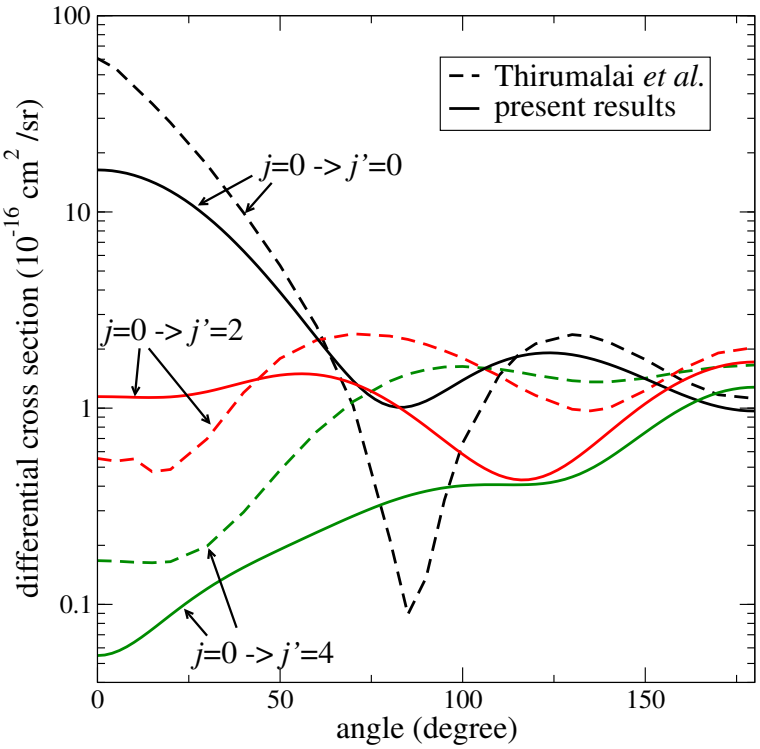

Figure 4.3: Comparison of differential cross sectionsfor $e-$HCCH scattering with the previous work [189] at energy 10 eV for different transitions $j = 0 \rightarrow 0, 2, 4$. The solid and dashed lines show the present and previous results, respectively.

figure, the panel above, compares the obtained momentum transfer cross section with the experimental and previously theoretical results [173, 133, 190, 191]. The dashed line shows the present work. There is almost a good agreement between the present and experimental results at energies between 1 eV and 2 eV.

In this chapter, a theoretical approach to evaluate cross sections for rotational excitation of linear neutral molecules by an electron impact was developed and applied to acetylene, HCCH. The differential cross sections for e-HCCH scattering were calculated for energies between 0.1 eV and 10 eV, and for transitions $j = 0 \rightarrow 0, 2, 4$. The momentum transfer cross section and eigenphases for e-HCCH scattering were also calculated and compared with the previous works.

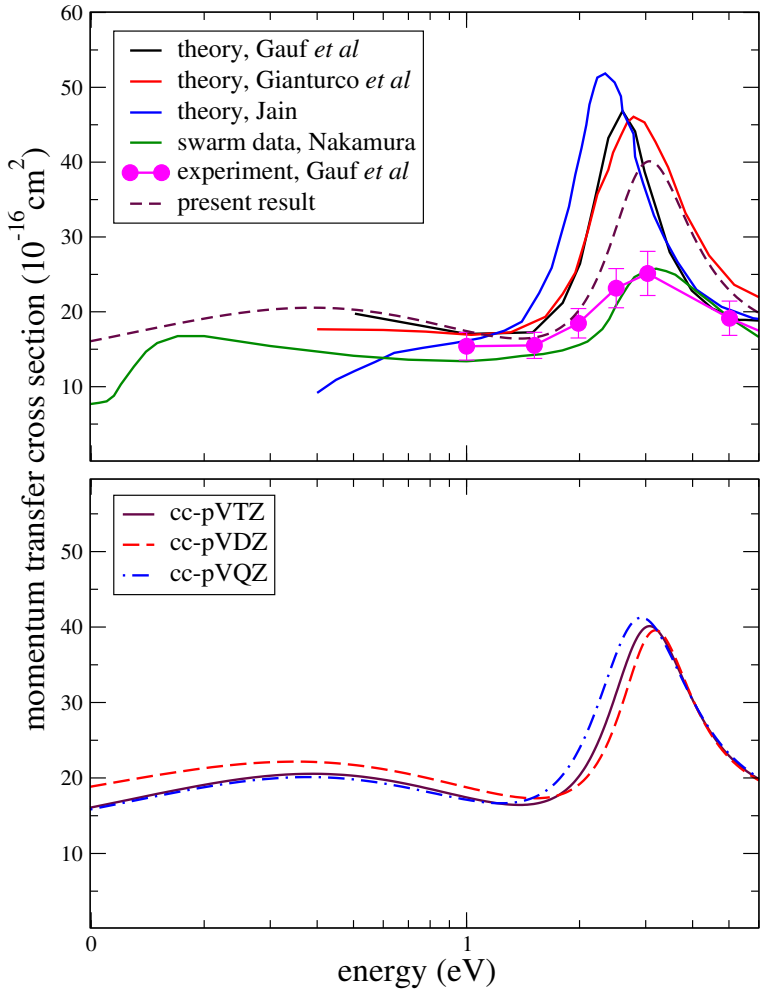

Figure 4.4: Comparison of momentum transfer cross section for $e-$HCCH scattering with the previous works. The dashed line on the graph above shows the present work.

CHAPTER 5: CONCLUSION

In this thesis, we have studied the process of radiative attachment to the C_nH ($n = 2, 4, 6, 8$), C_nN ($n = 1, 3, 5$), and C_2 molecules as well as the photodetachment of their anionic species. REA cross sections were calculated using Eq. (2.13) and discussed in chapter 2. Transitions dipole moments needed in cross section calculations were computed using a new implementation of the UK R-matrix [86, 87, 192]. Cross sections for the inverse process, electron photodetachment from the negative molecular ion were also calculated using the same transition dipole moments. Structure calculations are an essential part of the present thesis. They were performed using the MOLPRO [98] and UK R-matrix (Quantemol) suites of programs.

Photodetachment cross sections were used to obtain the corresponding thermally-averaged rate coefficients. The obtained REA rate coefficients evaluated at temperature 30 K are 7×10^{-16} cm^3/s for CN^-, 7×10^{-17} cm^3/s for C_2H^-, and 2×10^{-16} cm^3/s for C_4H^- [66]. At temperature 300 K, the rate coefficients are 2.5 $\times10^{-15}$ cm^3/s, 1.4 $\times10^{-15}$ cm^3/s, 4.5 $\times10^{-15}$ cm^3/s, and 4.8 $\times10^{-15}$ cm^3/s for C_2H^-, C_4H^-, C_6H^-, and C_8H^- respectively. The rate coefficients at 300 K are also calculated for CN^-, C_3N^-, and C_5N^-, which are 1.0 $\times10^{-15}$ cm^3/s, 4.7 $\times10^{-15}$ cm^3/s, and 7.5 $\times10^{-15}$ cm^3/s respectively. The coefficients depend weakly on temperature between 10 K and 100 K and increase relatively quickly with temperature above 200 K. The validity of the obtained results is verified by comparing the present theoretical results with experimental data from recent photodetachment experiments [5]. Values of rate coefficients calculated in this thesis increase with the size of molecules. This could be explained by a classical consideration that a larger size of a molecule means, in general, a larger TDM with the rate coefficient being proportional to the TDM squared.

Table 5.1 below compares the radiative attachment rate coefficients for molecules CN^-, C_2H^-, C_3N^-, C_4H^-, C_5N^-, C_6H^-, and C_8H^- at 300 K obtained in the present thesis with the rate coefficient that would be needed to explain the observed abundance of anions assuming that the anions are formed by REA in the ISM and previous theoretical calculation performed using the phase space theory respectively. Because the theoretical REA rate coefficients validated by the PD experiments disagree by several orders of magnitude with the values needed to explain the observed abundance of anions in the ISM, the formation mechanism of observed anions must be different than REA. The obtained REA cross sections are too small to explain formation of the molecular anions described above by the REA process in the ISM: If one assumes that CN^-, C_3N^-, and C_5N^- are formed by REA from the corresponding neutral molecules, the REA cross sections should be much larger, by more than five orders of magnitude than the values obtained in this study.

Table 5.1: Radiative attachment rate coefficients at 300 K

	Present (cm^3/s)	Coefficient needed to explain the observed abundance (cm^3/s)	Phase-space theory (cm^3/s)
CN/CN^-	1.0×10^{-15}	Large	2.0×10^{-15}
C_3N/C_3N^-	4.7×10^{-15}	2.0×10^{-9}	$(2\text{-}4)\times10^{-10}$
C_5N/C_5N^-	7.5×10^{-15}	$\sim 2.0\times10^{-7}$	2.0×10^{-7},1.25×10^{-7}
C_2H/C_2H^-	2.5×10^{-16}	$<1.5\times10^{-11}$	2.0×10^{-15}
C_4H/C_4H^-	1.4×10^{-15}	9×10^{-11}	1.1×10^{-8}
C_6H/C_6H^-	4.5×10^{-15}	1.4×10^{-8}	6.2×10^{-8}
C_8H/C_8H^-	$\sim 4.8\times10^{-15}$	2.5×10^{-8}	6.2×10^{-8}

Dissociative electron attachment (DEA) cross sections and rate coefficients for the ClF molecule were computed. Calculations confirm the exclusive production of Cl^- from ClF. The calculated rate coefficients are in good agreement with the experiment at 300 K. The results do not show a significant temperature dependence because the low-energy behavior of the cross section is close to $E^{-1/2}$ meaning that the rate coefficient weakly depends on E.

As mentioned above, indirect REA mechanism via rotational resonances in low-energy continuum spectra of electron-target collisions might increase the rate coefficients, but it is unlikely that the increase could be as large as five or more orders of magnitude [5, 193]. One possibility in the process of REA, which was not considered using a quantum-mechanical approach, is the role of weakly-bound dipole states of molecules with a large dipole moment, such as C_3N or C_5N, which according to recent studies [194, 195, 193] might enhance the REA cross section. On the other hand, it has been suggested that some of the anions observed in space could be formed due to their large dipole moment, which could provide a *doorway* to attach to the radical. Therefore, for the completeness of the theoretical approach, the role of dipole states in the REA process should still be considered.

Dipole bound states (DBS) of anions, which are electronic states close to the detachment threshold were predicted to exist for neutral molecules with a dipole moment larger than about 2-2.5 D [196, 197]. The rovibrational states below the threshold are bound states, but more excited rotational DBS levels situated above the threshold can autodetach. These states can be rovibrational Feshbach states that can also be reached in electron-molecule collisions by electron capture, which should provide a longer timescale for the electron to remain around the molecule before it is captured into an available unoccupied molecular orbital [198]. In the ISM, the existence of long-lived DBSs could increase the attachment rate, and subsequently increasing the abundance of anions [197]. DBSs could play a fundamental role as intermediate states in the attachment of electrons to neutrals. In Ref. [199] similar mechanism was studied in dissociative electron attachment experi-

ments, and also it was discussed as *doorway* for attachment into valence states of anions [196]. If this process is unlikely to occur for C_2H due to its relatively small dipole moment, this possibility can not be discarded for larger radicals such as C_4H or C_6H and should be the subject of future efforts. The study of the role of the dipole/rotational resonances is under way.

At the end, a theoretical approach to evaluate cross sections for rotational excitation of linear neutral molecules by an electron impact was developed and applied to acetylene, HCCH. The differential cross sections for e-HCCH scattering were calculated for energies between 0.1 eV and 10.0 eV. The momentum transfer cross section and eigenphases were also calculated.

LIST OF REFERENCES

[1] T. Best, R. Otto, S. Trippel, P. Hlavenka, A. von Zastrow, S. Eisenbach, S. Jezouin, R. Wester, E. Vigren, M. Hamberg, and W. D. Geppert. Absolute photodetachment cross-section measurements for hydrocarbon chain anions. *Astrophys. J.*, 742:63, 2011.

[2] S. Kumar, D. Hauser, R. Jindra, T. Best, Š. Roučka, W.D. Geppert, T. J. Millar, and R. Wester. Photodetachment as a destruction mechanism for CN^- and C_3N^- anions in circumstellar envelopes. *Astrophys. J.*, 776:25, 2013.

[3] P. Yzombard, M. Hamamda, S. Gerber, M. Doser, and D. Comparat. Laser cooling of molecular anions. *Phys. Rev. Lett.*, 114:213001, 2015.

[4] D. B. Dao and R. Mabbs. The effect of the dipole bound state on AgF^- vibrationally resolved photodetachment cross sections and photoelectron angular distributions. *J. Chem. Phys.*, 141:154304, 2014.

[5] N. Douguet, S. Fonseca dos Santos, M. Raoult, O. Dulieu, A.E. Orel, and V. Kokoouline. Theory of radiative electron attachment to molecules: Benchmark study of CN^-. *Phys. Rev. A*, 88:052710, 2013.

[6] M. Ayouz, R. Lopes, M. Raoult, O. Dulieu, and V. Kokoouline. Formation of H_3^- by radiative association of H_2 and H^- in the interstellar medium. *Phys. Rev. A*, 83:052712, 2011.

[7] M. Hamamda, P. Pillet, H. Lignier, and D. Comparat. Universal deceleration of highly polar molecules. *New J. Phys.*, 17:045018, 2015.

[8] W. D. Watson. Interstellar molecule reactions. *Rev. Mod. Phys.*, 48:513, 1976.

[9] D. L. Huestis, S. W. Bougher, J. L. Fox, M. Galand, R. E. Johnson, J. I. Moses, and J. C. Pickering. Cross sections and reaction rates for comparative planetary aeronomy. *Space Sci. Rev.*, 139:63, 2008.

[10] A. Luque, U. Ebert, and W. Hundsdorfer. Interaction of streamer discharges in air and other oxygen-nitrogen mixtures. *Phys. Rev. Lett.*, 101:075005, 2008.

[11] D. W. George. Magnetohydrodynamic electrical power generation. *Atom. Energy. Aust.*, 8:7, 1965.

[12] A. J. DeMaria. Review of CW high-power CO_2 lasers. *Proc. IEEE*, 61:731, 1973.

[13] A. Dalgarno and R. A. McCray. The formation of interstellar molecules from negative ions. *Astrophy. J.*, 181:95, 1973.

[14] N. F. Lane. The theory of electron-molecule collisions. *Rev. Mod. Phys.*, 52:29, 1980.

[15] R. Ajith Krishnan and B. S. Jinshah. Magnetohydrodynamic power generation. *Int. J. Sci. R. P.*, 3:1, 2013.

[16] P. V. Johnson, C. P. Malone, M. A. Khakoo, J. W. McConkey, and I. Kanik. Electron collisions with constituents of planetary atmospheres. *J. Phys. Conf. Ser.*, 88:012069, 2007.

[17] L. Campbell and M. J. Brunger. Modelling of plasma processes in cometary and planetary atmospheres. *Plasma Sources Sci. Technol.*, 22:013002, 2012.

[18] J. N. Moss and C. D. Scott. Thermophysical aspects of re-entry flows. 1986.

[19] M. A. Lieberman and A. J. Lichtenberg. *Principles of plasma discharges and materials processing*. John Wiley & Sons, 2005.

[20] W. N. G. Hitchon. *Plasma processes for semiconductor fabrication*, volume 8. Cambridge University Press, 2005.

[21] L. G. Christophorou and J. K. Olthoff. Electron interactions with plasma processing gases: an update for CF_4, CHF_3, C_2F_6, and C_3F_8. *J. Phys. Chem. Ref. Data*, 28:967, 1999.

[22] J. S. Yoon, M. Y. Song, H. Kato, M. Hoshino, H. Tanaka, M. J. Brunger, S. J. Buckman, and H. Cho. Elastic cross sections for electron collisions with molecules relevant to plasma processing. *J. Phys. Chem. Ref. Data*, 39:033106, 2010.

[23] L. Sanche. Low energy electron-driven damage in biomolecules. *Eur. Phys. J. D*, 35:367, 2005.

[24] W. F. van Dorp. The role of electron scattering in electron-induced surface chemistry. *Phys. Chem. Chem. Phys.*, 14:16753, 2012.

[25] W. F. Van Dorp, X. Zhang, B. L. Feringa, T. W. Hansen, J. B. Wagner, and J. Th. M. De Hosson. Molecule-by-molecule writing using a focused electron beam. *ACS nano*, 6:10076, 2012.

[26] A. J. Ragauskas, C. K. Williams, B. H. Davison, G. Britovsek, J. Cairney, C. A. Eckert, W. J. Frederick, J. P. Hallett, D. J. Leak, C. L. Liotta, et al. The path forward for biofuels and biomaterials. *Science*, 311:484, 2006.

[27] J. Amorim, C. Oliveira, J. A. Souza-Corrêa, and M. A. Ridenti. Treatment of sugarcane bagasse lignin employing atmospheric pressure microplasma jet in argon. *Plasma Process Polym.*, 10:670, 2013.

[28] E. M. de Oliveira, R. F. da Costa, S. d'A. Sanchez, A. P. P. Natalense, M. H. F. Bettega, M. A. P. Lima, and M. T. do. N. Varella. Low-energy electron scattering by cellulose and hemicellulose components. *Phys. Chem. Chem. Phys.*, 15:1682, 2013.

[29] J. Ishikawa. Negative ion beam technology for materials science. *Rev. Sci. Instrum.*, 63:2368, 1992.

[30] J. Ishikawa. Negative-ion source for implantation and surface interaction of negative-ion beams. *Rev. Sci. Instrum.*, 65:1290, 1994.

[31] J. Ishikawa. A heavy negative ion sputter source: Production mechanism of negative ions and their applications. *Nucl. Instr. Meth. Phys. Res. Sect. B: Beam Interactions with Materials and Atoms*, 37:38, 1989.

[32] M. R. C. McDowell. On the formation of H_2 in H I regions. *The Observatory*, 81:240, 1961.

[33] J. Simons. Theoretical studies of negative molecular ions. *Annu. Rev. Phys. Chem.*, 28:15, 1977.

[34] M. Agúndez, J. Cernicharo, M. Guélin, C. Kahane, E. Roueff, J. Klos, F. J. Aoiz, F. Lique, N. Marcelino, J. R. Goicoechea, M. González García, C.A. Gottlieb, M.C. McCarthy, and P. Thaddeus. Astronomical identification of CN^-, the smallest observed molecular anion. *Astronom. and Astrophys.*, 517:L2, 2010.

[35] P. Thaddeus, C. A. Gottlieb, H. Gupta, S. Brunken, M. C. McCarthy, M. Agundez, M. Guelin, and J. Cernicharo. Laboratory and astronomical detection of the negative molecular ion C_3N^-. *Astrophys. J.*, 677:1132, 2008.

[36] J. Cernicharo, M. Guelin, M. Agundez, K. Kawaguchi, and P. Thaddeus. Astronomical detection of C_4H^-, the second interstellar anion. *Astronom. and Astrophys.*, 467:L37, 2007.

[37] J. Cernicharo, M. Guélin, M. Agúndez, M. C. McCarthy, and P. Thaddeus. Detection of C_5N and vibrationally excited C_6H in IRC +10216. *Astrophys. J. Lett.*, 688:L83, 2008.

[38] H. Gupta, S. Brünken, F. Tamassia, C.A. Gottlieb, M.C. McCarthy, and P. Thaddeus. Rotational spectra of the carbon chain negative ions C_4H^- and C_8H^-. *Astrophys. J. Lett.*, 655:L57, 2007.

[39] M. C. McCarthy, C. A. Gottlieb, H. Gupta, and P. Thaddeus. Laboratory and astronomical identification of the negative molecular ion C_6H^-. *Astrophys. J. Lett.*, 652:L141, 2006.

[40] E. Herbst and Y. Osamura. Calculations on the formation rates and mechanisms for C_nH anions in interstellar and circumstellar media. *Astrophys. J.*, 679:1670, 2008.

[41] N. Harada and E. Herbst. Modeling carbon chain anions in L1527. *Astrophys. J.*, 685:272, 2008.

[42] K. Kentarou, R. Fujimori, S. Aimi, S. Takano, E.Y. Okabayashi, H. Gupta, S. Brünken, C.A. Gottlieb, M.C. McCarthy, and P. Thaddeus. Observation of C_8H^- toward IRC $+10216$. *Publ. Astron. Soc. JPN*, 59:L47, 2007.

[43] E. Herbst. Can negative molecular ions be detected in dense interstellar clouds? *Nature*, 289:656, 1981.

[44] T. E. Cravens, I. P. Robertson, J. H. Waite, R. V. Yelle, W. T. Kasprzak, C. N. Keller, S. A. Ledvina, H. B. Niemann, J. G. Luhmann, R. L. McNutt, et al. Composition of Titan's ionosphere. *Geophys. Res. Lett.*, 33, 2006.

[45] A. J. Coates, F. J. Crary, G. R. Lewis, D. T. Young, J. H. Waite, and E. C. Sittler. Discovery of heavy negative ions in Titan's ionosphere. *Geophys. Res. Lett.*, 34, 2007.

[46] T. E. Cravens, R. V. Yelle, J. E. Wahlund, D. E. Shemansky, and A. F. Nagy. *Composition and structure of the ionosphere and thermosphere*. Springer, 2009.

[47] J. H. Westlake, J. H. Waite, K. E. Mandt, N. Carrasco, J. M. Bell, B. A. Magee, and J. E. Wahlund. Titan's ionospheric composition and structure: Photochemical modeling of cassini INMS data. *J. Geophys. Res.*, 117, 2012.

[48] A. Faure, V. Vuitton, R. Thissen, L. Wiesenfeld, and O. Dutuit. Fast ion–molecule reactions in planetary atmospheres: a semiempirical capture approach. *Farad. Discuss.*, 147:337, 2010.

[49] E. Herbst. An approach to the estimation of polyatomic vibrational radiative relaxation rates. *Chem. Phys.*, 65:185, 1982.

[50] E. Herbst. Radiative association rate coefficients under shocked conditions in interstellar clouds - the case of $CH_3^+ + H_2$. *A&A*, 153:151, 1985.

[51] E. Clementi and A. D. McLean. Atomic negative ions. *Phys. Re.*, 133:A419, 1964.

[52] M. Gasda, N. D. Gibson, and C. W. Walter. *Photodetachment from negative ions*, volume 1. 1999.

[53] C. W. McCurdy and T. N. Rescigno. Collisions of electrons with polyatomic molecules: Electron-methane scattering by the complex kohn variational method. *Phys. Rev. A*, 39:4487, 1989.

[54] B. I. Schneider and T. N. Rescigno. Complex kohn variational method: Application to low-energy electron-molecule collisions. *Phys. Rev. A*, 37:3749, 1988.

[55] D. K. Watson, R. R. Lucchese, V. McKoy, and T. N. Rescigno. Schwinger variational principle for electron-molecule scattering: Application to electron-hydrogen scattering. *Phys. Rev. A*, 21:738, 1980.

[56] L. C. Leal. Brief review of the R-matrix theory, 2010.

[57] E. P. Wigner and L. Eisenbud. Higher angular momenta and long range interaction in resonance reactions. *Phys. Rev.*, 72:29, 1947.

[58] J. D. Gorfinkiel and J. Tennyson. Electron impact ionization of small molecules at intermediate energies: the molecular R-matrix with pseudostates method. *J. Phys. B-At Mol. Opt.*, 38:1607, 2005.

[59] J. Tennyson. Electron-molecule collision calculations using the R-matrix method. *Phys. Rep.*, 491:29, 2010.

[60] P. Descouvemont and D. Baye. The R-matrix theory. *Rep. Prog. Phys.*, 73:036301, 2010.

[61] J. Tennyson, J. Gorfinkiel, I. Rozum, C. Trevisan, and N. Vinci. Electron molecule collisions calculations using the R-matrix method. *Radiat. Phys. Chem.*, 68:65, 2003.

[62] C. Bloch. Une formulation unifiée de la théorie des réactions nucléaires. *Nucl. Phys.*, 4:503, 1957.

[63] A. M. Arthurs and A. Dalgarno. The theory of scattering by a rigid rotator. *P. Roy. Soc. Lond. A Mat.*, 256:540, 1960.

[64] F. A. Gianturco and W. M. Huo. *Computational methods for electron molecule collisions*. Springer Science & Business Media, 2013.

[65] T. N. Rescigno, C. W. McCurdy, A. E. Orel, and B. H. Lengsfield. *The complex Kohn variational method*. Springer, 1995.

[66] N. Douguet, S. Fonseca dos Santos, M. Raoult, O. Dulieu, A. E. Orel, and V. Kokoouline. Theoretical study of radiative electron attachment to CN, C_2H, and C_4H radicals. *J. Chem. Phys.*, 142:234309, 2015.

[67] J. Schwinger. A variational principle for scattering problems. *Phys. Rev.*, 72:742, 1947.

[68] B. A. Lippmann and J. Schwinger. Variational principles for scattering processes. I. *Phys. Rev.*, 79:469, 1950.

[69] J. M. Blatt and J. D. Jackson. On the interpretation of neutron-proton scattering data by the schwinger variational method. *Phys. Rev.*, 76:18, 1949.

[70] D. K. Watson. Schwinger variational methods. *Adv. Atom. Mol. Phys.*, 25:221, 1989.

[71] R. K. Nesbet. *Variational principles and methods in theoretical physics and chemistry*. Cambridge University Press, 2003.

[72] J. L. S. Lino and M. A. P. Lima. Studies of electron-molecule collisions using the schwinger variational principle with plane waves as a trial basis set. *Braz. J. Phys.*, 30:432, 2000.

[73] K. Takatsuka and V. McKoy. Theory of electronically inelastic scattering of electrons by molecules. *Phys. Rev. A*, 30:1734, 1984.

[74] M. A. P. Lima, L. M. Brescansin, A. J. R. da Silva, C. Winstead, and V. McKoy. Applications of the schwinger multichannel method to electron-molecule collisions. *Phys. Rev. A*, 41:327, 1990.

[75] R. R. Lucchese, D. K. Watson, and V. McKoy. Iterative approach to the Schwinger variational principle for electron-molecule collisions. *Phys. Rev. A*, 22:421, 1980.

[76] C. Schwartz. Application of the Schwinger variational principle for scattering. *Phys. Rev.*, 141:1468, 1966.

[77] E. Herbst. Negative ions in space: What they are telling us. *ASP Conf. Ser.*, 417:153, 2009.

[78] R. Terzieva and E. Herbst. Radiative electron attachment to small linear carbon clusters and its significance for the chemistry of diffuse interstellar clouds. *Int. J. Mass Spectrom.*, 201:135, 2000.

[79] S. Petrie and E. Herbst. Some interstellar reactions involving electrons and neutral species: Attachment and isomerization. *Astrophys. J.*, 491:210, 1997.

[80] S. Petrie. Novel pathways to CN^- within interstellar clouds and circumstellar envelopes: implications for IS and CS chemistry. *Mon. Not. R. Astron. Soc.*, 281:137, 1996.

[81] T. J. Millar, C. Walsh, M. A. Cordiner, R. Ní Chuimín, and E. Herbst. Hydrocarbon anions in interstellar clouds and circumstellar envelopes. *Astrophys. J. Lett.*, 662:L87, 2007.

[82] N. Douguet, V. Kokoouline, and A. E. Orel. Photodetachment cross sections of the $C_{2n}H$ ($n = 1 - 3$) hydrocarbon chain anions. *Phys. Rev. A*, 90:063410, 2014.

[83] T. N. Rescigno, B. H. Lengsfield III, and C. W. McCurdy. *Modern Electronic Structure Theory 1*, chapter 9, page 501. World Scientific, Singapore, 1995.

[84] T. N. Rescigno, C. W. McCurdy, A. E. Orel, and B. H. Lengsfield III. *Computational methods for electron molecule collisions*, chapter 1, page 1. Plenum Press, New York, 1995.

[85] C. S. Trevisan, A. E. Orel, and T. N. Rescigno. Ab initio study of low-energy electron collisions with ethylene. *Phys. Rev. A*, 68:062707, 2003.

[86] J. M. Carr, P. G. Galiatsatos, J. D. Gorfinkiel, A. G. Harvey, M. A. Lysaght, D. Madden, Z. Mašín, M. Plummer, J. Tennyson, and H. N. Varambhia. UKRmol: a low-energy electron- and positron-molecule scattering suite. *Euro. Phys. J. D*, 66:1, 2012.

[87] A. G. Harvey, D. S. Brambila, F. Morales, and O. Smirnova. An R-matrix approach to electron photon molecule collisions: photoelectron angular distributions from aligned molecules. *J. Phys. B: At. Mol. Opt. Phys.*, 47:215005, 2014.

[88] J. Tennyson, D. B. Brown, J. J. Munro, I. Rozum, H. N. Varambhia, and N. Vinci. Quantemol-N: an expert system for performing electron molecule collision calculations using the R-matrix method. *J. Phys. Conf. Series*, 86:012001, 2007.

[89] J. B. Halpern, Y. Huang, and T. Titarchuk. Radiative and collisional processes in $CN A\ ^2\Pi_i$. *Astrophys. Space SCI*, 236:11, 1996.

[90] P. Thaddeus. The short-wavelength spectrum of the microwave background. *Annu. Rev. Astron. Astr.*, 10:305, 1972.

[91] C. A. Gottlieb, S. Brunken, M. C. McCarthy, and P. Thaddeus. The rotational spectrum of CN. *J. Chem. Phys*, 126:191101, 2007.

[92] S. Harrison and J. Tennyson. Electron collisions with the CN radical: Bound states and resonances. *J. Phys. B: At. Mol. Opt. Phys.*, 45:035204, 2012.

[93] S. E. Bradforth, E. H. Kim, D. W. Arnold, and D. M. Neumark. Photoelectron spectroscopy of CN^-, NCO^-, and NCS^-. *J. Chem. Phys.*, 98:800, 1993.

[94] C. V. V. Prasad and P. F. Bernath. Fourier transform jet-emission spectroscopy of the $A^2\Pi_i$-$X^2\Sigma^+$ transition of CN. *J. Molec. Spectrosc.*, 156:327, 1992.

[95] R. Thomson and F. W. Dalby. Experimental determination of the dipole moments of the $X(^2\Sigma^+)$ and $B(^2\Sigma^+)$ states of the CN molecule. *Can. J. Phys.*, 46:2815, 1968.

[96] T. J. Lee and C. E. Dateo. Accurate spectroscopic characterization of $^{12}C^{14}N^-$, $^{13}C^{14}N^-$, and $^{12}C^{15}N^-$. *Spectrochim. Acta A*, 55:739, 1999.

[97] D. E. Woon and E. Herbst. Quantum chemical predictions of the properties of known and postulated neutral interstellar molecules. *Astrophys. J. Suppl. Ser.*, 185:273, 2009.

[98] H. J. Werner, P. J. Knowles, R. Lindh, F. R. Manby, M. Schütz, et al. MOLPRO, version 2008.3, A package of ab initio programs, 2008.

[99] E. L. Cochran, F. J. Adrian, and V. A. Bowers. ESR study of ethynyl and vinyl free radicals. *J. Chem. Phys.*, 40:213, 1964.

[100] K. D. Tucker, M. L. Kutner, and P. Thaddeus. The ethynyl radical C_2H-A new interstellar molecule. *Astrophys. J.*, 193:L115, 1974.

[101] T. R. Taylor, C. Xu, and D. M. Neumark. Photoelectron spectra of the $C_{2n}H^-(n = 1 - 4)$ and $C_{2n}D^-(n = 1 - 3)$ anions. *J. Chem. Phys.*, 108:10018, 1998.

[102] S. Joseph and A. Varandas. Ab initio based DMBE potential energy surface for the ground electronic state of the C_2H molecule. *J. Phys. Chem. A*, 114:2655, 2010.

[103] K. M. Ervin and W. C. Lineberger. Photoelectron spectra of C_2^- and C_2H^-. *J. Chem. Phys.*, 95:1167, 1991.

[104] NIST Computational Chemistry Comparison and Benchmark Database, NIST Standard Reference Database Number 101. Release 17b, Ed: Russell D. J., September 2015.

[105] J. C. Rienstra-Kiracofe, G. S. Tschumper, H. F. Schaefer, S. Nandi, and G. B. Ellison. Atomic and molecular electron affinities: photoelectron experiments and theoretical computations. *Chem. Rev.*, 102:231, 2002.

[106] P. G. Szalay, L. S. Thogersen, J. Olsen, M. Kallay, and J. Gauss. Equilibrium geometry of the ethynyl (CCH) radical. *J. Chem. Phys. A*, 108:3030, 2004.

[107] J. Natterer and W. Koch. Quantum chemical predictions of the electron affinities of carbon-hydrogen clusters $C_{2n}H\cdot$, the CH binding energies and the gas phase acidities of polyacetylenes C_{2n} H_2 for $n = 1 - 3$. *Mol. Phys.*, 84:691, 1995.

[108] S. Brünken, C. A. Gottlieb, H. Gupta, M. C. McCarthy, and P. Thaddeus. Laboratory detection of the negative molecular ion CCH^-. *A&A*, 464:L33, 2007.

[109] M. Guélin and P. Thaddeus. Tentative detection of the C_3N radical. *Astronom. J.*, 212:L81, 1977.

[110] P. Friberg, A. Hjalmarson, M. Guelin, and W. M. Irvine. Interstellar C_3N: Detection in Taurus dark clouds. *Astronom. J.*, 241:L99, 1980.

[111] C. A. Gottlieb, E. W. Gottlieb, P. Thaddeus, and H. Kawamura. Laboratory detection of the C_3N an C_4H free radicals. *Astronom. J.*, 275:916, 1983.

[112] T. A. Yen, E. Garand, A. T. Shreve, and D. M. Neumark. Anion photoelectron spectroscopy of C_3N^- and C_5N^-. *J. Phys. Chem. A*, 114:3215, 2009.

[113] B. Botschwina, P. Horn, M. Flugge, and S. Seeger. *J. Chem. Soc. Faraday Trans.*, 89:2219, 1993.

[114] R. Kołos, M. Gronowski, and P. Botschwina. Matrix isolation IR spectroscopic and ab initio studies of C(3)N(-) and related species. *J. Chem. Phys.*, 128:154305, 2008.

[115] M. Guélin, S. Green, and P. Thaddeus. Detection of the C_4H radical toward IRC plus 10216. *Astronom. J.*, 224:L27, 1978.

[116] J. Zhou, E. Garand, and D. M. Neumark. Slow electron velocity-map imaging spectroscopy of the $C_4H^-$and C_4D^-anions. *J. Chem. Phys.*, 127:154320, 2007.

[117] M. L. Senent and M. Hochlaf. Ab initio characterization of C_4^-, C_4H, and C_4H^-. *Astrophys. J.*, 708:1452, 2009.

[118] M. C. McCarthy and P. Thaddeus. Rotational spectrum and carbon-13 hyperfine structure of the C_3H, C_5H, C_6H, and C_7H radicals. *J. Chem. Phys.*, 122:174308, 2005.

[119] M. Kolbuszewski. The C_4H radical and the diffuse interstellar bands: an ab initio study. *Astrophys. J.*, 432:L63, 1994.

[120] S. Graf, J. Geiss, S. Leutwyler, et al. Ab initio calculations of excited states in C_4H and implications for ultraviolet photodissociation. *J. Chem. Phys.*, 114:4542, 2001.

[121] S. F. dos Santos, V. Kokoouline, and C. H. Greene. Dissociative recombination of H_3^+ in the ground and excited vibrational states. *J. Chem. Phys.*, 127:124309, 2007.

[122] M. Guélin, N. Neininger, and J. Cernicharo. Astronomical detection of the cyanobutadiynyl radical C_5N. *Astron. Astrophys.*, 335:L1, 1998.

[123] Y. Kasai, Y. Sumiyoshi, Y. Endo, and K. Kawaguchi. Laboratory detection of the C_5N radical by Fourier transform microwave spectroscopy. *Astrophys. J. Lett.*, 477:L65, 1997.

[124] P. Botschwina and R. Oswald. Carbon chains of type $C_{2n+1}N^-$ ($n = 2 - 6$): A theoretical study of potential interstellar anions. *J. Chem. Phys.*, 129:044305, 2008.

[125] P. Botschwina. The two lowest electronic states of C_5N: results of coupled cluster calculations. *Chem. Phys. Lett.*, 259:627, 1996.

[126] M. C. McCarthy, C. A. Gottlieb, H. Gupta, and P. Thaddeus. Laboratory and astronomical identification of the negative molecular ion C_6H^-. *Astrophys. J. Lett.*, 652:L141, 2006.

[127] T. Pino, M. Tulej, F. Guthe, M. Pachkov, and J. P. Maier. Photodetachment spectroscopy of the $C_{2n}H^-$ ($n = 2 - 4$) anions in the vicinity of their electron detachment threshold. *J. Chem. Phys.*, 116:6126, 2002.

[128] D. E. Woon. A correlated ab initio study of linear carbon-chain radicals C_nH ($n = 2 - 7$). *Chem. Phys. Lett.*, 244:45, 1995.

[129] S. Brünken, H. Gupta, C. A. Gottlieb, M. C. McCarthy, and P. Thaddeus. Detection of the carbon chain negative ion C_8H^- in TMC-1. *Astrophys. J. Lett.*, 664:L43, 2007.

[130] F. Pichierri. Molecular structure of the octatetranyl anion, C_8H^-: A computational study. *J. Phys. Chem. A*, 112:7717, 2008.

[131] J. D. Watts and R. J. Bartlett. Economical triple excitation equation-of-motion coupled-cluster methods for excitation energies. *Chem. Phys. Lett.*, 233:81, 1995.

[132] W. P. Kraemer and B. O. Roos. A CAS SCF CI study of the $^1\Sigma_g^+$ and $^3\Pi_u$ states of the C_2 molecule and the $^4\Sigma_g$ and $^2\Pi_u$ states of the C_2^+ ion. *Chem. Phys.*, 118:345, 1987.

[133] F. A. Gianturco and T. Stoecklin. Electron scattering from acetylene: elastic integral and differential cross sections at low energies. *J. Phys. B-At. Mol. Opt.*, 27:5903, 1994.

[134] A. C. Danks and M. Dennefeld. Near-infrared spectroscopy of comet Bradfield 1979l. *Astron. J.*, 86:314, 1981.

[135] G. Halmova, J. Gorfinkiel, and J. Tennyson. Low energy electron collisions with C_2 using the R-matrix method. *J. Phys. B-At Mol. Opt.*, 39:2849, 2006.

[136] P. Starke, U. Fantz, and M. Balden. Investigations of chemical erosion of carbon materials in hydrogen and deuterium low pressure plasmas. *J. Nucl. Mater.*, 337:1005, 2005.

[137] E. P. Hunter and S. G. Lias. Nist chemistry webbook. *NIST Standard Reference Database*, 69, 2005.

[138] P. L. Jones, R. D. Mead, B. E. Kohler, S. D. Rosner, and W. C. Lineberger. Photodetachment spectroscopy of C_2^- autodetaching resonances. *J. Chem. Phys.*, 73:4419, 1980.

[139] D. R. Dension and L. D. Hartsough. Laser induced dissociative chemical gas phase processing of workpieces, 1981. US Patent 4,260,649.

[140] J. J. Munro, S. Harrison, Fujimoto M. M., and Tennyson J. A dissociative electron attachment cross-section estimator. *J. Phys. Conf. Ser.*, 388:012013, 2012.

[141] S. T. Chourou and A. E. Orel. Dissociative electron attachment to HCN and HNC. *Phys. Rev. A*, 80:032709, 2009.

[142] L. G. Christophorou. *Electron Molecule Interactions and Their Applications*, volume 2. Academic Press, 2013.

[143] M. Braun, M. W. Ruf, I. I. Fabrikant, and H. Hotop. Observation of p-wave threshold behavior in electron attachment to F_2 molecules. *Phys. Rev. Lett.*, 99:253202, 2007.

[144] S. Barsotti, M. W. Ruf, and H. Hotop. Clear experimental evidence for p-wave attachment threshold behavior in electron attachment to chlorine molecules. *Phys. Rev. Lett.*, 89:083201, 2002.

[145] H. Hotop, M. W. Ruf, M. Allan, and I. I. Fabrikant. Resonance and threshold phenomena in low-energy electron collisions with molecules and clusters. *Adv. At. Mol. Opt. Phy.*, 49:85, 2003.

[146] N. S. Shuman, T. M. Miller, A. A. Viggiano, and I. I. Fabrikant. Thermal electron attachment to F_2. *Phys. Rev. A*, 88:062708, 2013.

[147] I. I. Fabrikant. Recent progress in the theory of dissociative attachment: From diatomics to biomolecules. *JPCS*, 204:012004, 2010.

[148] M. W. Ruf, S. Barsotti, M. Braun, H. Hotop, and I. I. Fabrikant. Dissociative attachment and vibrational excitation in low-energy electron collisions with chlorine molecules. *J. Phys. B-At. Mol. Opt.*, 37:41, 2003.

[149] J. F. Friedman, T. M. Miller, L. C. Schaffer, A. A. Viggiano, and I. I. Fabrikant. Electron attachment to Cl_2 from 300 to 1100 K: Experiment and theory. *Phys. Rev. A*, 79:032707, 2009.

[150] H. B. Wahlin. Behavior of free electrons toward gas molecules. *Phys. Rev.*, 19:173, 1922.

[151] N. E. Bradbury. Formation of negative ions in gases by electron attachment part I. NH_3, CO, NO, HCl and Cl_2. *Chem. Phys.*, 2:827, 1934.

[152] R. E. Center and A. Mandl. Ionization cross sections of F_2 and Cl_2 by electron impact. *J. Chem. Phys*, 57:4104, 1972.

[153] W. L. Morgan. A critical evaluation of low-energy electron impact cross sections for plasma processing modeling. I: Cl_2, F_2, and HCl. *Plasma Chem. Plasma Process.*, 12:449, 1992.

[154] J. P. Wiens, J. C. Sawyer, T. M. Miller, N. S. Shuman, A. A. Viggiano, M. Khamesian, V. Kokoouline, and I. I. Fabrikant. Electron attachment to the interhalogen compounds ClF, ICl, and IBr. *Phys. Rev. A*, 93:032706, 2016.

[155] M. T. Nguyen and T. K. Ha. Ab initio calculation of the ionization potentials and hyperfine splitting constants of the radical anions FCl^{xxx} and Cl_2^{xxx}. *Chem. Phys. Lett.*, 136:413, 1987.

[156] C. K. Law, S. H. Chien, W. K. Li, and Y. S. Cheung. Thermochemistry of chlorine fluorides ClF_n, $n = 1 - 7$, and their singly charged cations and anions: A Gaussian-3 and Gaussian-3X study. *Phys. Chem. A*, 106:11271, 2002.

[157] A. B. Alekseyev, H. P. Liebermann, R. J. Buenker, and D. B. Kokh. Relativistic configuration interaction study of the ClF molecule and its emission spectra from 0^+ ion-pair states. *Chem. Phys.*, 112:2274, 2000.

[158] S. Li, S. J. Chen, D. S. Zhu, and J. J. Wei. Structure and potential energy function of ClF-molecular ion. *Acta. Phys-Chim. Sin.*, 29:737, 2013.

[159] T. J. V. Huis, J. M. Galbraith, and H. F. Schaefer. The monochlorine fluorides (ClF_n) and their anions (ClF_n^-) $n = 1 - 7$: structures and energetics. *Mol. Phys.*, 89:607, 1996.

[160] I. S. McDermid. Potential-energy curves, Franck-Condon factors and laser excitation spectrum for the $B^3\Pi(0^+)$–$X^1\Sigma^+$ system of chlorine monofluoride. *J. Chem. Soc. Farad. T. 2: Mol. and Chem. Phys.*, 77:519, 1981.

[161] A. U. Hazi. Behavior of the eigenphase sum near a resonance. *Phys. Rev. A*, 19:920, 1979.

[162] W. Domcke. Theory of resonance and threshold effects in electron-molecule collisions: The projection-operator approach. *Phys. Rep.*, 208:97, 1991.

[163] D. J. Haxton, C. W. McCurdy, and T. N. Rescigno. Angular dependence of dissociative electron attachment to polyatomic molecules: Application to the $^2B_1$ metastable state of the H_2O and H_2S anions. *Phys. Rev. A*, 73:062724, 2006.

[164] T. F. O'malley. Theory of dissociative attachment. *Phys. Rev.*, 150:14, 1966.

[165] D. T. Birtwistle and A. Herzenberg. Vibrational excitation of N_2 by resonance scattering of electrons. *J. Phys. B-At. Mol. Phys.*, 4:53, 1971.

[166] R. J. Hall. Dissociative attachment and vibrational excitation of F_2 by slow electrons. *Chem. Phys.*, 68:1803, 1978.

[167] J. N. Bardsley and J. M. Wadehra. Dissociative attachment in HCl, DCl, and F_2. *Chem. Phys.*, 78:7227, 1983.

[168] I. I. Fabrikant, T. Leininger, and F. X. Gadéa. Low-energy dissociative electron attachment to Cl_2 molecules. *J. Phys. B-At. Mol. Opt.*, 33:4575, 2000.

[169] T. Rescigno, V. McKoy, and B. Schneider. *Electron-molecule and Photon-molecule Collisions*, volume 5. Springer, 1979.

[170] I. I. Fabrikant and H. Hotop. Low-energy behavior of exothermic dissociative electron attachment. *Phys. Rev. A*, 63:022706, 2001.

[171] W. M. Haynes. *CRC handbook of chemistry and physics*. CRC press, 2014.

[172] I. I. Fabrikant and H. Hotop. On the validity of the Arrhenius equation for electron attachment rate coefficients. *J. Chem. Phys*, 128:124308, 2008.

[173] A. Gauf, C. Navarro, G. Balch, L. R. Hargreaves, M. A. Khakoo, C. Winstead, and V. McKoy. Low-energy elastic electron scattering by acetylene. *Phys. Rev. A*, 87:012710, 2013.

[174] J. H. Lacy, N. J. Evans, J. M. Achtermann, D. E. Bruce, J. F. Arens, and J. S. Carr. Discovery of interstellar acetylene. *Astrophys. J.*, 342:L43, 1989.

[175] S. T. Ridgway. Jupiter: Identification of ethane and acetylene. *Astrophys. J.*, 187:L41, 1974.

[176] R. Hanel, B. Conrath, F. M. Flasar, V. Kunde, W. Maguire, J. Pearl, J. Pirraglia, R. Samuelson, L. Herath, M. Allison, et al. Infrared observations of the saturnian system from voyager 1. *Science*, 212:192, 1981.

[177] B. Bézard, P. N. Romani, B. J. Conrath, and W. C. Maguire. Hydrocarbons in neptune's stratosphere from voyager infrared observations. *J. Geophys. Res-Space Phys.*, 96:18961, 1991.

[178] J. I. Lunine. The atmospheres of uranus and neptune. *Annu. Rev. Astron. Astrophys.*, 31:217, 1993.

[179] J. Benedikt. Plasma-chemical reactions: low pressure acetylene plasmas. *J. Phys. D: Appl. Phys.*, 43:043001, 2010.

[180] L. Andric and R. I. Hall. Resonance phenomena observed in electron scattering from acetylene. *J. Phys. B-At. Mol. Opt.*, 21:355, 1988.

[181] L. Monchick, R. J. Munn, and E. A. Mason. Thermal diffusion in polyatomic gases: A generalized stefan-maxwell diffusion equation. *J. Chem. Phys*, 45:3051, 1966.

[182] D. L. Akins, E. H. Fink, and C. B. Moore. Rotation−translation energy transfer between individual quantum states of HD ($B^1\Sigma_u^+$). *J. Chem. Phys*, 52:1604, 1970.

[183] J. W. Riehl, C. J. Fisher, J. D. Baloga, and J. L. Kinsey. Spin-lattice relaxation and the anisotropic part of the H_2-He and H_2-Ne intermolecular potential. *J. Chem. Phys*, 58(10):4571, 1973.

[184] T. L. Cottrell and J. C. McCoubrey. *Molecular energy transfer in gases*. Butterworths, 1961.

[185] A. C. Allison and A. Dalgarno. The rotational excitation of molecular hydrogen. *Proc. Phys. Soc.*, 90:609, 1967.

[186] D. R. Miller and R. P. Andres. Rotational relaxation of molecular nitrogen. *J. Chem. Phys*, 46:3418, 1967.

[187] D. A. Varshalovich, A. N. Moskalev, and V. K. Khersonskii. *Quantum theory of angular momentum*. World Scientific, 1988.

[188] K. Kuchitsu. *Structure of free polyatomic molecules: basic data*. Springer Science & Business Media, 2013.

[189] D. Thirumalai, K. Onda, and D. G. Truhlar. Elastic scattering and rotational excitation of a polyatomic molecule by electron impact: Acetylene. *J. Chem. Phys.*, 74:526, 1981.

[190] A. Jain. Low energy (0.01-20 eV) electron scattering from acetylene. *J. Phys. B-At. Mol. Opt.*, 26:4833, 1993.

[191] Y. Nakamura. Electron swarm parameters in pure C_2H_2 and in C_2H_2-Ar mixtures and electron collision cross sections for the C_2H_2 molecule. *J. Phys. D Appl. Phys.*, 43:365201, 2010.

[192] Quantemol – A software tool maintained by quantemol Ltd, which is based in university college london. The code brings a full accessibility to the UK molecular R-matrix code, which is used to model electron polyatomic molecule interactions.

[193] M. Satta, F. A. Gianturco, F. Carelli, and R. Wester. A quantum study of the chemical formation of cyano anions in inner cores and diffuse regions of interstellar molecular clouds. *Astrophys. J.*, 799:228, 2015.

[194] F. Carelli, M. Satta, T. Grassi, and F. A. Gianturco. Carbon-rich molecular chains in proto-planetary and planetary atmospheres: quantum mechanisms and electron attachment rates for anion formation. *Astrophys. J.*, 774:97, 2013.

[195] F. Carelli, F. A. Gianturco, R. Wester, and M. Satta. Formation of cyanopolyyne anions in the interstellar medium: The possible role of permanent dipoles. *J. Chem. Phys.*, 141:054302, 2014.

[196] R. N. Compton, H. S. Carman Jr, C. Desfrancois, H. Abdoul-Carime, J. P. Schermann, J. H. Hendricks, S. A. Lyapustina, and K. H. Bowen. On the binding of electrons to nitromethane: Dipole and valence bound anions. *J. Chem. Phys*, 105:3472, 1996.

[197] F. Güthe, M. Tulej, M. V. Pachkov, and J. P. Maier. Photodetachment spectrum of I-$C_3H_2^-$: The role of dipole bound states for electron attachment in interstellar clouds. *Astrophys. J.*, 555:466, 2001.

[198] C. E. H. Dessent, J. Kim, and M. A. Johnson. Spectroscopic observation of vibrational Feshbach resonances in near-threshold photoexcitation of $X^-{\cdot}CH_3NO_2$ (X^- = I^- and Br^-). *Farad. Discuss.*, 115:395, 2000.

[199] M. Stepanović, Y. Pariat, and M. Allan. Dissociative electron attachment in cyclopentanone, γ-butyrolactone, ethylene carbonate, and ethylene carbonate-d_4: Role of dipole-bound resonances. *J. Chem. Phys*, 110:11376, 1999.